GRADUAL FAILURE OF HIGH-PERFORMANCE HYBRID COMPOSITES: TENSILE AND BENDING BEHAVIOUR

By

B. Eng, M.Eng
GUILLERMO ANDRÉS IDÁRRAGA ALARCÓN

NATIONAL UNIVERSITY OF COLOMBIA
FACULTY OF MINES

SCHOOL OF MINERALS AND MATERIALS

MEDELLÍN

2020

FALLA GRADUAL DE MATERIALES COMPUESTOS HÍBRIDOS DE ALTO DESEMPEÑO: COMPORTAMIENTO BAJO TENSIÓN Y FLEXIÓN

Por

B. Eng, M.Eng
GUILLERMO ANDRÉS IDÁRRAGA ALARCÓN

UNIVERSIDAD NACIONAL DE COLOMBIA
FACULTAD DE MINAS

ESCUELA DE MATERIALES Y MINERALES

MEDELLÍN

2020

HIGH-PERFORMANCE PSEUDO-DUCTILE HYBRID COMPOSITES: TENSILE AND BENDING BEHAVIOUR

A dissertation submitted to the National University of Colombia in accordance with the requirements of the degree of PhD in Engineering - Materials Science and Technology.

M.Eng. Guillermo Andrés Idárraga Alarcón
Design of Advanced Composite Structures DADCOMP
The National University of Colombia.
gaidarra@unal.edu.co

SUPERVISOR:
Dr. Juan Manuel Meza Meza
National University of Colombia
jmmezam@unal.edu.co

SUPERVISOR:
Dr. Meisam Jalalvand
University of Southampton
M.Jalalvand@soton.ac.uk

I dedicate this dissertation to
my mother Consuelo, my sister Katherine
and my wife Magaly

"Live as if you were to die tomorrow.
Learn as if you were to live forever"

Mahatma Gandhi

ABSTRACT

Fibre-reinforced composites are increasingly used for primary structures, as they provide significant weight savings while maintaining the highest material and structural performance, improving fuel efficiency and lowering maintenance costs. Unfortunately, the high stiffness and strength of composite materials come at the expense of their limited toughness. The failure of composites is usually sudden and catastrophic. To ensure safe operations, much greater safety factors are applied for composites than for ductile materials like metals. This condition produces overdesigned structures, reducing the weight benefits. These serious limitations not only prevent engineers and operators from exploiting the performance advantages of composites, but render them unsuitable for many applications in which loading conditions are not fully predictable, and catastrophic failure cannot be tolerated. Achieving gradual failure in composites can help structures to maintain functionality even when they are overloaded, increasing the scope of composites applications in critical structures in industries such as aerospace and automotive.

The aim of this thesis is to explore the gradual failure of thin ply hybrid composites under tension and bending, combining experimental and numerical analysis. This work introduces new composite architectures using thin ply carbon-epoxy prepregs and standard ply thickness S-Glass-epoxy prepregs in an interplay configuration. All laminates are consolidated using autoclave and tested in a computer-controlled universal servo-hydraulic test machine. For tensile tests, less explored multidirectional layups are proposed, analysing the hybrid effect when stacking sequence is modified. The hybrid effect is defined in this thesis as the enhancement in the strain at failure of the carbon fibres in a hybrid composite compared with a pure carbon composite. On the other hand, for bending tests, a new methodology and two novel unidirectional asymmetric layups are proposed to achieve gradual failure by promoting failure initiation in tension and avoid catastrophic failure in compression.

Favourable gradual failure has been achieved for hybrid configurations in both tension and bending. The failure is characterised by progressive degradation of the thin carbon/epoxy layers by multiples cracks (fragmentation) and dispersion delamination. For tensile tests, standard thickness S-glass/epoxy layers fail suddenly after further strength reduction of carbon plies by fragmentation. Variation in the hybrid effect was investigated in the earliest stage of damage, analysing a single crack in one of the 0° carbon plies. The non-uniform strain distribution through the thickness produced by the crack is affected by the stacking sequence, increasing or decreasing the strain concentration on the undamaged layers and changing the hybrid effect. Correlations between the hybrid effect and stiffness of the adjacent layer were proposed.

On the other hand for bending tests, catastrophic failure is avoided and high values of flexural displacement were achieved. The gradual layer-by-layer failure of the surface layers on the tensile side produces a brush-like appearance. Microscopy observations from interrupted tests verified fragmentation followed by local delamination on the tensile side of the beam. Stable shear cracks at an angle between ±45° and ±60° to the fibre direction were also identified as a unique failure mechanism in compression. Numerical analysis was crucial to understanding the failure sequence and damage mechanism in the hybrid configurations.

RESUMEN

Los compuestos reforzados con fibra se utilizan cada vez más para estructuras primarias, ya que proporcionan un ahorro de peso significativo al tiempo que mantienen el mayor desempeño estructural, mejorando la eficiencia en combustible y reduciendo los costos de mantenimiento. Desafortunadamente, la alta rigidez y resistencia de los materiales compuestos se obtiene a expensas de su limitada tenacidad. El fallo de los compuestos suele ser repentino y catastrófico. Para garantizar operaciones seguras, se aplican factores de seguridad mucho mayores para los compuestos que para los materiales dúctiles como los metales. Esta condición produce estructuras sobrediseñadas, reduciendo los beneficios de peso. Estas graves limitaciones no solo impiden que los ingenieros y operadores aprovechen las ventajas de rendimiento de los compuestos, sino que los hacen inadecuados para muchas aplicaciones en las que las condiciones de carga no son completamente predecibles y no se pueden tolerar fallas catastróficas. Lograr una falla gradual en los materiales compuestos puede ayudar a las estructuras a mantener la funcionalidad incluso cuando están sobrecargadas, aumentando el alcance de las aplicaciones de los compuestos en estructuras críticas en industrias como la aeroespacial y la automotriz.

El objetivo de esta tesis es explorar el fallo gradual de los compuestos híbridos bajo tensión y flexión, combinando análisis experimental y numérico. Este trabajo presenta nuevas arquitecturas compuestas que utilizan preimpregnados de carbono-epoxi de capas delgadas y preimpregnados de vidrio-epoxi tipo S de espesor de capa estándar. Todos los laminados se consolidan en autoclave y se prueban en una máquina de prueba servo-hidráulica universal controlada por computadora. Para los ensayos de tracción, se proponen laminados multidireccionales, analizando el efecto híbrido cuando se modifica la secuencia de apilamiento. El efecto híbrido se define en esta tesis como la mejora en la deformación en caso de rotura de las fibras de carbono en un compuesto híbrido en comparación con un compuesto de carbono puro. Por otro lado, para los ensayos de flexión, se propone una nueva metodología y dos novedosos laminados asimétricos unidireccionales para lograr un fallo gradual al promover el inicio del fallo en tracción y evitar un fallo catastrófico en compresión.

Con este trabajo se logra una falla gradual para configuraciones híbridas tanto en tensión como en flexión. La falla se caracteriza por la degradación progresiva de las capas delgadas de carbono por múltiples grietas (fragmentación) y delaminación local. Para las pruebas de tracción, las capas de vidrio de espesor estándar fallan repentinamente después de una mayor reducción de la resistencia de las capas de carbono por fragmentación. Se investigó la variación en el efecto híbrido en la etapa más temprana del daño, analizando una sola grieta en una de las capas de carbono 0 °. La distribución de deformaciones no uniforme a través del espesor producido por la fisura se ve afectada por la secuencia de apilamiento, aumentando o disminuyendo la concentración de deformaciones en las capas no dañadas y cambiando el efecto híbrido. Se propusieron correlaciones entre el efecto híbrido y la rigidez de la capa adyacente.

Por otro lado, para los ensayos de flexión se evitan fallas catastróficas y se logran altos valores de desplazamiento por flexión. El fallo gradual capa por capa de las capas superficiales en el lado de tracción produce una apariencia similar a un cepillo. Las observaciones microscópicas de las pruebas interrumpidas verificaron la fragmentación seguida de delaminación local en el lado de tracción de la viga. Grietas a un ángulo entre ±

45 ° y ± 60 ° con respecto a la dirección de la fibra se identificaron como mecanismo de falla único en compresión. El análisis numérico fue crucial para comprender la secuencia de fallas y el mecanismo de daño en las configuraciones híbridas.

KEY WORDS

Bending; Tension; Hybrid composites; Gradual failure; Fragmentation;

PALABRAS CLAVES

Flexión; Tensión; Compuestos híbridos; Falla gradual; Fragmentación;

ACKNOWLEDGEMENTS

This research was support by the Ministry of Science and Education of Colombia - Doctoral grant, Minciencias - Call 647. Sapiencia of the municipality of Medellín, the funding call Enlaza-Mundos programme 2017. The Newton Fund: Industry-Academia Partnership Programme. The University of Bristol, the University of Strathclyde and the National University of Colombia.

Doing a PhD is an excruciating task that cannot be done without the help and support of many special people. I would, therefore, like to start by thanking Prof. Juan Manuel Meza Meza for allowing me to do this project at an esteemed institution such as the National University of Colombia. I appreciate all the support that you gave me during these years and especially for trust in my work. I owe deep gratitude to Dr. Meisam Jalalvand, this would not have been possible without your support, advising and guidance. I learned a lot from you not only in the academic aspect but also concerning life, you are a great person Meisam.

I would particularly acknowledge Juan Manuel Macias who took the challenge of continue this work and improve the model of bending. I also would like to express my appreciation to my colleagues of the DADCOMP research group, Jose David Acosta and Johnattan Vargas and all the members of the M17 building. I owe my gratitude to Mery Arrubla for your help in the laboratory tasks and your friendship during all these years.

To the people closest to my heart, my mother Consuelo and my sister Katherine: thank you to be always there supporting me. To my wife, I think there are not enough words in this thesis to thank you, thanks for pushing me to finish writing this thesis, for your love, for your support, for your patience during my internships and especially for being my wife.

CONTRIBUTIONS AND PUBLICATIONS

PROJECTS

During my PhD I contributed writing and developing the next projects:

1. SFC GCRF Escalator Fund 2019/20; Biodegradable material for cross-Atlantic transport baskets of fresh products including avocados to the UK. **GBP 69.825.**
2. Industry-Academia Partnership Programme (IAPP) – Colombia 2019; New environmentally friendly natural fibre composite materials for low power wind turbine blades for rural areas. Total funding: **GBP 110.473.**
3. SFC GCRF Escalator Fund 2018/19; Fique natural fibre composites – A new degradable composite material for local automotive industries in Colombia; Total funding: **GBP 61.000.**
4. Industry-Academia Partnership Programme (IAPP) – Colombia 2018; Novel Hybrid Composites to improve structural performance of a Compact Electric Utility Vehicles Chassis; Total funding: **GBP 101.000**.
5. Industry-Academia Partnership Programme (IAPP) – Colombia 2017; Optimisation of Composite Structures for Compact Electric Utility Vehicles; Total funding: **GBP 96.000.**

MASTER THESES

From this work two master theses were proposed and already finished:

- Jose David Acosta Correa. Master's thesis “Numerical modelling and experimental evaluation of open-hole tensile multidirectional carbon/glass hybrid composites”. Program: Master of Engineering - Materials and Processes. National University of Colombia 4 – August – 2020.
- Juan Manuel Macias Lopez. Master's thesis “Numerical and analytical models for design of hybrid composite laminates with gradual failure behaviour under bending loads” Program: Master of Engineering - Materials and Processes. National University of Colombia 4 – September – 2020.

JOURNAL PAPERS

G.Idarraga, M. Jalalvand, M. Fotouhi, J. Meza, M.R. Wisnom. Gradual failure in high-performance unidirectional thin-ply carbon/glass hybrid composites under bending. Composites Part A JCOMA-20-1483 (Under Review)

G.Idarraga, M. Jalalvand, J. Meza, M.R. Wisnom. The hybrid effect and plies interaction on high-performance quasi-isotropic carbon/glass composites (being prepared).

D. Acosta, **G. Idarraga**, J Meza, M. Jalalvand, P. Maimí. Numerical modelling of tensile notch behaviour of quasi-isotropic thin-ply carbon/glass hybrid composites (being prepared).

CONFERENCE PAPERS

G. Idarraga, M. Fotouhi, M. Jalalvand, J. Meza, M.R. Wisnom. Experimental and numerical study of hybrid effect in high-performance quasi-isotropic thin-ply carbon/glass composites. Twenty-second international conference on composite materials (ICCM22), Melbourne Australia 2019.

M. Jalalvand, **G. Idarraga**, M. Fotouhi, J. Meza, M.R. Wisnom. Achieving gradual failure in hybrid composite laminates in bending. Twenty-second international conference on composite materials (ICCM22), Melbourne Australia 2019.

Content

List of Figures

List of Tables

CHAPTER 1 INTRODUCTION

Composites combine short or long fibres with a binding polymer matrix. The fibres act as the stiff and strong phase in the material while the matrix makes the fibres deform as one entity. Modern composites were established at the middle of the 20th century, when a new generation of plastics was developed, like vinylester, polystyrene, phenolic and polyester resins. Between the thirties and the seventies with the design and manufacture of new reinforcing fibres including glass, aramid and carbon, fibre reinforced plastics (FRPs) or composites laid its foundation as a matured industry [1]. Today, the market for composite products, across all sectors, has a value of around USD 74bn and it is projected to reach USD 112bn by 2025 [2]. Where glass-reinforced polymers (GRPs) dominate the material composite market with a global demand of over 95%, while carbon-reinforced polymers (CRPs) represent 1-2% of the market's share [3].

Composites are attractive due to their high strength and moderate stiffness combined with a low density and corrosion resistance. These benefits make composites more interesting for the industry, replacing the traditional materials in many different applications. The most prominent consumers of composites are the aerospace, automotive, construction and wind energy industries. Light-weight and higher-performance composite structures allow reducing weight in the automotive and aerospace vehicles savings in running costs and, more significantly, carbon emissions. One example is the Airbus A350 XWB which burns 25% less fuel in comparison with an equivalent aircraft because 53% of its weight is manufactured using composites [4]. On the other hand, to produce higher power wind turbines, the wind industry is increasingly looking to design and manufacture turbines with larger blades. However, the increase in size and weight of larger blades requires stiffer materials to prevent blades bending and hitting the turbine tower. The strength and stiffness of advanced composites make them an ideal material for the production of this new generation of wind turbines [5].

Although composite materials are now well established in multiple applications, their failure is usually sudden, without sufficient warning and little amount of residual load-carrying capacity. These limitations hinder the design and exploitation of composite structures. Therefore, promote and understand the gradual failure of composites with a wider margin between damage initiation and final failure is highly important. This will help manufacturers of high-performance composite products to reduce their overdesign and increase reliability in critical applications.

One of the successful approaches for introducing gradual failure into composite materials and avoiding catastrophic failure is hybridisation. By combining two types of fibres with different failure strains and selecting an appropriate configuration, it is possible to obtain gradual failure and a pseudo-ductile response. However, if the configuration and material combination is not selected appropriately, not only the tensile response is brittle, but also the mechanical properties of the hybrid are worse than those of the constituents. The approach to get gradual failure using hybrid composites is based on the suppression of catastrophic failure mechanisms and the promotion of multiples fractures in the low strain

material. This allows achieving a stable degradation and a smooth load transfer from the degraded low strain material to the high strain material, producing a nonlinear stress-strain response. This concept will be further explained in section 2.7.

These new type of composites materials with gradual failure have been developed in recent years. G. Czel and M.R. Wisnom demonstrated the pseudo-ductile response of the hybrid composites in 2013 [6] and after that, several studies have been conducted to understand failure mechanisms and optimise the design of these materials [7]-[10]. However, most of the studies and predictive tools have been developed based on unidirectional layups under tensile tests, being less explored other loading conditions. To promote wider use of hybrid composites with gradual failure and increase the reliability of these materials in high-performance applications, this thesis studies the gradual failure under multidirectional and bending conditions. Proposing a novel method to get gradual failure in bending and providing a new understanding of the hybrid effect in multidirectional layups.

CHAPTER 2 LITERATURE REVIEW

2.1 Composites Materials

A composite is formed by the combination of two or more physical or chemical different materials to produce a new material with enhanced properties. In composites, the combined materials are classified into two categories, reinforcements and matrix. The reinforcements are usually stiffer and stronger than the matrix, while the matrix typically has a higher elongation to failure compared to the reinforcement. Reinforcements can be continuous (long fibres), discontinuous (chopped fibres) and particles (powders), and their selection and use depend mainly on the application and the properties desired. Among the wide range of properties that could be improved are impact, erosion and wear resistance, acoustic and vibration damping, enhanced fatigue life, electromagnetic transparency, thermal and electric conductivity, self-healing, fire resistance, among others [11]. In a composite material, the reinforcement is distributed within the matrix which provides support and allow transferring the load between the constituents. In composites where more than one reinforcement in the matrix is used, the composite is said to be a hybrid.

In high-performance structural applications where materials with higher strength and stiffness are required, fibre reinforcements are preferred because its small diameter reduces the size and quantity of defects and because its aspect ratio allows an effective load transference. However, in the case of polymeric fibres, such as aramid fibres, the main contribution comes from an alignment of the polymer chains in the fibre direction. Additionally, fibres have higher values of strength/weight and stiffness/weight ratios than most materials, which makes them relevant in lightweight applications. Although fibres can withstand high tensile loads, they cannot sustain compression and shear loads, therefore, to achieve functional structures the matrix works as a binder to hold the fibres together.

Carbon and glass fibres are some of the most used fibre types in composite materials, both fibres have excellent stiffness and strength, combined with a low density [12],[13]. In the case of carbon, the most commercial fibres are polyacrylonitrile (PAN) and pitch-based. The production processes for both fibres starts from a different base material, which leads to a different microstructure and hence different mechanical, thermal and electrical properties. PAN-based carbon fibres can reach a maximum strength of 7.1 GPa while the maximum strength reported for Pitch-based carbon fibres is 4GPa [14],[15]. Both types of carbon fibres are made out of graphite planes that are oriented preferentially in the fibre direction and also folded, see Figure 1. This particular arrangement of graphite makes carbon fibres transversely isotropic, the longitudinal stiffness of standard carbon fibres ranges between 200 and 400 GPa, while their transverse stiffness ranges between 5 and 30 GPa, depending on the fibre type [16]. On the other hand, glass fibres are amorphous and unoriented. The most well-known types of glass fibres are E-glass and S-glass fibres, where E and S come from electrical and strength respectively. S-glass offers higher stiffness and strength and better corrosion resistance than E-glass but poor drawability and hence increased cost [12],[18]. The maximum strength may yield up to 3.5 GPa for E-glass and 4.8 GPa for S-

glass [11]. Unlike carbon fibre, glass fibres are isotropic and their tensile modulus is the same in all directions.

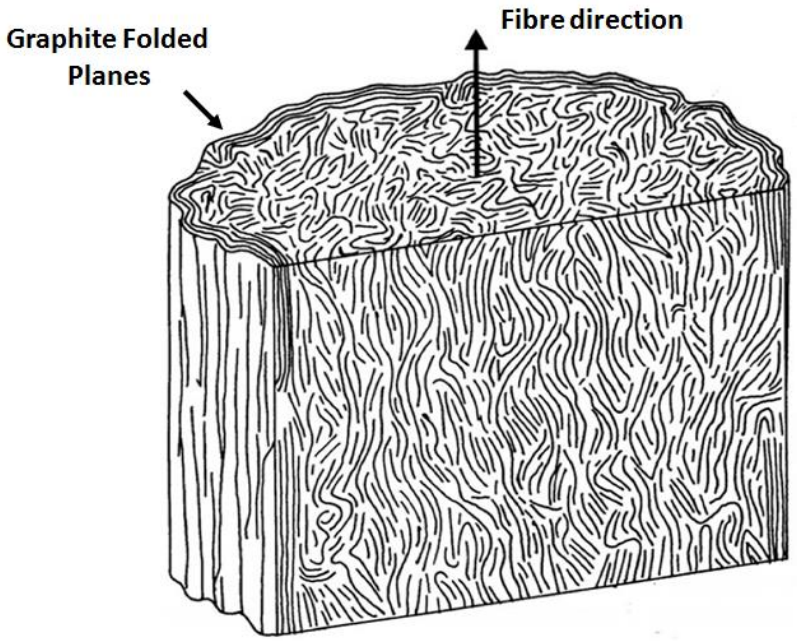

Figure 1 Typical microstructure of PAN-based carbon fibre, adapted from [16].

Although fibres have a strong impact on mechanical behaviour, the matrix also influences the performance of composites. Some properties, such as transverse stiffness and strength, are matrix dominated. A stiffer matrix with higher shear strength leads to more localised stress concentrations around fibre breaks, which will increase the longitudinal tensile strength [19]. The properties of the matrix also determine the allowable service conditions for the composite including temperature range, chemical resistance, moisture abrasion and weathering capability.

Matrix types are mainly split up into thermoplastics and thermosets and selecting one type or another implies changes in the manufacturing route and composite properties. Basically, the differences between thermoplastics and thermosets are originated in the arrangement of the polymeric chains and the type of chemical bonds which links one polymer chain to another. For thermoplastics, the intermolecular forces weaken rapidly with increased temperature, yielding a viscous liquid. While in thermosets, the chemical bonds are irreversible, causing the decomposition of the material as temperature increased rather than melting [20].

Thermoplastic composites offer shorter cycle times and improved toughness and recyclability but they usually have impregnation difficulties due to higher viscosities, and their poorer fibre/matrix interface due to the lack of chemical bonds [21]. On the other hand, thermoset resins are the most common resin systems used in composites because their

ease in processing and a wide range of performance. The thermoset resins available in the market are polyesters, vinylester, epoxy, and phenolic resins. Epoxy resins are considered high-performance resins and they are used in most critical applications because their elongation to failure and higher service temperature are superior to most other commonly used thermoset resins.

2.2 Manufacturing Process – Autoclave

Composite materials can be consolidated through different manufacturing processes. The selection of the process depends on the type of matrix and fibres, the temperature required to cure the matrix and the cost-effectiveness. Each manufacturing process imposes particular limitations in the production of the desired structure considering cost, production volume, production rate, quality and performance. Manufacturing methods include: hand layup, prepreg layup, bag moulding, autoclave processing, compression moulding, resin transfer moulding (RTM), vacuum-assisted resin transfer moulding (VARTM), pultrusion, and filament winding. Autoclave processing is the consolidation method implemented in this thesis and it will be described below.

The autoclave is used in the manufacture of high-performance structures with moderate production quantities. It is widely used to manufacture critical parts in aerospace, automotive and wind energy industries, such as wings and fuselage of the aircrafts, the chassis of racing and luxury cars and blades of wind turbines. The majority of autoclaves for composite manufacturing are cylindrical pressure vessels with domed ends, one of which is the door or entrance. Large-diameter autoclaves require extremely thick walls and become very expensive. Most research and development autoclaves are about 1m in diameter, while production autoclaves run from about 1 to 8 m in diameter. Figure 2 shows the giant autoclave (8.5 meters wide by 37 meters long) designed exclusively for Boeing to manufacture the wings of the next generation of 777 aircrafts, the 777X, which will be the world's largest and most efficient twin-engine jet. However, what makes autoclave an important manufacturing process for these industries? the answer is related to porosity levels and volume fractions of fibres. A high fibres volume fraction and low levels of voids are essential for good structure performance. During the autoclave process, a positive pressure is applied during the temperature cycle, the pressure allows to squeeze the resin excesses and collapse any voids that may develop during the resin cure. Autoclave coupled with preimpregnated fibres technology (known as prepregs) allows achieving typical fibre volume fractions of 54% (even higher) and level of porosity lower than 2% (threshold to accept or reject a manufactured aerospace part) [22],[23].

Autoclave processing is an extension of the vacuum bag technique, providing higher pressure than available with a vacuum. The laminae are laid up in a mould and resin is spread (in the case of non-prepregs), release film or a release agent is used on both sides of the laminate to prevent it from sticking to the mould or the breather. The breather helps distribute the vacuum and channels the volatiles and excess resin to the vacuum port. Finally, the laminate is then covered with a flexible bag, which is perfectly sealed to the tool, see Figure 3. The tool–laminate assembly is placed in an autoclave, the augmented

pressure combined with vacuum causes increased wetting, flow of the resin and transport of volatiles allowing minimising porosity and voids, see Figure 4.

Figure 2 Giant Autoclave for Boeing 777X, adapted from www.boeing.com.

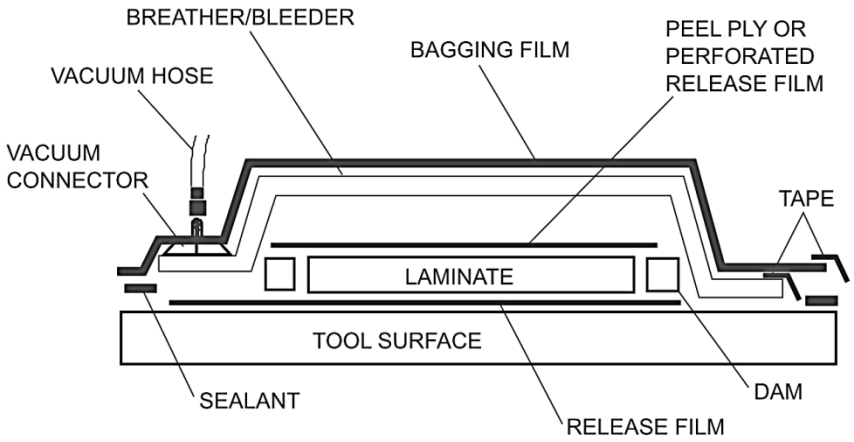

Figure 3. Component and tooling prepared for autoclave processing, adapted from [11].

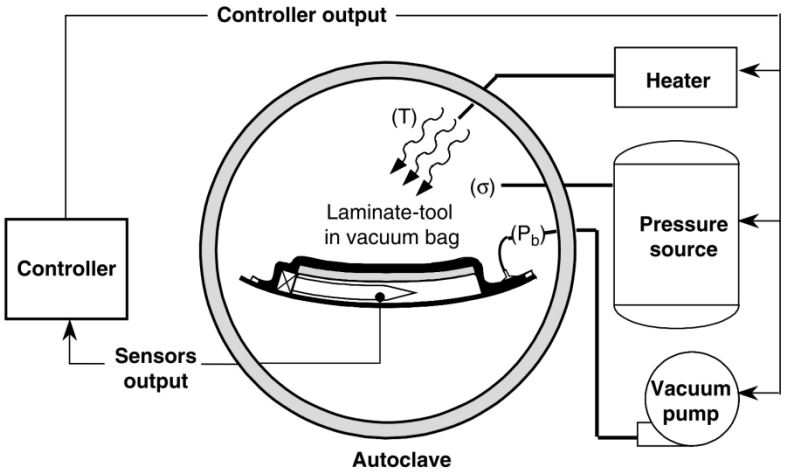

Figure 4 Typical autoclave processing system, adapted from [22].

2.3 Failure Mechanisms in Fibre Composites

The loss of functionality of a structure manufactured with composites materials can be generated for many reasons such as moisture absorption, defects produced during the manufacture, thermal fatigue, chemical degradation, among others. However, this section is dedicated to explaining the damage mechanisms produced under tension and bending.

2.3.1 Tensile Damage Mechanisms

The failure of composites subjected to tension loading is controlled by the development of fractures in the fibres parallel to the axis force [24]. Because of the presence of flaws, fibre strength is variable and often described by a probability function, being the Weibull distribution the common choice to characterise fibre strength. According to Rosen [24], when fibre breaks the surrounding fibres are subjected to stress concentrations. This stress increment is in the range of 5–15% close to the fibre break but rapidly decreases with increased distance from the broken fibre [25],[26]. If this increment in the stress is enough to break new fibres, a cluster of broken fibres is generated, which grows further upon loading. When this cluster reaches a certain size, it propagates unstably and leads to the final failure of the laminate. Figure 5 shows schematically this failure mechanism, in Figure 5a all the fibres are intact and the stress distribution is homogenous. In Figure 5b a first fibre is broken and stress concentrations are produced in the surrounded fibres. Subsequently, a cluster of broken fibres is produced (see Figure 5c), which grows unstably leading to the failure of the whole composite, Figure 5d.

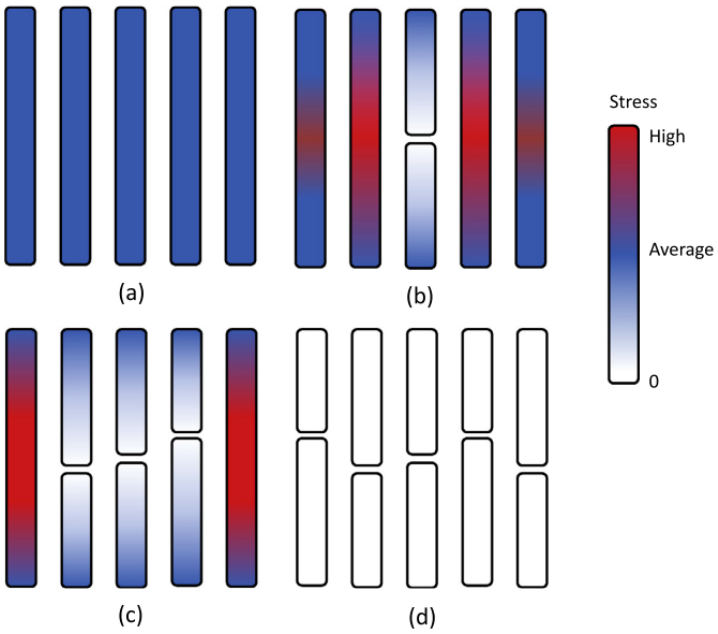

Figure 5 Schematic representation of the failure development in unidirectional non-hybrid composites: (a) all fibres intact, (b) one broken fibre, with the surrounding fibres subjected to stress concentrations, (c) development of a broken fibre cluster, and (d) crack propagation and final failure, adapted from [7].

Despite the final failure of composites in tension is dominated by the formation of clusters of broken fibres, other failure mechanisms also contribute to the degradation of the composite. Matrix cracking is common damage in composites due to the lower strength of the matrix. In unidirectional composites where all the fibres are oriented in the loading direction, matrix cracking is commonly produced by the local stress concentrations around the fibre fractures, however, it has been demonstrated that the influence of matrix cracking is negligible in the final failure of unidirectional composites [27]. On the other hand, for multidirectional composites where plies can be oriented in different directions, matrix cracking plays a more important role especially in the plies oriented at an angle out of the loading axis (off-axis plies). For multidirectional composites, cracks are generated at a lower applied strain under tensile loading, promoting other failure mechanisms such as interlaminar delamination and the formation of clusters of broken fibres [28],[29]. Experimental results have shown that cracks induce local stress concentrations at crack tips [30],[31], when the cracks reach an interface between two plies and the stored energy in the crack tip is higher than the interlaminar toughness, the crack propagates through the interface producing delamination, see Figure 6a. On the other hand, if the interlaminar delamination is not generated, the concentrated stresses at the crack tips produce a strong non-uniform stress field in the fibres parallel to the axis force, promoting a premature development of clusters of broken fibres [32], see Figure 6b. Therefore, matrix cracking in multidirectional composites not only cause a decrease in the laminate stiffness but also alter other failure mechanisms, contributing to an earlier failure of the whole structure.

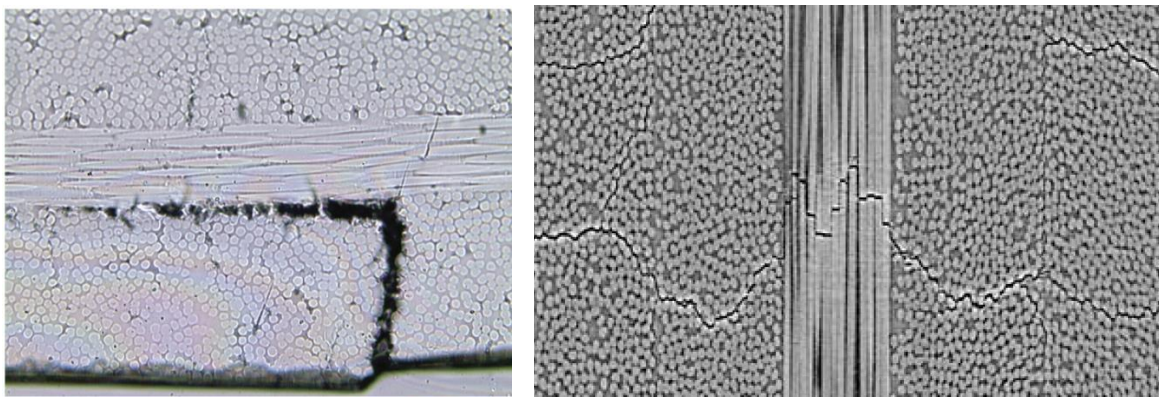

a) b)

Figure 6 a) Interlaminar delamination produced by a crack in the off-axis ply b) concatenated cluster of breaks aligned with the crack in the off-axis ply, adapted from [28] and [29] respectively.

2.3.2 Bending Damage Mechanisms

When a fibre composite is loaded under bending, different regions through the thickness are subjected to tensile or compressive stresses depending on the location of the neutral axis. The stresses under bending produce different damage mechanisms in the tension and compression regions. However, due to the compressive strength of fibre composites is generally 50% lower than their tensile strength [33], it is common that the failure initiates on the compression side. The flexural failure modes either in compression or tension are the same as those found in a pure compressive or tensile test. Kinking and microbuckling are some of the damage modes in the compression side, but depending on the interface strength delamination also occurs [34]. While the tensile failure mechanisms are comprised of fibre fracture, matrix cracking and delamination, which have been described before.

In the microbuckling mode, the compressive failure is assumed to be triggered by the instability of the fibres embedded in the matrix. While, in the kinking mode, the compressive failure is considered to be a result of a plastic shear deformation associated with the rotation at a specific angle of initially misaligned fibres within a certain band [35], see Figure 7.

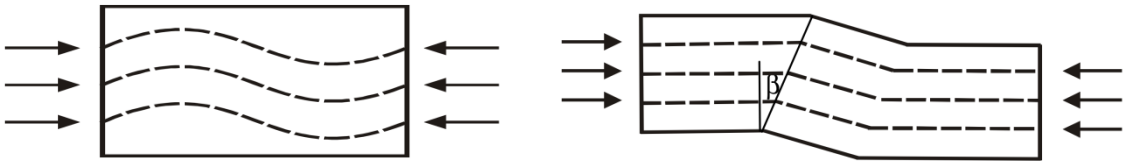

a) b)

Figure 7 Flexural failure modes a) microbuckling mode, b) kink ban mode, adapted from [35].

2.4 Thin-ply Composites

Despite continued growth in the use of composites in structural applications, premature failure modes such as uncontrolled cracking and delamination, limit their use in critical components. If cracking could be controlled and delamination suppressed, there will be a further incentive to use laminated composite structures in favour of other structural materials, like metals. Thin-ply carbon laminates emerged in the late-1990s to address these issues [36]. Thin plies are defined as those with thicknesses < 100μm and ply areal weights < 100 g/m^2, being the thinnest commercially available unidirectional carbon thin-ply prepreg with a fibre areal weight of just 15g/m^2 [37],[38]. Thin-ply composites are attracting growing interest, especially in aerospace applications because of their superior mechanical properties. Including higher initiation and ultimate strengths, improved homogenisation, increased stacking sequences possibilities for a predefined laminate thickness and further weight reduction keeping structural performance, which make them exceptional in weight-sensitive applications [39].

Thin-ply composites include benefits to in-plain static and fatigue properties, impact resistance, damage tolerance and potential for gradual failure. However, drawbacks like higher open-hole and notch sensitivity and lower interlaminar fracture toughness should be considered [40]. Additionally, thin plies make manufacturing more complicated since the number of plies that should be laid up to reach a specific thickness is much higher.

Several technologies can create thin-ply tows. The most widely used and cost-effective is airflow technology suggested by Kawabe et.al. [41] in 1998 and further developed by Tsai and Kawabe [42] in 2007. The method uses the conventional thick tow such as 12K filament tow, passed through a spreading machine equipped with a vacuum, which is sucking air downward through an air duct positioned between guide rolls, see Figure 8. Air flows past the fibres, the tow bends downwards due to the airflow pressure and the fibre tow momentarily loses tension, allowing the fibre tow to be spread continuously in a stable manner [43], see Figure 9. Since the airflow velocity is relatively low, the process does not typically cause significant damage to the fibre filaments. As a result, the carbon filaments are well distributed along the width of the layer, see Figure 10. The method further reduces resin-rich areas and increases the fibre volume fraction, these characteristics have shown suppress or delay damage mechanisms such as matrix cracking and delamination leading to increased strength and strain to failure [43].

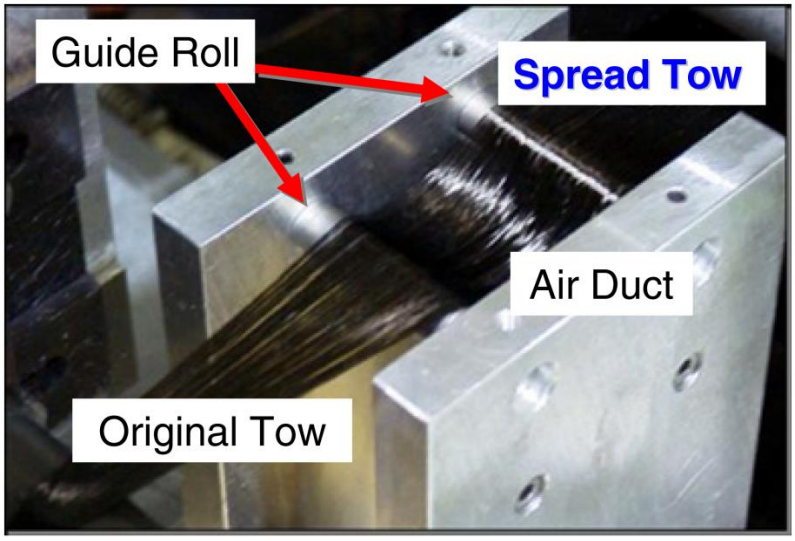

Figure 8 Schematic of the tow-spreading method with a pneumatic method, adapted from [43].

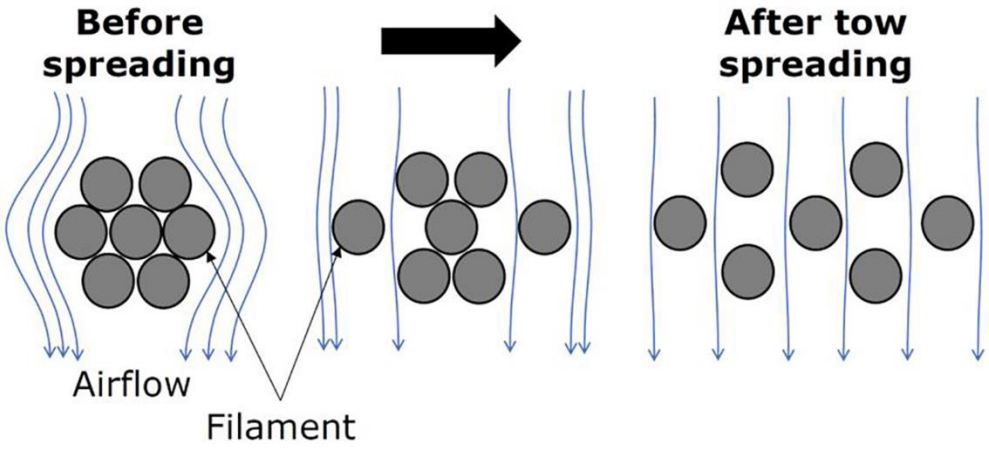

Figure 9 Schematic of the airflow tow spreading process, adapted from [43].

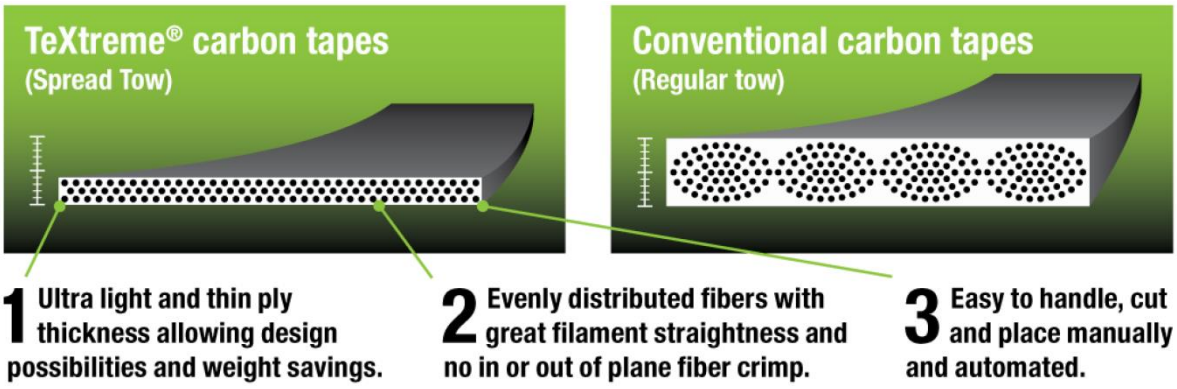

Figure 10 Illustration of the benefits of the spread tow carbon fibre tapes from conventional carbon fibre tapes, adapted from www.textreme.com/technology.

2.5 Hybrid Composites

Hybridisation provides the possibility of combining more than one type of fibre in a composite component. The study of hybrid composites was essentially motivated by the aerospace and automotive industries especially in the 1970s and 1980s [44]–[48]. The initial goal of those hybrid composites studies was to reduce the high costs of implementing carbon fibres in structural applications. Replacing carbon fibres by cheaper glass fibres can significantly reduce the cost, while the flexural properties remain almost unaffected (depending on the stacking sequence design) [7],[49].

Hybrid composites are able to achieve a better balance in stiffness, strength and toughness, combining brittle and ductile fibres. Brittle fibres provide strength and stiffness but suffer from their lack of toughness and ductile fibres have improved toughness and impact resistance but they have poor strength and stiffness. This is, for example, the case of hybrid composites reinforced with polypropylene and carbon fibres [50],[51]. Nevertheless, for most of the high-performance applications, two brittle fibres are combined, so the term brittle/ductile fibres is not appropriated. In the case of carbon/glass hybrid composites, both types of fibres are brittle and fail individually in an explosive manner. Usually, when a hybrid composite reinforced with two brittle fibres is loaded in tension, the most brittle type of fibre starts to fail first at lower strain, followed by the less brittle at higher strain. Then, low strain (LS) fibres and high strain (HS) fibres are commonly used to distinguish between the fibre types in hybrid composite materials [7],[8].

The LS and HS fibres can be combined in many different configurations. The three most important configurations are visualised in Figure 11. **a)** in the interlayer configuration, see Figure 11a, the layers of different type of fibres are stacked onto each other making a layer by layer arrangement. This is the simplest and cheapest method for producing hybrid composites [7]. **b)** in the intralayer hybrid, the different types of fibres are mixed within the layers. This is illustrated in Figure 11b, where different yarns are co-woven into a fabric. Other intralayer configurations such as parallel bundles are also possible. **c)** the different types of fibres can also be mixed or comingled on the fibre level, resulting in an intrayarn hybrid (see Figure 11c). More complex configurations can be obtained by combining two of these three configurations [8].

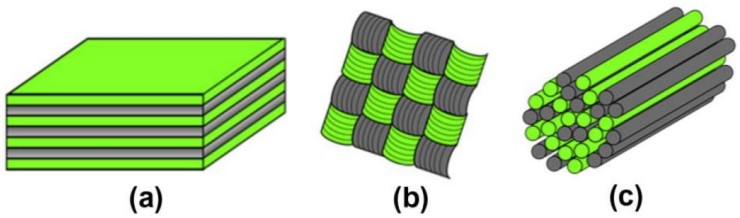

Figure 11 The three main hybrid configurations: (a) interlayer or layer-by-layer, (b) intralayer or yarn-by-yarn, and (c) intrayarn or fibre-by-fibre, adapted from [7].

It has been demonstrated that hybrid composites have greater advantages over traditional composites, the hybridisation can lead to synergetic effects obtaining properties that neither of the constituents possesses. This is the case of gradual failure in tension, most of the composites have a brittle nature, they fail individually in a catastrophic way, however, hybridising the correct materials in adequate proportion it has been demonstrated a gradual failure response under tension [6]. This will be explained in the next sections.

2.6 Hybrid Effect

Hayashi [52] first introduced the notion of hybrid effect, the author reports an apparent failure strain increment of carbon fibres when they were sandwiched in between glass layers, the failure strain of the carbon layers was 40% higher than for a composite consisting of only carbon layers. In the years after Hayashi, several works have been conducted combining high strain (HS) and low strain (LS) fibres in a single composite, establishing that hybridisation can significantly alter the failure development and thereby increase the apparent failure strain for the LS fibres in the hybrid composite [53]–[56]. In the case of carbon/glass composites, the values for this effect are typically in the range of 10% to 50% [7].

There is some controversy about the accurate measurement of the hybrid effect because of underestimations of the failure strain of the baseline LS material due to stress concentrations introduced at the grips in traditional uniaxial tensile tests. These stress concentrations produce a premature failure of the laminates from the end-tabs, leading to unrealistic failure strain values for the LS fibres. Czel et.al. [57] proposed a method to eliminate the stress concentration induced by the end-tabs at the grips. The authors used glass/carbon hybrid composites, rather than all carbon composites, to determine reference failure strains. When the carbon is sandwiched between glass plies, stress concentrations on the carbon ply is further reduced, see Figure 12a. Using this method, Wisnom et.al. [58] measured the failure strain of carbon ply changing the carbon/glass proportion. According to the results, as the carbon ply thickness increases the hybrid effect reduces and when the carbon is thick enough the failure strain of the carbon ply represents the baseline, being zero the hybrid effect, see Figure 12b.

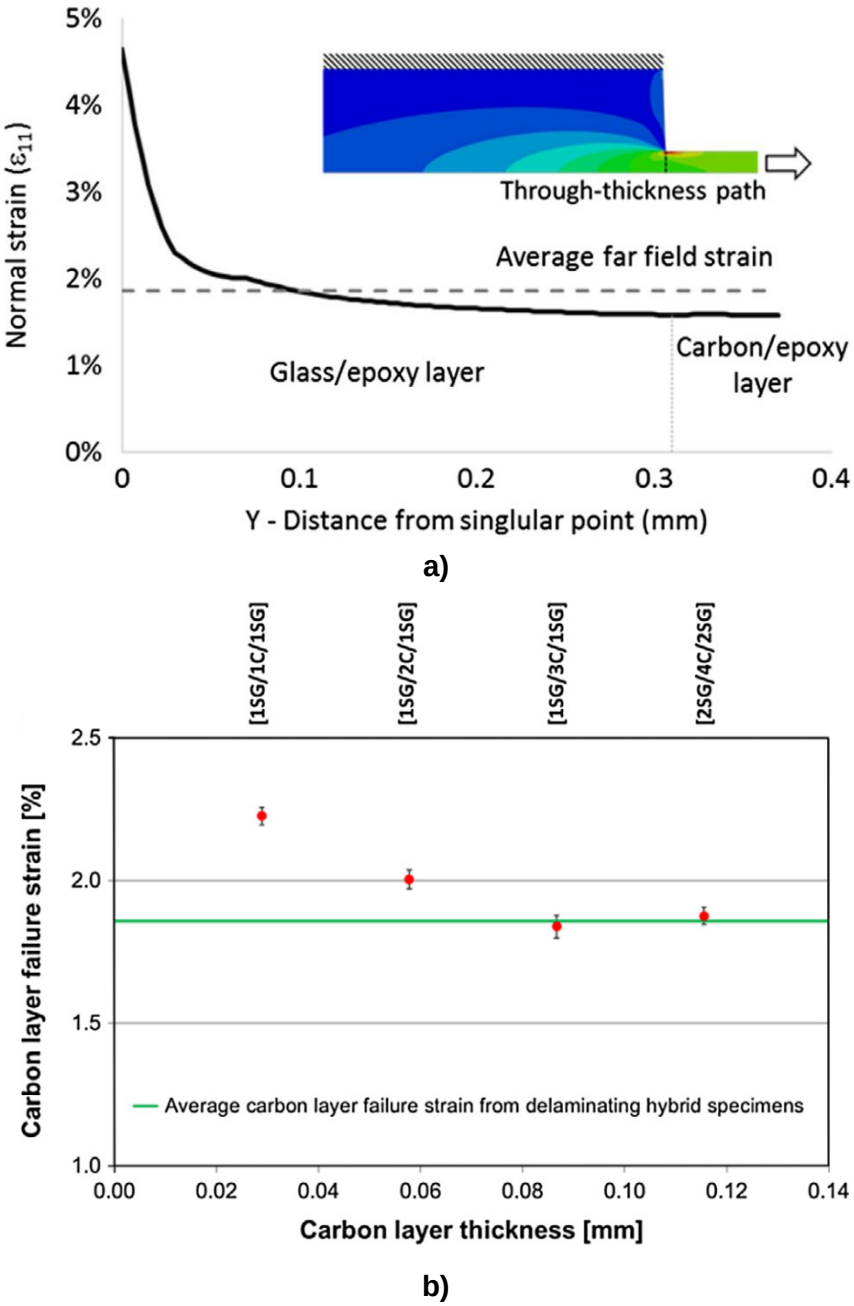

Figure 12 a) Normal strain through the thickness at the end-tab of a UD glass/carbon specimen under tension, b) dependency of carbon thickness and hybrid effect, adapted from [57] and [58] respectively.

Over the last years, there has been much interest to understand the basic mechanisms responsible for the hybrid effect, being three hypotheses the most significant considered: thermal residual stresses, dynamic stress concentrations and failure development. Different researches have argued that despite the first two hypotheses play a role in the hybrid effect, their contribution is only a small part, being the third hypothesis, “the failure development”, the main synergetic effect [58]–[60]. These three hypotheses will be briefly explained below:

Thermal residual stresses: this effect occurs in hybrid composites due to differences in the coefficient of thermal expansion (CTE) between constituents. Carbon fibres typically have a lower CTE than glass fibres, this difference generates compressive residual stresses into the carbon component which counteracts the applied stresses during a tensile test. This effect delays the failure of the carbon fibres in the hybrid composite. The thermal residual stresses are relatively small compared to the experimentally measured synergies in the failure strain of carbon and in the case of carbon/glass fibre-hybrid composites, this effect represents less than 10% of the hybrid effect [61]-[63].

Dynamic stress concentrations: intrinsically fibre fracture is a dynamic process, resulting in a change in the stress level over time, see Figure 13. Before fibre break, the stress in the adjacent intact fibres is equal to the nominal level. When the fibre breaks the stress in the nearby fibres increases to the dynamic stress level, after which it gradually dampens out to the static stress level. The reason for these dynamic effects is that a broken fibre releases its stored elastic energy and converts it into kinetic energy. This causes dynamic stress concentrations on the neighbouring fibres that exceed the static ones. The characteristics of the dynamic response of a composite with only one type of fibre are different from that of a hybrid. In the case of hybrid composites, the difference in longitudinal stiffness and density of the fibres types will change the dynamic response, causing that the stress waves to propagate at different speeds and damping the stress concentrators. Dynamic stress concentrations have received no attention at all in the past two decades and remain poorly investigated today [19],[59],[64],[65].

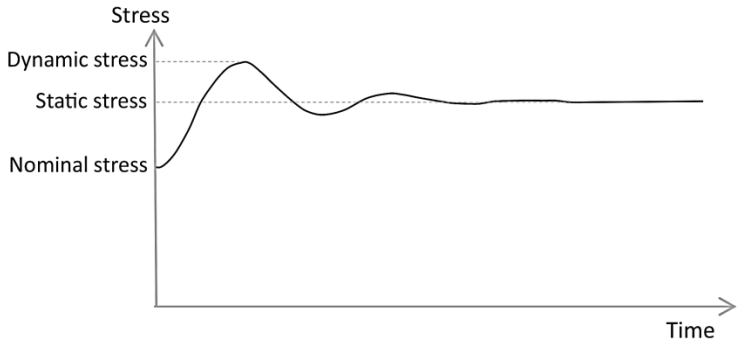

Figure 13 The stress evolution in a nearby, intact fibre as a function of time when a fibre breaks in a regular 1D packing. The dynamic stress level is significantly higher than the static stress level, adapted from [19].

Failure development: It has been extensively demonstrated that the fibres interaction changes the failure development, contributing to the synergetic increment on initial failure strain of the LS fibres (the hybrid effect) [66]-[70]. As it was mentioned before, in hybrid composites the LS fibres tend to fail first at lower applied strain producing stress concentrations in the adjacent fibres and increasing the probability of failure propagation [71],[72], see Figure 14. The presence of HS fibres in the adjacent fibres alters the development of the failure, reducing the stress concentration and delaying the fracture propagation. Different works have demonstrated that the failure strain of LS fibres increase dramatically with a higher relative fraction of well-dispersed HS fibres in the hybrid composite

[60],[73],[74]. This concept is also applied at the ply-level (interlayer hybrid configurations) where dispersion can be modified by alternating the stack design of the laminate and the relative fraction is changed reducing or increasing the plies thickness [6],[9],[75]. According to Swolfs et.al. [74], not only the relative fraction and dispersion of fibres play an important role in failure development but also variation in the stiffness of the fibres modify the stress concentrations on the LS fibres and change the hybrid effect. “Increasing the stiffness of the hybridisation fibre reduces the stress concentrations on the low elongation fibre and may also enlarge the hybrid effect” [74].

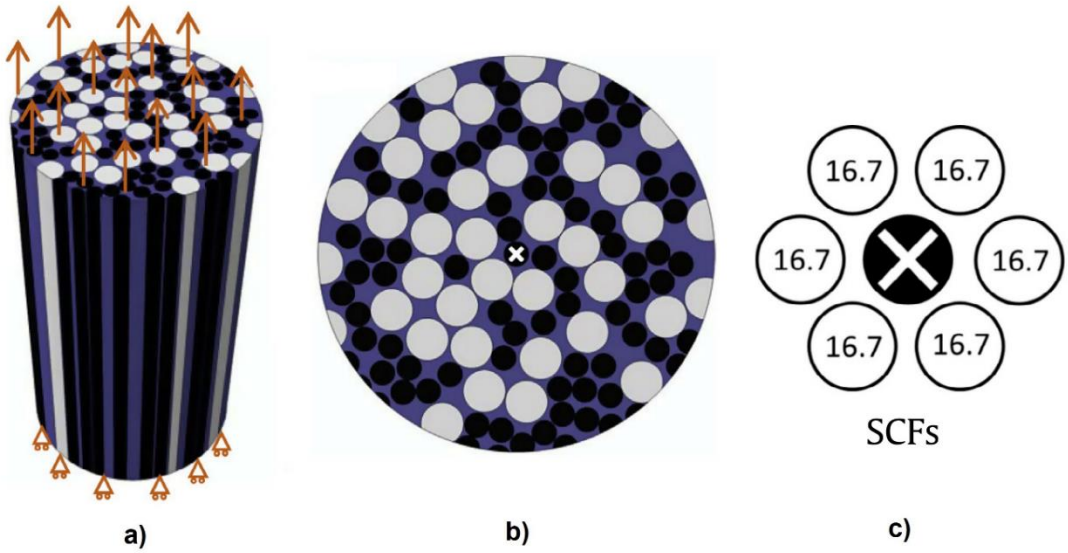

Figure 14 Illustration of the models with carbon fibres in black, glass fibres in white and matrix in purple, the white crosses indicate fibre break, a) 3D representation of a glass/carbon intermingled fibres composite b) random distribution of fibres c) stress concentration factors (SCFs) in adjacent layers produced by the broken carbon fibre in a hexagonal packing, adapted from [27],[72].

2.7 Gradual Failure in Unidirectional (UD) Hybrid Composites

The availability of thin-ply prepregs has attracted researchers to develop thin-ply hybrid composites [6],[9],[76],[10]. These hybrids are made of thin carbon prepregs (~0.03 mm) and standard thickness glass fibre prepregs (~0.155mm), with the carbon ply located in the middle of the laminate. These types of configurations have led to synergistic effects such as gradual failure. Composites which fail gradually are characterised not only by an enhancement to the failure initiation strain of the carbon plies but also a new failure mechanism is developed, called fragmentation [6]. Carbon fragmentation is the results of the capacity of thin carbon plies to delay and constraint damage mechanisms such as matrix cracking and delamination due to its low energy release rate [77]. As a result, multiple fractures in the carbon ply can occur stably followed by local delamination. Figure 15 shows the damage pattern, where well-bonded areas appear black and the locally delaminated areas just around the cracks in the carbon layer are visible as the yellow stripes due to the

translucent nature of the glass/epoxy outer plies of the hybrid laminate. The yellow stripe corresponds to the colour of the epoxy resin [6].

Figure 15 Damage pattern for thin ply hybrid composite [SG/C_2/SG]s, own source.

Czél et.al. [6],[10] demonstrated gradual failure in glass/carbon hybrids. The authors showed that if the carbon ply is thin enough (less than about 0.06 mm which is two thin carbon plies), catastrophic delamination propagation around the first carbon ply fracture can be suppressed and therefore fragmentation occurs. The authors analysed the change in failure modes as the thickness of the carbon ply increases, as it is shown in Figure 16. Four different configurations were tested showing similar initial linear stress-strain response up to an initial fracture of the carbon ply and, after this point, the behaviour depends on the number of carbon plies. For configurations 1 and 2 gradual failure is obtained and according to the authors, multiples fractures in the carbon ply occurred. The fractures in the carbon plies produce a loss of the stiffness in the form of a horizontal stress plateau which is more evident for configuration 2. On the other hand, for configuration 3 and 4, where the carbon ply thickness is three and four times respectively, a load-drop corresponding to delamination is seen. This delamination extended out at the carbon-glass interfaces immediately after the first carbon ply fracture, concluding that the dominant failure mechanism is delamination rather than carbon fragmentation. A plateau is also observed after load drop, which corresponding to further growth of the delamination. For all configurations, a final stress increment is seen which is produced by a load transfer from the damaged carbon ply to the undamaged glass plies.

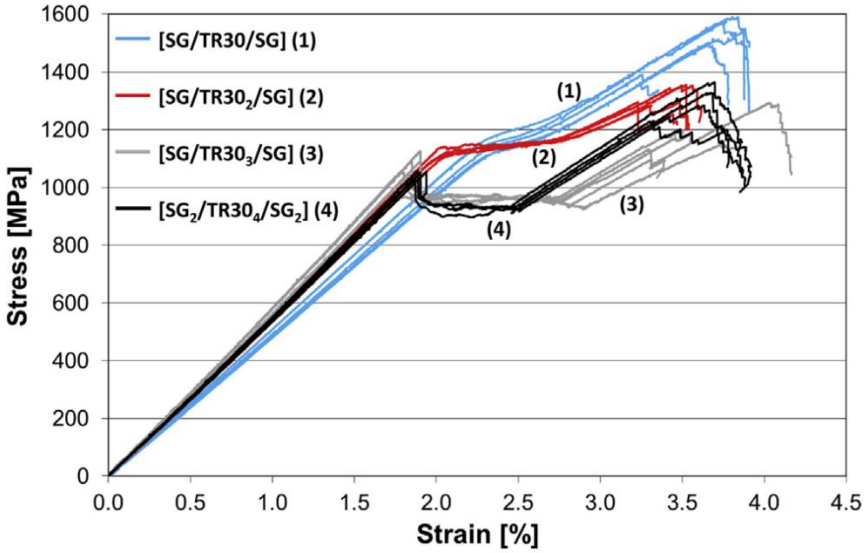

Figure 16 Tensile stress-strain graphs of S-glass/TR30 carbon configurations, adapted from [10].

Figure 17 summarises the main features of a glass/carbon hybrid composite with gradual failure. The knee point represents the initiation of carbon failure by fragmentation, where there is enough number of fractures to significantly reduce the stiffness of the laminate. In hybrid composites with gradual failure, the knee point is used to quantify the hybrid effect. When fragmentation reaches the saturation point, the carbon ply is stably pulled out and its loading capacity is further reduced. Then, a stress increment in the stress-strain curve is observed when the load is mostly transferred to the undamaged glass plies. Finally, the composite fails. The pseudo-ductile strain measures the favourable gradual failure and it is defined as the extra strain obtained due to gradual failure and is measured between the final failure point and the initial slope line at the failure stress level.

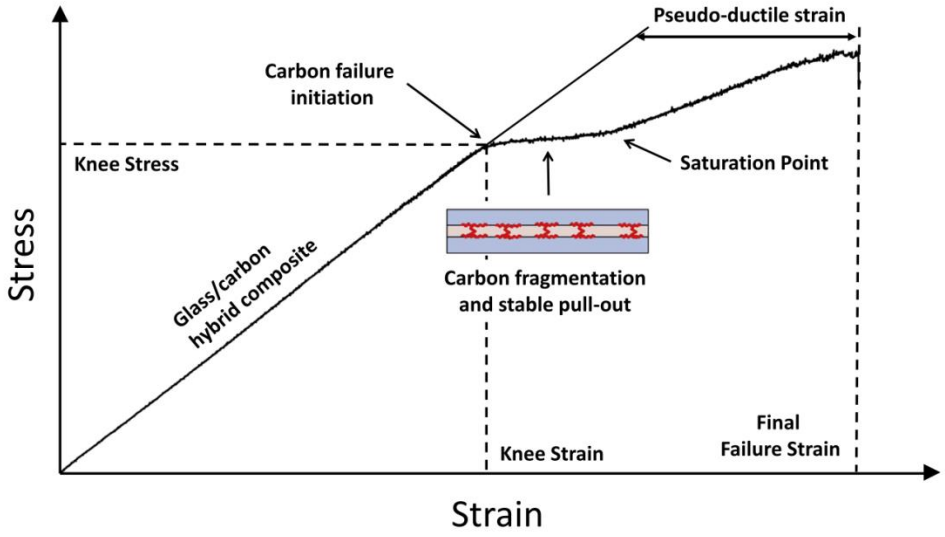

Figure 17 Illustration of stress-strain curves of thin ply carbon/glass hybrid composites with gradual failure, own source.

Jalalvand et.al. [9],[76],[77] further analysed the failure mechanisms involved in the hybrid composites. The authors recognised four types of failure modes for unidirectional hybrid composites under tension. These are schematically illustrated in Figure 18 alongside their stress-strain schematic response: 1) premature failure of high strain material (HSM) after the first crack in the low strain material (LSM), 2) catastrophic delamination at the interface between the LSM and HSM after the first crack in the LSM, 3) fragmentation of the LSM and 4) fragmentation of the LMS followed by limited dispersed delamination. The first two failure modes are unfavourable and their behaviour in the stress-strain graphs is characterised by a significant load drop, leading to mechanical properties lower than the constituents. On the other hand, damage modes 3 and 4 are desirable because they provide integrity and load carrying capacity while the laminate is gradually deteriorating. It is worth remembering that for a glass/carbon hybrid composite, glass plies correspond to the high strain material (HSM) and carbon plies correspond to the low strain material (LSM). It is because usually the failure strain for carbon fibres is lower than the failure strain of glass fibres.

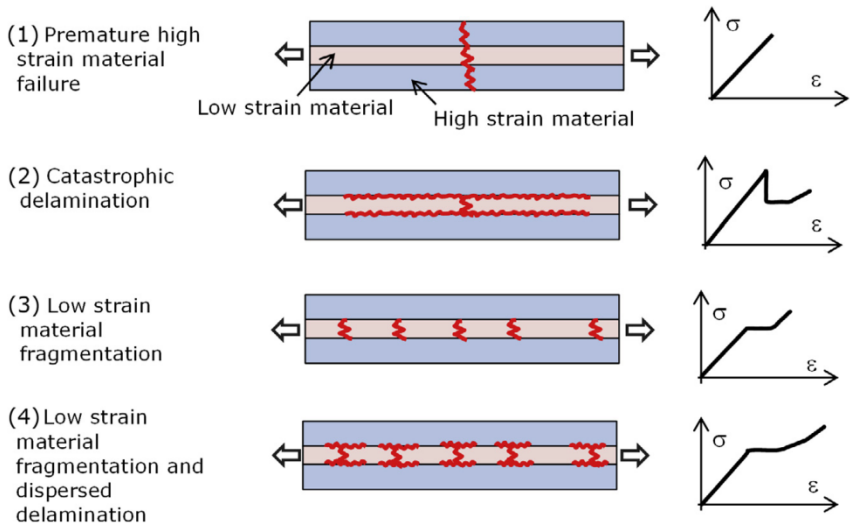

Figure 18 Different damage scenarios of UD hybrid laminates, adapted from [76].

According to [78], to assure gradual failure for UD hybrid interlayer composites two criteria should be met:

1. The outer HSM layers need to be thick and strong enough to take the full load after LSM fractures and it is pulled-out. Figure 19 shows schematically the load transference and the stress variation between LSM and HSM considering a crack in the LSM. If this criterion is not met the fracture will extend toward all thickness producing failure mode 1 in Figure 18. According to that, Eq. (1) should be considered:

$$\sigma'_H > \frac{\sigma'_L(E_H t_H + E_L t_L)}{E_L t_H} \qquad \text{Eq. (1)}$$

Where E_H is the initial modulus of the HSM plies, E_L is the initial modulus of the LSM ply, t_H is the thickness of one HSM layer, t_L is the half of thickness of the LSM layer (as shown on Figure 19), σ'_H is the failure stress of the HSM plies and σ'_L is the failure stress of the LSM layer.

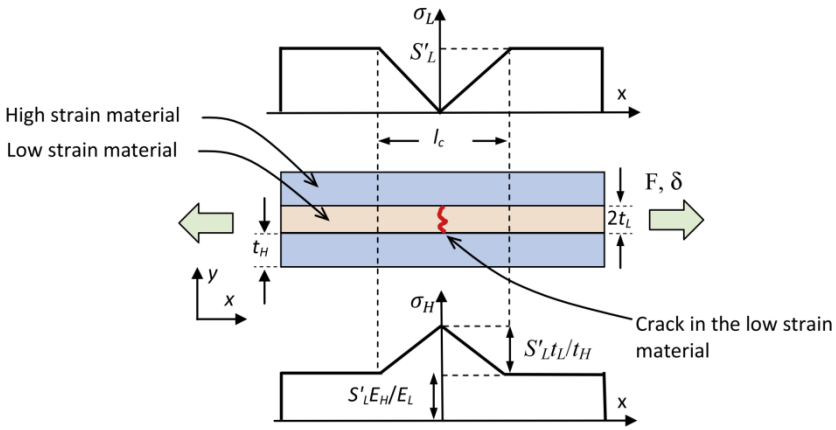

Figure 19 The stress variation in the low and high strain materials around a crack in the low strain material, where $\acute{S}_L$ is the average strength of LSM and l_c is the critical length where the stress field is influenced by the fracture in the LSM, adapted from [76].

2. The energy release rate (GII) at the expected failure strain of the LSM must be lower than the mode II fracture toughness (GII_C) of the LSM/HSM interface to avoid catastrophic delamination. If this criterion is not met, catastrophic delamination occurs, mode 2 in Figure 18. This criterion is defined by Eq. (2).

$$G_{II} = \frac{\varepsilon_L'^{\,2} E_L t_L (E_H t_H + E_L t_L)}{2 E_H t_H} < G_{IIC} \qquad \text{Eq. (2)}$$

Where E_H, E_L, t_H and t_L were defined previously according to criterion 1 and ε_L' corresponds to the failure stress of the LSM.

These criteria show that not only the thickness of the HSM plays an important role in the gradual failure but also the layup configuration and properties of each material influence the stress-strain response; in other words, the stiffness, failure strain, modulus and thickness of the constituent plies determine the failure type.

2.8 Damage Mode Maps

In [76] Jalalvand et.al. proposed a novel analytical approach for predicting all possible damage modes, identifying the required stress level for each damage condition. Using this analytical method, the damage process of the UD hybrid can be predicted based on the order of the required stress for each damage mode. Table 1 summarises the stress levels at which damage modes are expected to occur, where $\sigma_{@LF}$, $\sigma_{@del}$ and $\sigma_{@HF}$ correspond to the stress level associated with LSM, HSM and delamination failure, α is Young's modulus ratio of the low to high strain material, β is the thickness ratio of the low to high strain material, *V* is the volume of the specimen and *m* is Weibull modulus the strength distribution of the HSM. For more details refer to [76].

Table 1 Summary of the stress in the laminate for each damage mode, adapted from [76].

Damage mode	Equation	
Fragmentation in the low strain material	$\sigma_{@\mathrm{LF}} = \acute{S}_{\mathrm{L}} \frac{\alpha\beta + 1}{\alpha(\beta + 1)}$	Eq. (3)
Delamination	$\sigma_{@\mathrm{del}} = \frac{1}{1+\beta} \sqrt{\frac{1+\alpha\beta}{\alpha\beta} \frac{2 G_{\mathrm{IIC}} E_{\mathrm{H}}}{t_{\mathrm{H}}}}$	Eq. (4)
Failure in the high strain material	$\sigma_{@\mathrm{HF}} = \frac{S_{\mathrm{H}}}{K_t} \frac{1}{(\beta+1)\sqrt[m]{V}}$	Eq. (5)

Using the equations proposed in Table 1, the authors defined a procedure for finding the damage response of the UD hybrid composite based on the order of the required stress for the damage modes. The procedure for finding the damage response is shown in Figure 20. Initially, the stresses at which the low and high strain materials fail are compared and then

the stress at which delamination propagates is considered. After considering all the inequalities the four damage scenarios of Figure 18 are obtained.

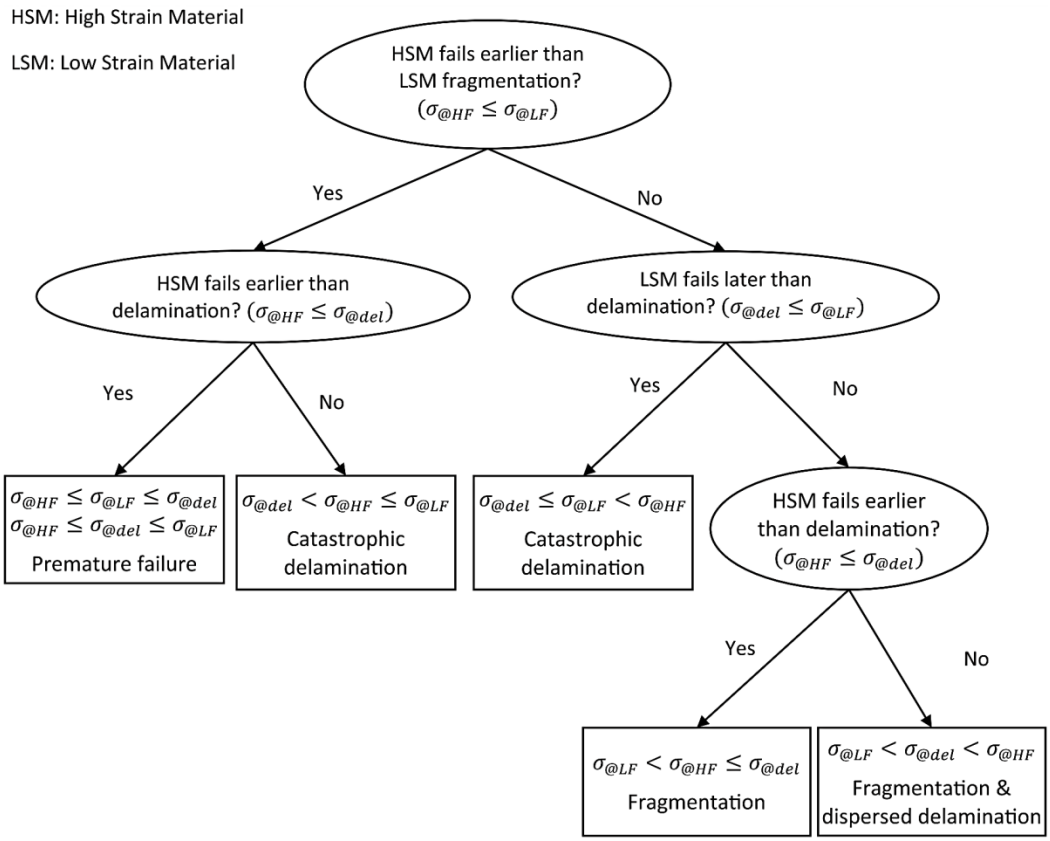

Figure 20. The procedure for finding the hybrid's damage process based on the order of required stresses for each damage mode, adapted from [76].

Using the analytical method and the equations proposed above, Jalalvand et.al. [9] identified correlations between the damage modes and the geometric parameters of any specific material combination. Using those correlations, damage mode maps have been proposed as an efficient method to find optimum configurations of different UD hybrid combinations to achieve gradual failure. Figure 21 shows schematically a damage mode map, where the horizontal axis in the map corresponds to the relative LSM thickness, the thickness of LSM plies divided by the total thickness of the hybrid laminate, and the vertical axis shows the absolute thickness of the LSM plies. The map shows the different damage sceneries separated by boundaries, correlating the damage type zone with the geometric parameters (total LSM proportion and absolute LSM layers thickness). The coloured bar in the map indicates the pseudo-ductile strain (ε_d), defined previously in Figure 17, which measures the favourable gradual failure for damage modes 3 and 4. As it is shown in Figure 21, the pseudo-ductile strain is a maximum close to the intersection of the three boundaries between different damage modes. The pseudo-ductile strain (ε_d) for damage modes 1 and 2 is zero because the loss of integrity due to premature failure and catastrophic delamination respectively.

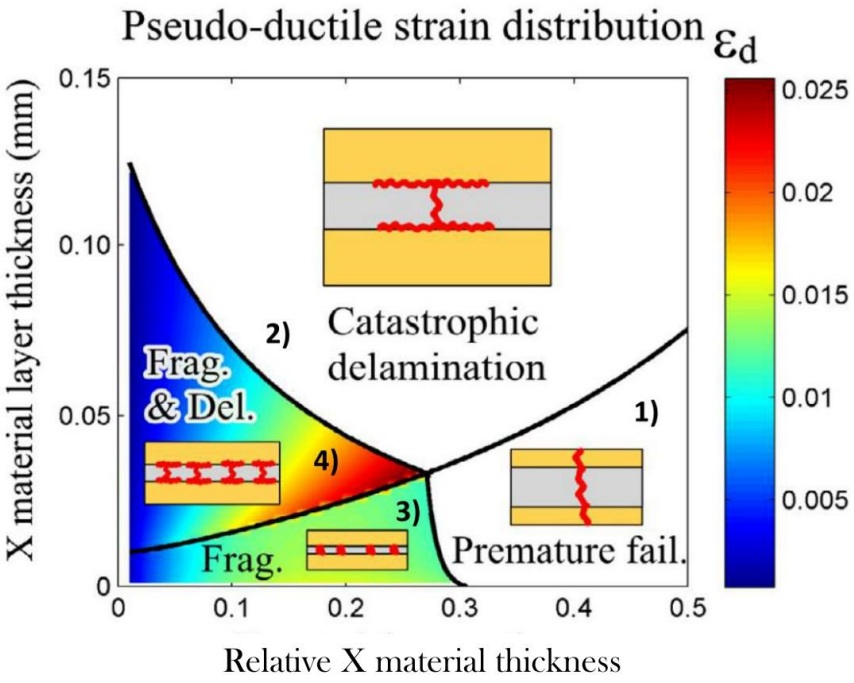

Figure 21 Damage mode map of an arbitrary hybrid combination, adapted from [9].

2.9 Gradual Failure in Multidirectional Hybrid Composites

The multidirectional composites bring the opportunity to increase the transverse strength locating fibres in different directions where loads are applied. Multidirectional composites are widely used in the industry because most of the structures are subjected to multiple loading orientations and the exact load direction is not always known. Nevertheless, most of the results in the literature have been focused in unidirectional composites and just a few works have been proposed to study gradual failure in multidirectional laminates [75], [79]–[81].

Czel et.al. [81] confirmed gradual failure for multidirectional composites demonstrating fragmentation in plies oriented in the load direction. The authors proposed two carbon/carbon hybrid composites (T1000/XN-80 and MR60/XN-80) made out of ultra-high modulus XN-80 (LSM) and intermediate modulus T1000 and MR60H (HSM) carbon/epoxy thin-ply prepregs in a quasi-isotropic configuration $[45_H/90_H/\text{-}45_H/0_H]_S$. Where H in the layup stands for hybrid and means that each layer is a sandwich of two high and one low strain material layers, see Figure 22. Authors achieved gradual failure in both T1000/XN-80 and MR60/XN-80 hybrid configurations, Figure 23 left side. The strain-stress curve produced by T1000/XN-80 shows all the main features of gradual failure, a knee point, a stress plateau and a stress increment produced by the load transfer between the T1000 and XN-80. On the other hand, MR60/XN-80 shows an ‘‘elastic-plastic” type response without a stress increment at the end of the curve and a shorter stress plateau. According to the authors, this condition is produced because the MR60/XN-80 has a higher mode II toughness,

suppressing interfacial damage between the XN-80 and the MR60 layer, resulting in higher stress concentrations in the intact MR60 around XN-80 fractures and decreasing the safety margin. Czel et.al. also characterised the damage mechanisms responsible for the favourable gradual failure using X-ray computed tomography (CT). The authors identified a failure mechanism which is not presented for UD hybrid composites called free-edge delamination, which originates from the edges of the laminates and grows along the width, see Figure 23 right side. This failure mechanism causes loss of laminate integrity and it is responsible for the load-drops present in the stress plateau of T1000/XN-80 configuration.

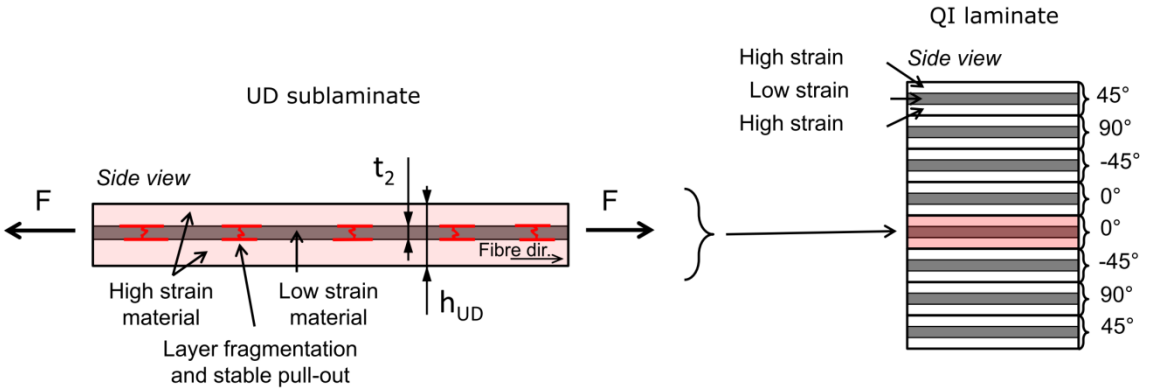

Figure 22 Schematic showing the sub-laminate concept for multi-directional composite plates, adapted from [81].

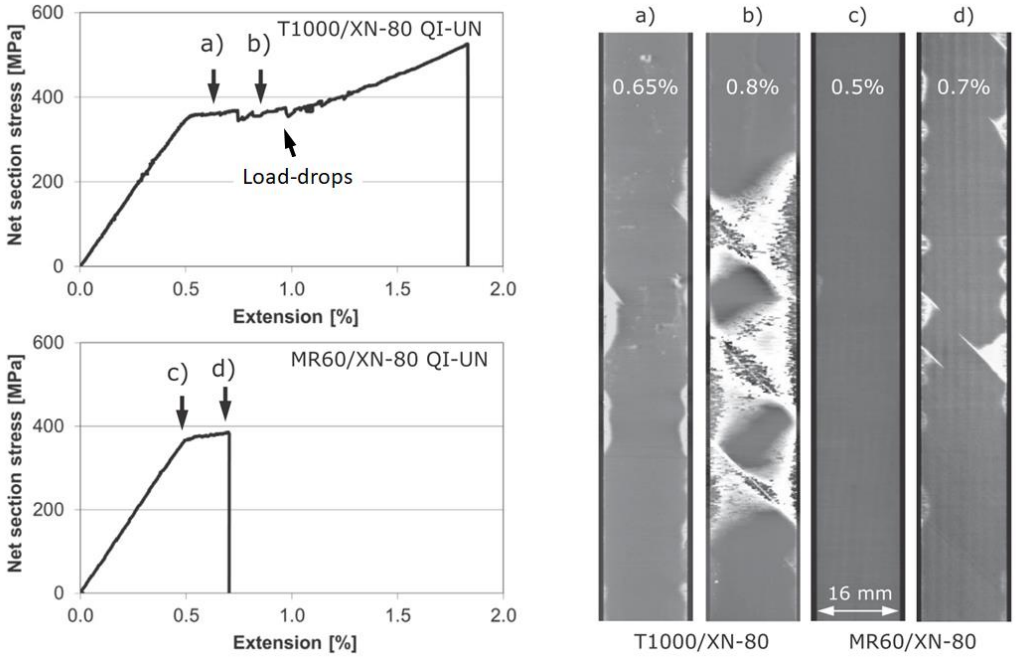

Figure 23 X-ray CT scans showing inter-sublaminate damage in QI-UN laminate specimens after tests interrupted at specific strains: (a) T1000/XN-80 QI-UN 0.65% (at plateau, before any stress-drop), (b) T1000/XN-80 QI-UN 0.8% (after the first stress-drop), (c) MR60/XN-80 QI-UN 0.5% (at knee point), (d) MR60/XN-80 QI-UN 0.7% (at plateau, before any stress-drop), adapted from [81].

Free-edge delamination in multidirectional hybrid composites was studied by Jalalvand et.al. [75]. The authors proposed a new concept to design multidirectional hybrid layups avoiding this damage mode. The concept is based on a reduction of the energy release rates at the interfaces between the laminates, showing that when the layers are well oriented dispersed no free-edge delamination is observed. To do that, the author compared two types of stacking sequences, “orientation-blocked” and “orientation-dispersed” and using a numerical model the energy release rate for free-edge delamination in all the interlaminar interfaces was calculated. The orientation-blocked stacking sequence is similar to the design proposed previously by Czel et.al [81], where the total laminate is composed for blocks of UD hybrid sub-laminates ($45_H/90_H/-45_H/0_H$) with layers oriented in the same direction within the blocks. This is better appreciated in Figure 24a in the oriented base separation, where the layup is coloured and uses fibre angle as the parameter to separate different layers. Despite material is well dispersed, thick blocks with the same fibre orientation through the thickness are generated. On the other hand, in the orientation-dispersed stacking sequence, the layers with similar angle are distributed through the thickness, however, the material is grouped in sub-laminates, see Figure 24b.

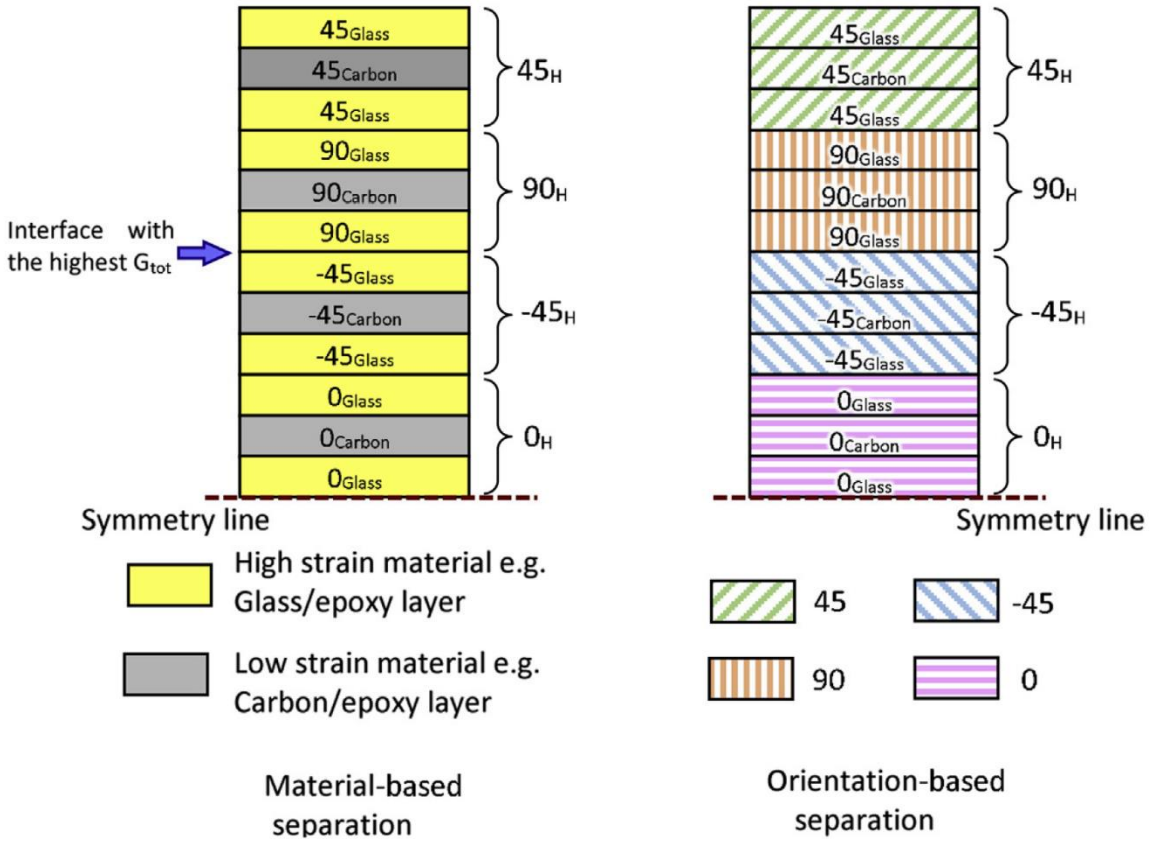

a)

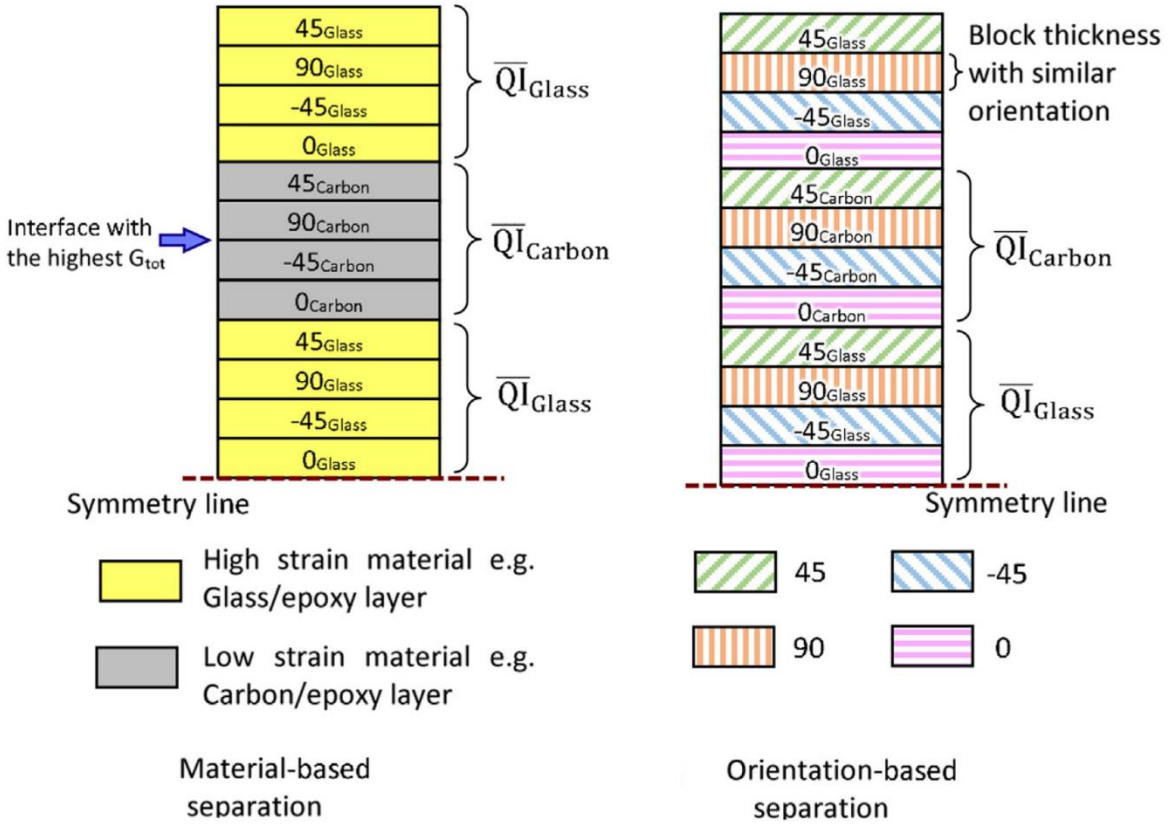

b)

Figure 24 a) Orientation-blocked stacking sequence, b) Orientation-dispersed stacking sequence, adapted from [75].

The results of the energy release rate conducted by Jalalvand et.al. [75] in the orientation-blocked and orientation-dispersed stacking sequences show that the energy release rates for free-edge delamination are significantly lower for the orientation-dispersed laminate. Figure 25 shows the total energy release rate calculated in each interface of the orientation-blocked and orientation-dispersed layups. The total energy release rate is defined as the sums of all G components ($G_{tot} = G_I + G_{II} + G_{III}$) and the authors found that delamination is shear dominated, being G_{II} the main component in the total energy. The G_{tot} values are larger in the orientation-blocked laminate especially at interfaces number 5 and 6, which are more likely to fail by delamination. The authors conduct new experiments with an orientation-dispersed layup demonstrating that the free-edge delamination is avoided with this approach.

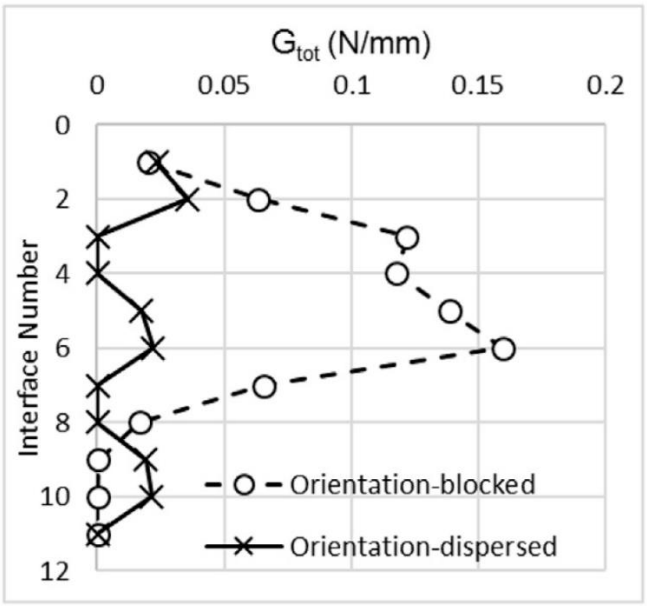

Figure 25 Total energy release rate (G_{tot}) for both orientation-blocked and orientation-dispersed layups with S-glass/USN020A carbon hybrid combination, adapted from [75].

Recently, Fotuohi et.al. [80] used the results of Czel et.al and Jalalvand et.al. to propose quasi-isotropic carbon/glass hybrid composites with gradual failure in all fibre orientations. The authors used the orientation-dispersed approach to design two types of QI lay-ups with 45° and 60° intervals, i.e. [45/90/-45/0] and [60/-60/0], using T300/epoxy thin carbon and S-glass/epoxy prepregs. The layups were loaded in different directions according to Figure 26, showing gradual failure in all the possible loading conditions with fragmentation and local delamination as the main failure mechanisms and suppressing free-edge delamination. The results of Fotuohi et.al. also show that hybrid effect change depending on the loading orientation, configurations loaded at ±60QI/0° and ±45QI/0° shows the highest knee strain for each respective configuration, but the author did not conclude about this phenomenon.

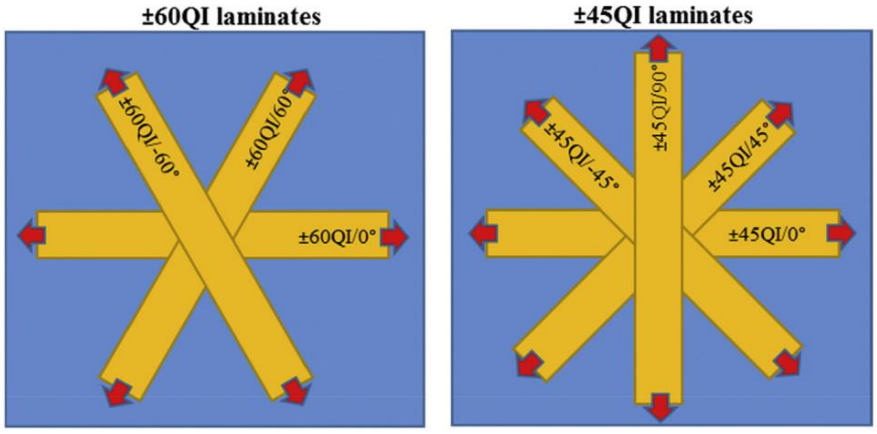

Figure 26 Schematic of the investigated laminates in a QI composite plate, the red arrows showing the loading directions, adapted from [80].

This thesis takes the work conducted by Czel et.al [81], Jalalvand et.al. [75] and Fotuohi et.al. [80] and proposes new types of orientation-dispersed quasi-isotropic carbon/glass hybrid layups. This in order to provide a new understanding of the variation of the hybrid effect (knee point) produced by changes on the loading orientation or which is equivalent to the stacking sequence.

2.10 Gradual Failure in Composites Under Bending

In bending, most of the research has concentrated on preventing failure initiation, maximising the flexural strength and modulus in both unidirectional and multidirectional hybrid composites by optimising stacking configurations [82]–[85]. Different works [86]–[89] have demonstrated that the stacking sequence plays an important role in the performance of glass/carbon hybrid composites under bending conditions. A work conducted by Dong et.al. studied the flexural properties of carbon and glass epoxy hybrid composites varying the stacking sequence according to Figure 27. The authors analysed the layups using three-point bending tests and a numerical model. They showed that layups yield the highest flexural strength when the glass layers are placed on the compressive side. Replacing lower elongation carbon fibres with higher elongation glass fibres in compression improves the overall flexural performance of the composites and delays compressive failure mechanisms [89].

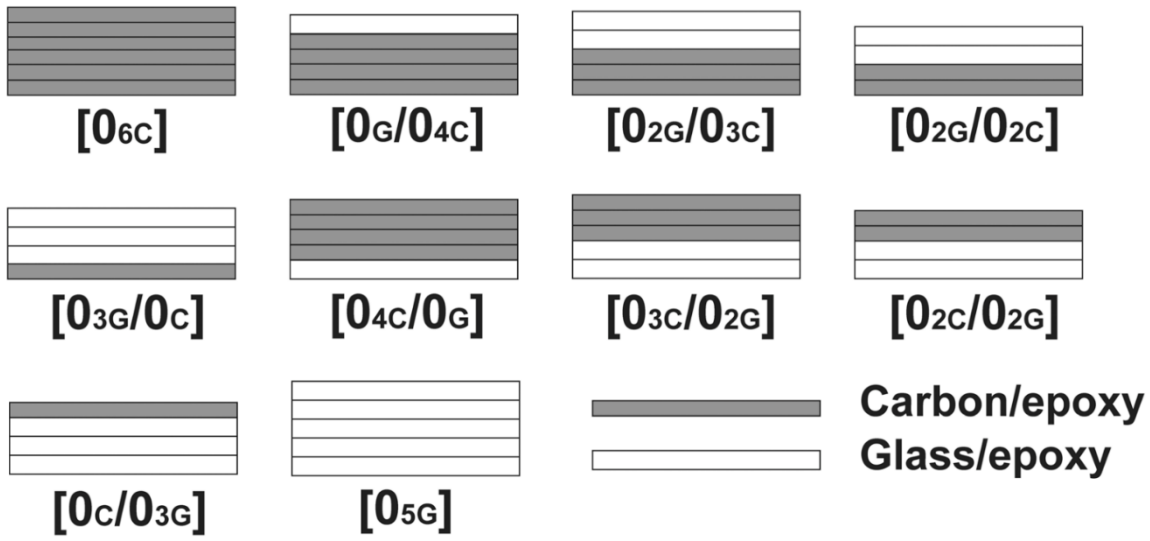

Figure 27 Stacking sequences with top laminas subjected to compression, adapted from [89].

Unlike tension loading, achieving gradual failure under bending has not been studied as extensively. Wisnom [90],[91] tested different size unidirectional non-hybrid carbon composites under four-point bending and pinned-end buckling tests and reported failure initiation in tension with a gradual splitting-off process of individual bundles of fibres and a brush-like appearance, see Figure 28. However, for larger samples, final failure was catastrophic in compression.

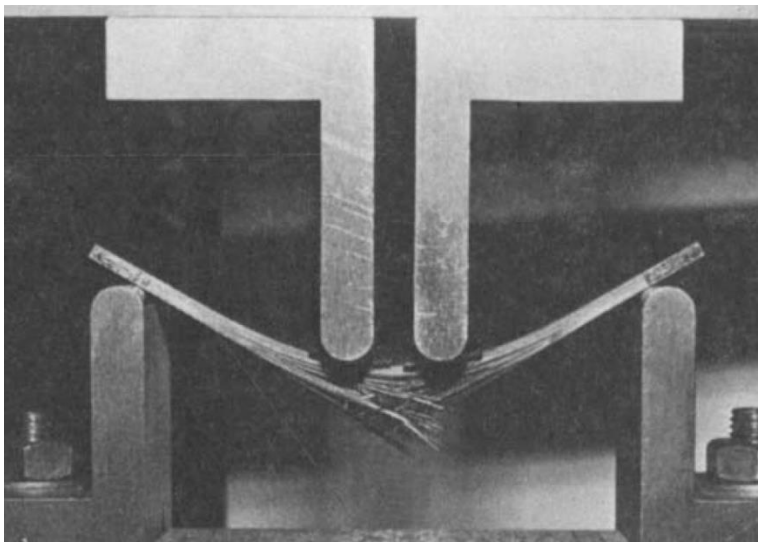

Figure 28 brush-like appearance in four-point bending specimen under load, adapted from [90].

Czel et.al. [92],[93] proposed a novel approach to measure the tensile and compressive failure strain implementing new asymmetric UD glass/carbon hybrid specimens evaluated under four-point bending. The approach achieved stable failure and fragmentation of the high (M55 carbon/epoxy) and ultra-high modulus (XN80 carbon/epoxy) unidirectional carbon plies which were located either in the compression or tension side of the hybrid composite, see Figure 29. The results also show failure strains significantly higher than those measured in conventional non-hybrid carbon/epoxy baseline specimens.

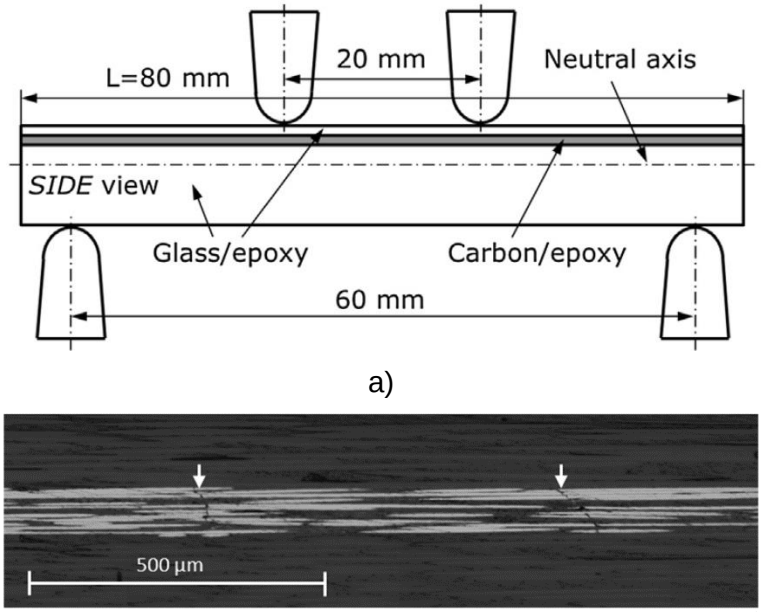

Figure 29 a) The four-point bending test setup with an asymmetric interlayer hybrid specimen, locating carbon plies in the compression side, b) stable failure and fragmentation of the carbon plies, adapted from [92].

Wu et.al. [94] followed the approach proposed in [92],[93] and evaluated a $[\pm 27_7/0]s$ configuration in compression, via a sandwich beam subjected to four-point bending and locating carbon plies in compression side. The authors reported a progressive compressive failure of the M55 carbon/epoxy plies, achieving a compressive failure strain of 0.56% which is significantly higher than the 0.26% provided by the manufacturer's datasheet.

Despite the previous researches have shown locally gradual failure in carbon plies located strategically in the tensile or compressive side, composites which achieved an overall gradual failure under bending conditions have not been well explored in the literature. This thesis proposes a novel approach to design hybrid composites with gradual failure, keeping loading capacity even under overloading conditions and obtaining high flexural displacements without catastrophic failure.

2.11 Numerical Modelling

Different numerical models have been proposed to predict the damage scenarios presented in composites. Essentially, they have been split up into two big categories: micro-level and ply-level models, see Figure 30. The first category considers the fibres and the matrix as individual entities allowing to determine fibre/matrix and fibre/fibre interactions, while the second category makes abstraction of some micromechanisms considering the fibres and the matrix as a single entity with homogenised properties [8]. Figure 30a shows an example of a micro-level model developed by Mesquita et.al. [95] which is based on the determination of fibre breaks and the calculation of stress fields to predict failure propagation and stress-strain response of the hybrid composite. On the other hand, Figure 30b shows a ply-level model developed by Jalalvand et.al. [77] which simulates the same loading condition of Mesquita et.al. The model of Jalalvand et.al. takes into account that the failure of the plies initiates when a stress or strain failure condition is achieved using cohesive elements, this model is also able to predict failure propagation and stress-strain response of the hybrid composites.

Both, micro-level and ply-level models have shown accurate results in the prediction of the composites behaviour and the failure analysis [27],[28],[60],[70],[96],[97]. Micro-level models are an excellent tool to model intrayarn (fibre-by-fibre) hybrid composites since they can consider how fibres are distributed, the differences in diameters and the interaction between them. However, these models are 3D models, with higher consumption of machine resources and require that the fibre and matrix properties been characterised in detail [98]–[102]. On the other hand, ply-level models have shown their potential to model interlayer (layer-by-layer) hybrid composites, allowing to simplify the model to 2D and the properties are directly characterised from the laminate [103]–[106]. Since this thesis has the objective to understand the ply interactions and the overall failure behaviour, ply-level models will be implemented.

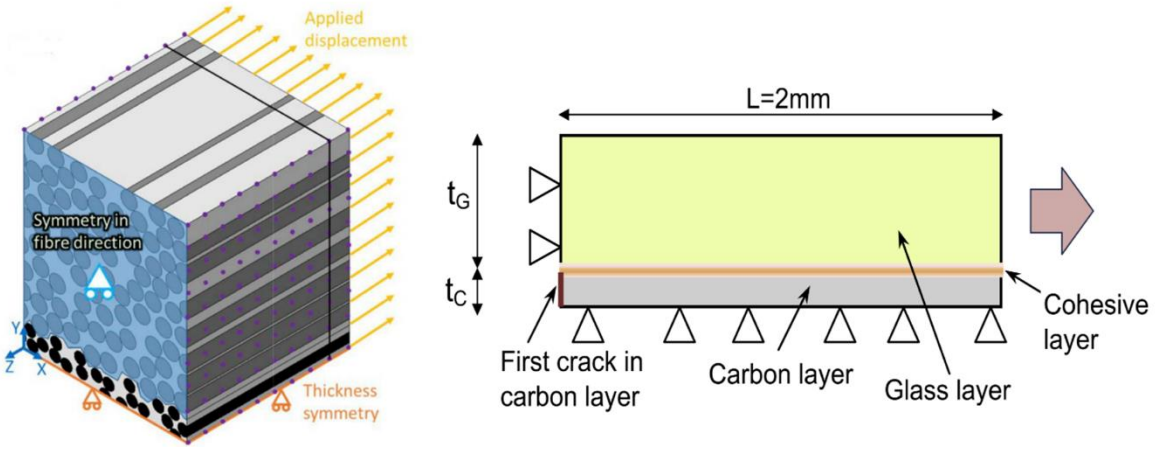

Figure 30 a) Micro-level model of hybrid glass/carbon composite under tension, b) Ply-level model of hybrid glass/carbon composite under tension, adapted from [95] and [77] respectively.

Most of the ply-level models use cohesive elements to predict failure initiation, propagation of damage and final failure of the material. The three fracture modes are captured by the cohesive elements to model traction-separation and shear conditions, see Figure 31. Cohesive elements have been used in the analysis of composite materials with gradual failure, modelling fragmentation and local delamination. According to Figure 32, if the cohesive elements are intralaminar they capture mainly mode I which produces fragmentation and if the cohesive elements are interlaminar the predominant mode is mode II which produces delamination. However, the cohesive elements also capture mixed-modes which are a common situation in composites subjected to multiple loading orientations or when the stacking sequence produces couplings in the load-deformation condition [107],[108].

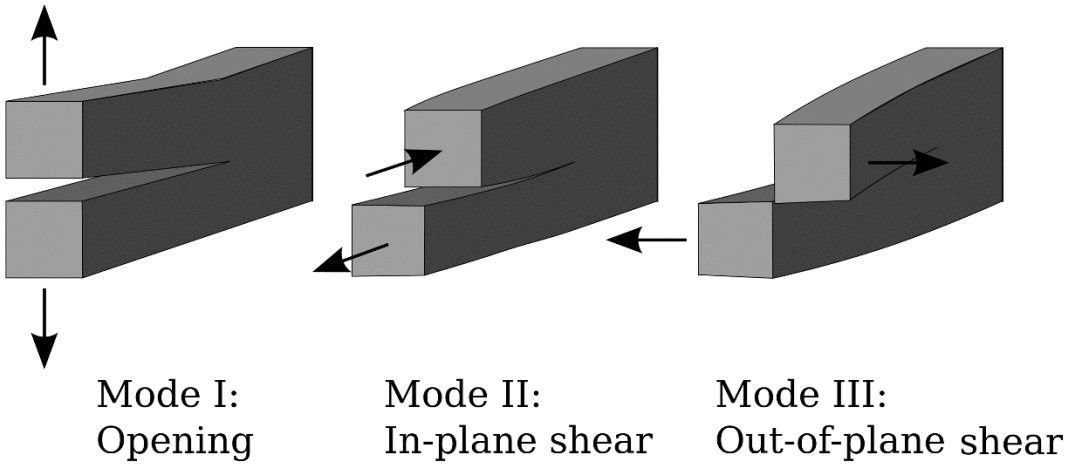

Figure 31 The three fracture modes.

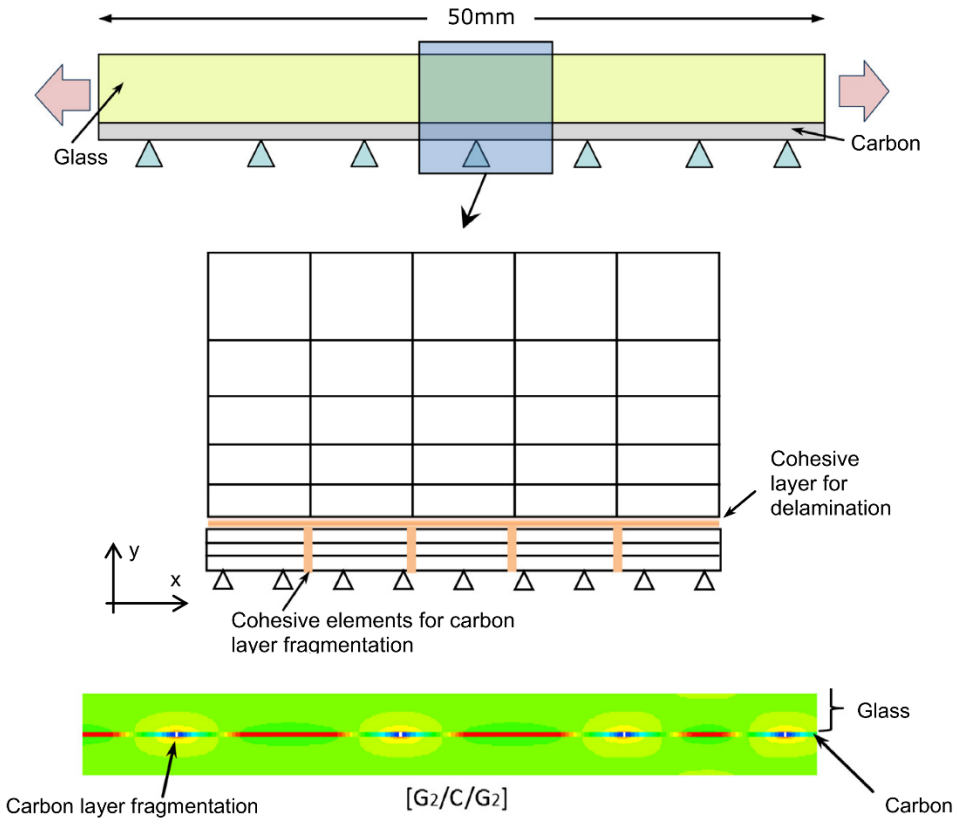

Figure 32 Modelling fragmentation and local delamination of the hybrid laminates, adapted from [77].

Cohesive elements work as a joining material with a negligible thickness which connects two plies (surfaces). According to Turon et.al. [109] the effective elastic properties of the composite depend on both the cohesive elements and the bulk material. Although cohesive elements contribute to the global deformation, its only purpose is to simulate fracture. Therefore, the elastic properties of the cohesive elements should be defined in such a way to avoid modifying the effective Young's modulus E_{eff} of the laminate. This condition is defined by Eq. (6), where the effective Young's modulus is a function of the modulus of the material, the stiffness (K) of the cohesive layer and the thickness (t) of surrounding plies.

$$E_{eff} = E_m \left(\frac{1}{1 + \frac{E_m}{tK}} \right) \qquad \text{Eq. (6)}$$

According to Eq. (6), the effective elastic properties of the composite will not be affected by the cohesive layer whenever the inequality $E_m \ll tK$ is being accomplished, i.e:

$$K = \frac{\alpha E_m}{t} \qquad \text{Eq. (7)}$$

Where α is a parameter much larger than 1 (α≫1). According to [109] for values of α greater than 50, the loss of stiffness due to the presence of the cohesive layer is less than 2%, which is an adequate value.

The constitutive response of cohesive elements is based on traction versus separation behaviour, as it is shown in Figure 33. The area under the stress-separation curve is the amount of energy associated with the failure mode G in one specific mode of load, see Figure 31. The approach combines the three fracture modes identifying three main conditions: damage initiation, damage evolution and completely damaged state. The initial response of the cohesive element is assumed to be linear, however, once a damage initiation criterion is met, material damage can occur according to a damage evolution law.

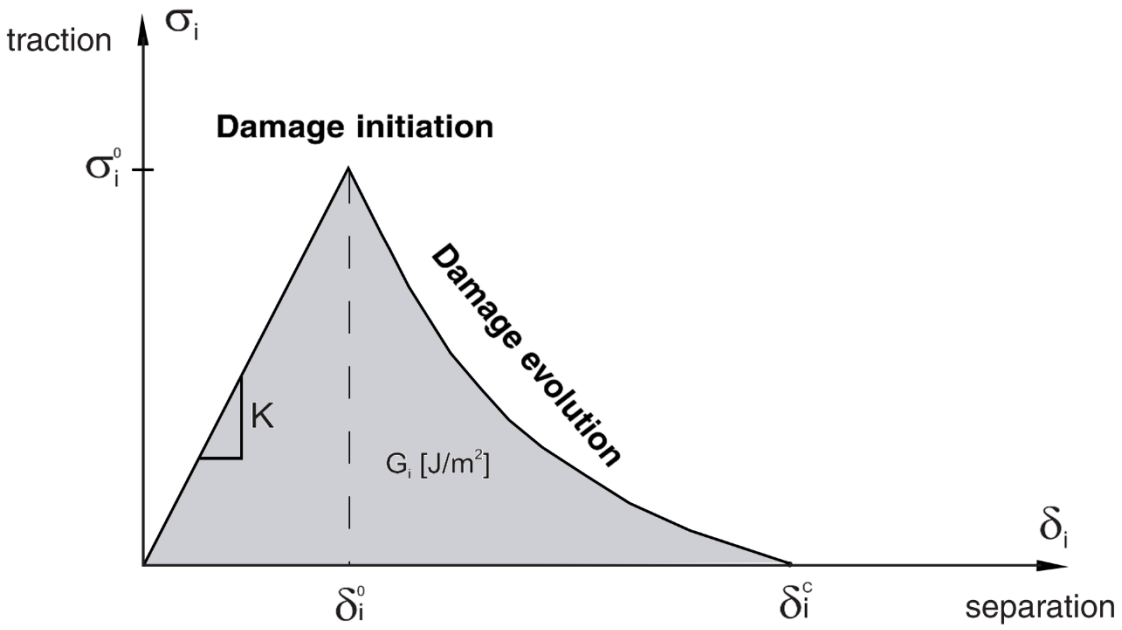

Figure 33 Typical traction-separation response, adapted from [107].

Several damage initiation criteria are available and some of them are described in Table 2, where σ_i^o and ε_i^o correspond to the strength and the failure strain of the cohesive layer, being the subindexes *n,s,t* associated with normal (mode I), shear (mode II), and shear transverse (mode III) load conditions and σ_i and ε_i correspond to an applied stress or strain at a specific load step. A value of 1 or higher indicates that the criterion has been met and damage initiation is reached.

.

Table 2 Damage initiation criteria, adapted from [107].

CRITERION	EQUATION	
Maximum nominal stress criterion	$\max\left\{\frac{\sigma_n}{\sigma_n^o}, \frac{\sigma_s}{\sigma_s^o}, \frac{\sigma_t}{\sigma_t^o}\right\} = 1$	Eq. (8)
Maximum nominal strain criterion	$\max\left\{\frac{\varepsilon_n}{\varepsilon_n^o}, \frac{\varepsilon_s}{\varepsilon_s^o}, \frac{\varepsilon_t}{\varepsilon_t^o}\right\} = 1$	Eq. (9)
Quadratic nominal stress criterion	$\left\{\frac{\sigma_n}{\sigma_n^o}\right\}^2 + \left\{\frac{\sigma_s}{\sigma_s^o}\right\}^2 + \left\{\frac{\sigma_t}{\sigma_t^o}\right\}^2 = 1$	Eq. (10)
Quadratic nominal strain criterion	$\left\{\frac{\varepsilon_n}{\varepsilon_n^o}\right\}^2 + \left\{\frac{\varepsilon_s}{\varepsilon_s^o}\right\}^2 + \left\{\frac{\varepsilon_t}{\varepsilon_t^o}\right\}^2 = 1$	Eq. (11)

On the other hand, the damage evolution law describes the rate at which the material stiffness is degraded once the corresponding initiation criterion is reached. A scalar damage variable, *D*, represents the overall damage in the material and captures the combined effects of all the active mechanisms. It initially has a value of 0 but monotonically evolves from 0 to 1 upon further loading after the initiation of damage, as it is described below.

- $D = 0$ up to damage onset while the cohesive layer is undamaged, thus retaining its initial stiffness.
- $0 < D < 1$ during degradation of the cohesive layer, when the material is gradually losing its stiffness.
- $D = 1$ at fracture when there is no remaining stiffness for the cohesive layer, which means no stress transfer capacity is provided by the interface.

The damage evolution law can be defined based on an effective displacement or based on energy and it could be linear or exponential. Each evolution law has its specific set of equations which describes the degradation of the cohesive element, due to the big number of equations the author invites the reader to refer to [107].

2.12 Opportunities for Research

The literature review provided a brief description of all the concepts used in this thesis identifying three main opportunities:

- Most of the works conducted to understand and demonstrate gradual failure in hybrid composites have been focused on unidirectional hybrid composites under tension, leaving behind other loading conditions such as multidirectional and bending loading.
- Previous studies have demonstrated gradual failure in multidirectional composites suppressing unfavourable failure mechanisms such as free-edge delamination. They show enormous potential in industrial applications. However, more experimental and analytical analysis is required to understand ply interactions and why the hybrid effect varies just changing the direction of the load applied or which is equivalent, the stacking sequence.
- To the best of the author's knowledge, gradual failure in hybrid composite material reinforced with high-performance fibres has not been demonstrated yet, and the current results in the literature are focused to achieve gradual failure of individual layers located in compression or tension rather than obtain an overall gradual failure of the composite.

CHAPTER 3 OBJECTIVES

3.1 General objective

To understand the main characteristics of gradual failure in high-performance hybrid composites under tension and bending conditions

3.2 Specific objectives

- To propose composite hybrids FRPs configurations which achieve gradual failure in tension and bending tests.
- To identify the main parameters controlling and affecting the failure process involved in the gradual failure.
- To develop numerical models to understand the failure sequence and the effect of the ply interactions in the configurations proposed.

CHAPTER 4 QUASI-ISOTROPIC COMPOSITES TENSILE BEHAVIOUR

4.1 Introduction

In this chapter gradual failure in multidirectional composites is examined. Two quasi-isotropic configurations are proposed and the stacking sequence is varied. In section 2.7, it was established that for unidirectional carbon/glass composites under tension, the hybrid effect depends directly on absolute and relative carbon thickness and material properties. In this chapter, new experimental results are presented to show that for multidirectional composites the stacking sequence and the stiffness of the adjacent layers to the 0° carbon plies has a significant impact on the knee strain and therefore the hybrid effect. To understand these results, a numerical model is proposed to study the interaction between the carbon layers, considering a single crack in one of the 0° carbon plies. The non-uniform strain distribution through the thickness produced by the crack is affected by the position and stiffness of the adjacent layers. The strain increment in the undamaged 0° carbon ply is measured. The layups where the stiffness of adjacent layers is lower, an effective strain concentration in the undamaged 0° carbon ply is observed making that the two 0° carbon plies behave like a thicker single-ply fragmenting simultaneously and leading to a lower hybrid effect.

4.2 Materials and Configuration Design

4.2.1 Materials

The materials considered for the experiments are UD S-glass/epoxy prepreg supplied by Hexcel and thin-ply UD SkyFlex USN020A carbon/epoxy prepreg from SK Chemicals. TC35 carbon fibres and aerospace-grade K50 epoxy resin are used in the carbon/epoxy plies. S-Glass/epoxy is a standard thickness prepreg using FliteStrand S ZT S-glass fibres and aerospace-grade epoxy resin system 913. Although no chemical analysis on the compatibility of both resin systems is done, previous experience indicated a good bonding between both resin systems [110] at a curing temperature of 125°C. The most relevant properties of prepreg systems can be found in Table 3. To quantify the hybrid effect in the next sections, the fibre failure strain (1.6%) is implemented. Despite the literature reports the failure strain for the TC35/K50Epoxy prepreg (1.9%) [110], it was calculated using the hybrid configuration [S-Glass/$Carbon_2$/S-Glass] where 2 carbon plies are used. This value has already a hybrid effect since the thickness of the carbon sub-laminate is thin enough to have an enhancement in the strain, see Figure 12b, therefore it is more adequate to use 1.6% as the baseline.

Table 3. Properties of the applied UD prepregs.

Prepreg Material	Elastic Modulus [GPa]	Fibre Failure Strain [%]	Prepreg Failure Strain [%]	Volume Fraction [%]	Cured ply thickness [mm]	Fibre mass [g/m^2]
TC35/K50Epoxy	114.3[a]	1.60[a]	1.90[b]	46.9[a]	0.027[a]	22[a]
S-Glass/913Epoxy	45.7[c]	5.5[a]	3.98[c]	50[a]	0.155[c]	190[a]

[a] Based on the manufacturer´s datasheet.
[b] First carbon layer fracture measured on [S-Glass/Carbon2/S-Glass] UD interlayer hybrid in static tension [110]
[c] Taken from [111]

4.2.2 Design of QI Hybrid Laminate

To understand the interaction between the layers and the effect of the stiffness of the adjacent sub-laminates, two types of quasi-isotropic (QI) configurations are proposed. QI composites are conceived to create a lamina which behaves like an isotropic plate [11], to such an end, the plies have an orientation given by $\theta_k = k\pi/N$ where k is the ply number and N is the number of plies which should be minimum of three plies. For this work, N takes the values of 3 and 4, given the next basic angles for each QI configuration: [60/-60/0] and [45/90/-45/0]. It is worth to mention, that the plies can be oriented in any order and the composite is still quasi-isotropic.

For the hybrid QI composites, the orientation-dispersed method presented in section 2.9 is used. This stacking sequence approach is based on combining different non-hybrid QI sub-laminates in a single composite, i.e, [QI S-glass/ QI Carbon / QI S-glass]. As mentioned before, in comparison with other stacking sequence approaches, it has been demonstrated that the orientation-dispersed method reduces significantly the free-edge delamination in the plies interface [75]. According to that, two reference configurations are presented:

±45QI: $[45°_{\text{S-Glass}}/90°_{\text{S-Glass}}/-45°_{\text{S-Glass}}/0°_{\text{S-Glass}}/0°_{\text{TC35}}/45°_{\text{TC35}}/90°_{\text{TC35}}/-45°_{\text{TC35}}]_s$

±60QI: $[60°_{\text{S-Glass}}/-60°_{\text{S-Glass}}/0°_{\text{S-Glass}}/0°_{\text{TC35}}/60°_{\text{TC35}}/-60°_{\text{TC35}}]_s$

Using the analytical method proposed by Jalalvand et. al. [9] (section 2.7 and 2.8) the failure modes of the two QI configurations are predicted. Figure 34 shows the damage mode map of the QI configurations proposed. The map correlates the geometric parameters with the possible failure scenarios separated by boundaries: catastrophic delamination, premature failure, fragmentation and fragmentation followed by local delamination. The horizontal axis in the map corresponds to the relative TC-35 carbon ply thickness (the thickness of QI carbon sub-laminate divided by the total hybrid's thickness) and the vertical axis shows the absolute thickness of the TC-35 QI carbon sub-laminate. To generate the map the QI glass and QI carbon sub-laminates properties are homogenised, the equivalent stiffness is calculated using Classical Laminate Theory and it is assumed that the cracks propagate

through the thickness of the whole carbon sub-laminate. The failure strain of the homogenised QI carbon sub-laminate is assumed to be equal to the 0° carbon layer failure strain. The damage analysis was carried out using a mode II critical strain energy release rate of G_{IIC}= 1 N/mm. This value is selected based on [112], where similar hybrid configurations made out of the same prepreg systems are evaluated. Table 4 summarises properties used for the damage analysis.

According to Figure 34 the proposed QI hybrid layups are in the Fragmentation and local Delamination (Frag. & Delamination) region which is the desired damage scenario, avoiding catastrophic damage modes such as premature failure and catastrophic delamination. The layup ±45QI is close to the boundary with catastrophic delamination, which could generate larger local delaminations in this configuration. However, the damage mode map is just an approximation of the damage modes since the analytical model is originally conceived for UD laminates. For UD composites all the carbon layers are located at 0° and fragmentation takes place through all thickness of the carbon sub-laminate, but in QI, some layers are off-axis and fragmentation only is produced on the 0° carbon plies. To adapt the method developed by Jalalvand et. al. [9] to QI laminates, the thickness of the fragmented carbon plies is overestimated since the fragmentation is assumed to take place throughout all the thickness of the carbon sub-laminated including the off-axis plies. This increases the relative and the absolute carbon thickness, and therefore, the damage mode map is conservative. According to that, both layups show acceptable behaviour and they are expected to produce gradual failure in tension.

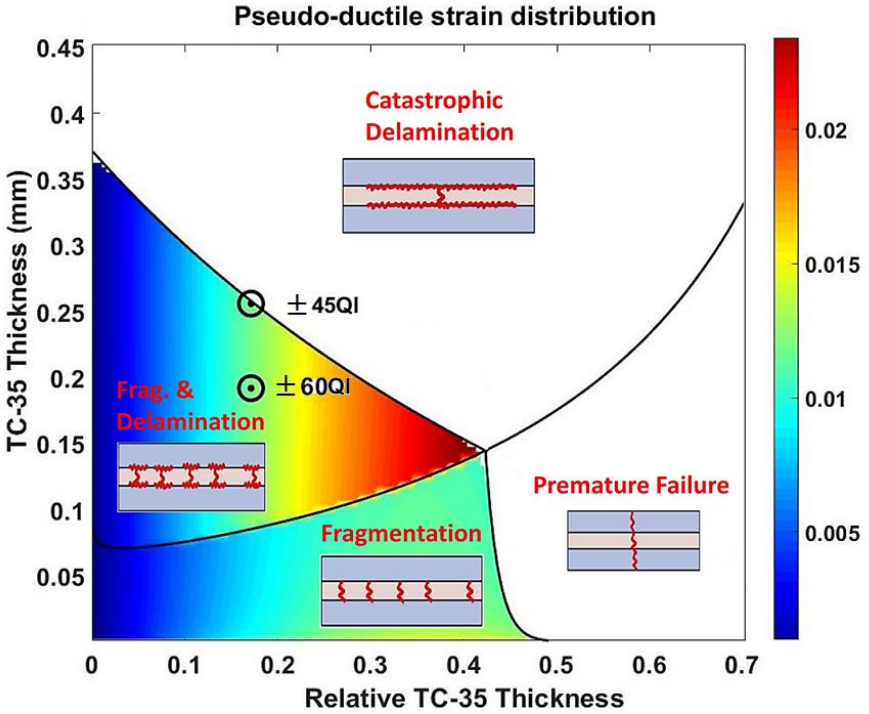

Figure 34 Damage mode map of the QI hybrid configurations ±45QI, and ±60QI.

Table 4. Material properties used in producing the damage mode map

Prepreg type	S-Glass/913Epoxy	TC35/K50Epoxy
E1 (GPa) [a]	45.7	114.3
E2 (GPa) [b]	15.4	6
G12 (GPa) [b]	4.3	2.4
V12 [b]	0.3	0.3
Homogenised in-plane stiffness (GPa) [c]	19.7	42.0
Failure strain (%) [d]	5.5	1.6

[a] Elastic Modulus Table 3.

[b] Based on the manufacturer's datasheet.

[c] Calculated using Classical Laminate Theory.

[d] Fibre failure strain, Table 3.

Using the QI reference configurations, six layups are proposed variating the plies position. Figure 35 shows the layups to be analysed in the next sections: ±45QI_1 and ±60QI_1 are the reference configurations. In layups ±45QI_2, and ±60QI_2 the 0° glass layer was relocated from the position close to the 0° carbon ply to the external faces. For ±45QI_3 and ±60QI_3 the position of the plies was changed. In the case of layup ±45QI_3, the two 0° carbon layers are one position closer. While in layup ±60QI_3, 0° carbon plies are next to each other. In each configuration, only the positions of the plies are rearranged, keeping constant thickness, material and number of layers.

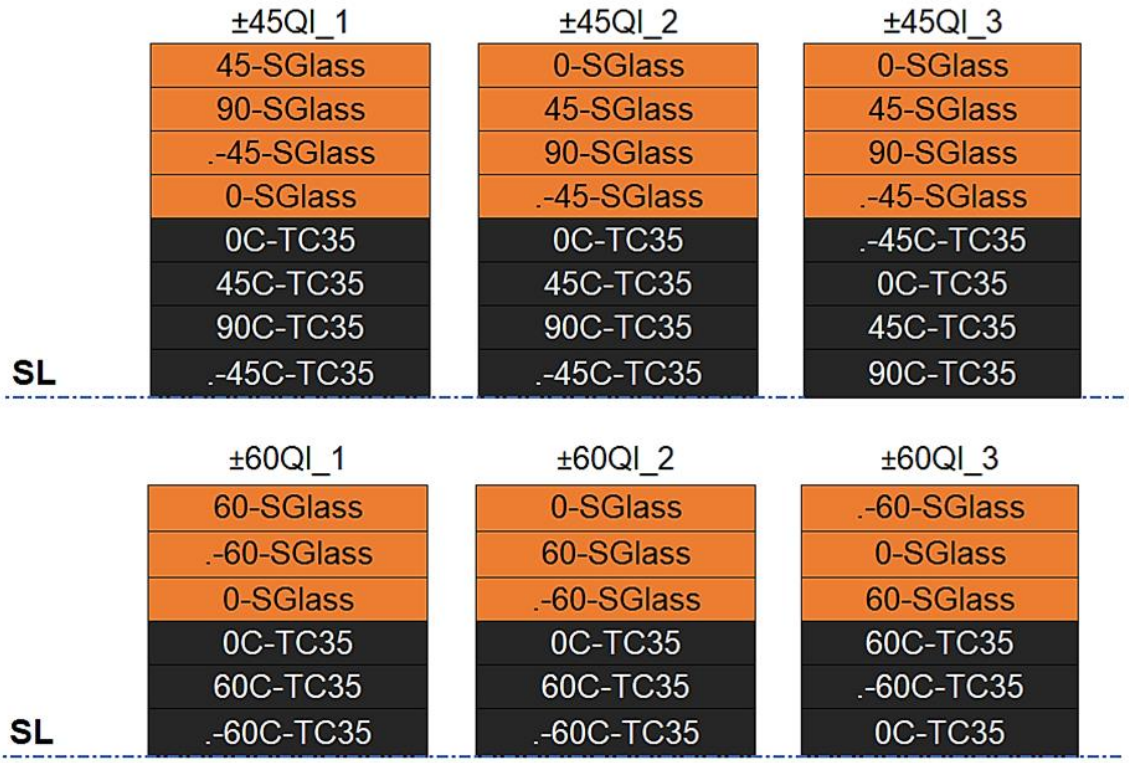

Figure 35 QI layups proposed to understand the interaction between the layers (SL: Symmetric Line).

4.3 Experiments
4.3.1 Specimen Manufacture

The layups were laid upon a flat aluminium tooling plate and vacuum bagged, as shown in Figure 36. Following the recommendation of experts from the University of Bristol, the consolidation was conducted using an autoclave implementing a two-step cure cycle. First, the temperature was ramped up to 80°C and held there for 60 minutes and then the laminates were heated-up reaching the final cure temperature of 125°C and held for 100 minutes. This cure cycle was implemented in [75] and [80] showing good results. Once the laminates are cured, end tabs made of 2 mm thick woven glass/epoxy were bonded using a two-component Araldite 2000 A/B epoxy adhesive. The individual specimens were cut with a diamond cutting wheel. The dimensions of the samples were then measured as shown in Table 5. Two white tracking dots were painted on the specimen face of each sample. The dots are used for video gauge recording, as it is explained in the next section. A gauge length of 150mm and 125mm for the external and internal white dots were used respectively.

Figure 36 Manufacturing process using an autoclave.

Table 5. Average geometric dimensions

Spec. type	Width (mm)	Thickness (mm)	Free length (mm)
±45Ql_1	19.98±0.08	1.58±0.00	163±0.34
±45Ql_2	19.93±0.07	1.59±0.00	164±0.19
±45Ql_3	19.89±0.09	1.59±0.00	162±0.58
±60Ql_1	19.95±0.06	1.20±0.00	165±0.50
±60Ql_2	19.84±0.15	1.21±0.00	160±1.40
±60Ql_3	19.78±0.21	1.21±0.01	162±0.55

4.3.2 Test Method

The specimens were tested under uniaxial tensile loading with a displacement control crosshead speed of 2 mm/min on a computer-controlled Instron 8801 type 100 kN rated universal hydraulic test machine with a regularly calibrated 25 kN load cell and wedge type hydraulic grips. Strains were measured using an Imetrum video gauge system, tracking the points on the specimen face, see Figure 37. At least 5 specimens of each layup were tested to check the repeatability of the results. Some of the tests were interrupted at a strain value slightly higher than the knee point in order to analyse the failure mechanisms.

Figure 37 Fixture and mounting arrangement for the uniaxial tensile tests.

4.4 Test Results

Results obtained from the tensile tests for the investigated configurations show the desired gradual failure response characterised by fragmentation and local delamination, see Figure 39 and Figure 40. Despite ±45QI configuration is located close to the boundary of catastrophic delamination in the damage mode map (Figure 34), no evidence of large delamination is observed in different specimens, neither load-drops are observed in the

strain-stress curves. This proves that the design and manufacture of the layups were appropriate.

All the layups show a stiffness reduction, which is common in multidirectional composites where matrix cracks are generated at a lower applied strain in the off-axis plies. The matrix cracks reduce the load capacity of the off-axis plies, showing an overall stiffness reduction of the laminates. The average stiffness reduction was calculated as the difference between the initial Young's modulus E1 and Young´s modulus E2 of a secant line from the origin of the curve to a point close to the knee point, as shown schematically in Figure 38. The averaged knee strain ε_y and knee stress σ_y were also calculated using two trendlines just before and after the knee point, calculating the intersection point, see Figure 38. The average measurements are summarised in Table 6 for each layup, including the percentage of stiffness reduction.

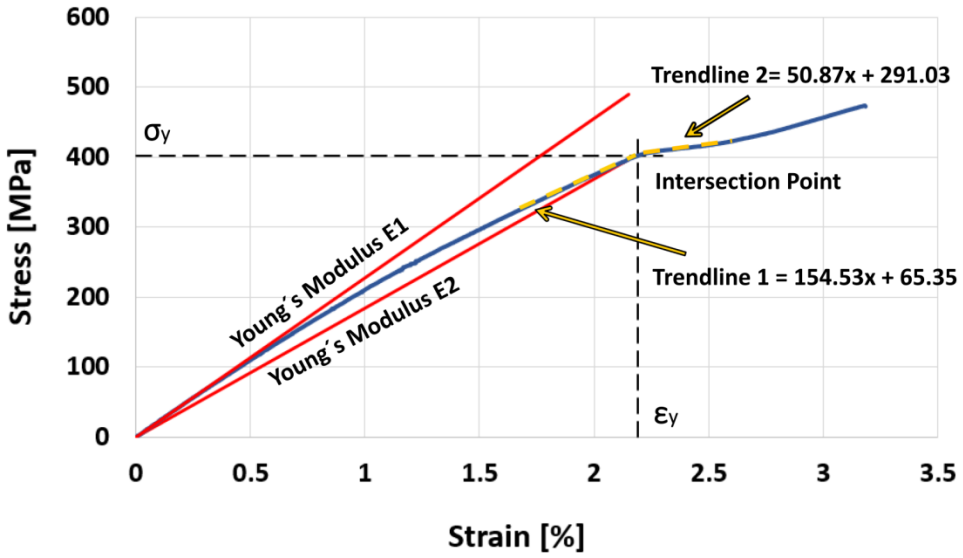

Figure 38 Graphic definitions of the knee point parameters.

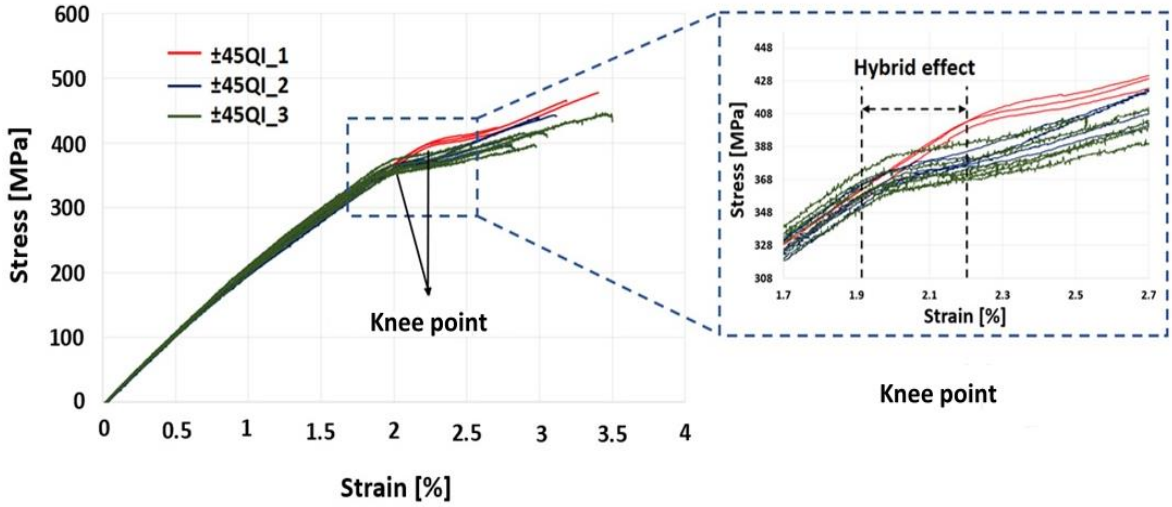

Figure 39 Results of the tensile tests for the ±45QI specimens.

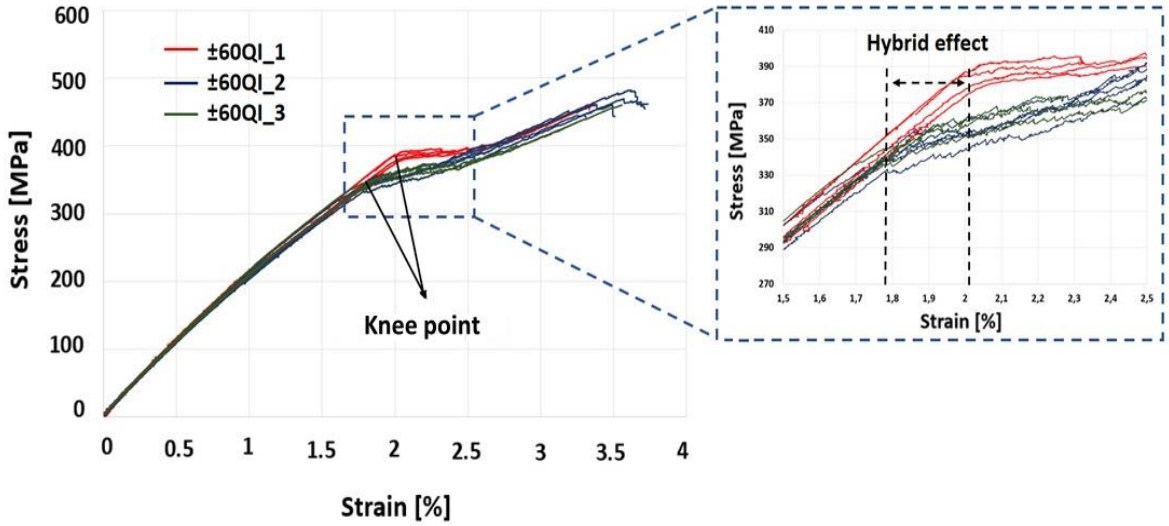

Figure 40 Results of the tensile tests for the ±60QI specimens.

Table 6. Experimental results for the investigated hybrid specimens at the knee point.

Specimen type	Knee strain ε_y [%]	Knee stress σ_y [MPa]	Young's modulus E1 [GPa]	Young's modulus E2 [GPa]	Stiffness reduction [%]
±45QI_1	2.19±0.02	402.8±4.6	22.7±0.2	18.3±0.1	19.2
±45QI_2	1.95±0.02	365.9±4.2	23.3±0.7	18.8±0.4	19.5
±45QI_3	1.91±0.03	363.7±8.8	23.3±0.7	18.9±0.3	18.9
±60QI_1	2.01±0.02	384.8±5.0	24.8±1.1	19.2±0.5	19.2
±60QI_2	1.81±0.03	342.9±7.4	22.7±0.2	19.2±0.6	15.7
±60QI_3	1.75±0.04	336.7±1.8	23.7±1.1	19.4±1.6	18.2

Figure 41 shows the different knee strain values for the layups. According to the results, all layups show a knee strain higher than the fibre failure strain reported by the manufacturer's datasheet (1.6%, see section 4.2.1), indicating a hybrid effect. It is possible to see that there is a different response between layups were just stacking sequence was varied. The highest knee strains are reported by the layups ±45QI_1 and ±60QI_1. Comparing these layups with the knee strains of layups ±45QI_2 and ±60QI_2 where just the 0° glass ply was relocated from the position close to the 0° carbon ply to the external face, a reduction in the knee strain observed. The lowest value of knee strain is present in layup ±60QI_3 where 0° carbon plies are close to each other.

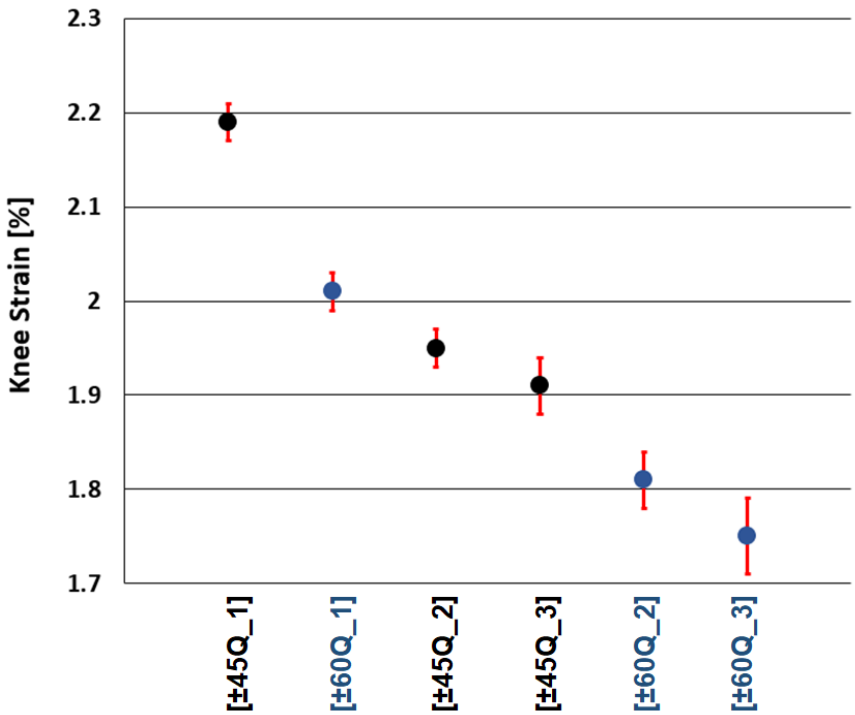

Figure 41 Knee strain of different layups including carbon baseline.

4.5 Microscope Observations

Samples of each layup were interrupted after knee point at around 2.3% of strain and observed using a Nikon Eclipse LV100 optical microscope to study the failure mechanisms. The samples were ground 5mm along the width using 240 grit sandpaper and water as the lubricant. Then, the samples were progressively polished up-to a 2000 grit SiC sandpaper. The final polishing was a chemo-mechanical step in a cloth with a 0.05 µm colloidal silica suspension.

Figure 42 shows the images through the full thickness of the layups. In general, matrix cracking in off-axis plies is observed, which is responsible for stiffness reduction in the strain-stress curves. Despite the stiffness reduction calculated in Table 6 is similar for all layups, matrix cracking is more evident in layups ±45QI_3 and ±60QI_3 as well as local delamination. The voids observed in the figures are produced by the colloidal silica in the grinding process and they don't correspond to defects of the manufacturing.

Some regions were analysed in more detail in Figure 43, where fragmentation in the 0° carbon plies is observed in all layups (red arrows). Figure 43 shows only the whole carbon sub-laminate and the adjacent glass ply, which corresponds to 0° glass in ±45QI_1 and ±60QI_1 and an off-axis ply in the other layups (45° glass or 60° glass). Layups ±45QI_1 and ±60QI_1, where 0° glass ply is close to the 0° carbon ply, the failure is locally contained showing minor matrix cracking and delamination around the fracture. For layup ±45QI_2 and ±60QI_2, where the adjacent glass ply is an off-axis ply, the fracture produced in 0° carbon plies propagates through the thickness. On the other hand, layup ±45QI_3 where carbon plies are closer in comparison with ±45QI_2, matrix cracking is more severe and delamination is more extensive. Finally, for layup ±60QI_3, the two 0° carbon plies behave as a single layer, showing a single crack which propagates to the adjacent layers.

From Figure 42 and Figure 43 it is possible to see that the main failure mechanisms are fragmentation, local delamination and matrix cracking in off-axis plies. It was observed that for each crack generated in the top 0° carbon ply, there is another crack in the bottom 0° carbon ply. This condition shows that the two 0° carbon layers interact with each other. If a crack is produced in the top 0° carbon ply the strain/stress concentrations produced by the crack increase the probability of failure of the bottom 0° carbon ply.

These results provide evidence of the interaction between the two 0° carbon plies but it is not enough to explain the differences in the hybrid response of the layups and further analysis is required. According to that, in the next section, these interactions between the 0° carbon plies will be studied using numerical modelling, showing correlations between the layups, the strain distribution and the experimental results.

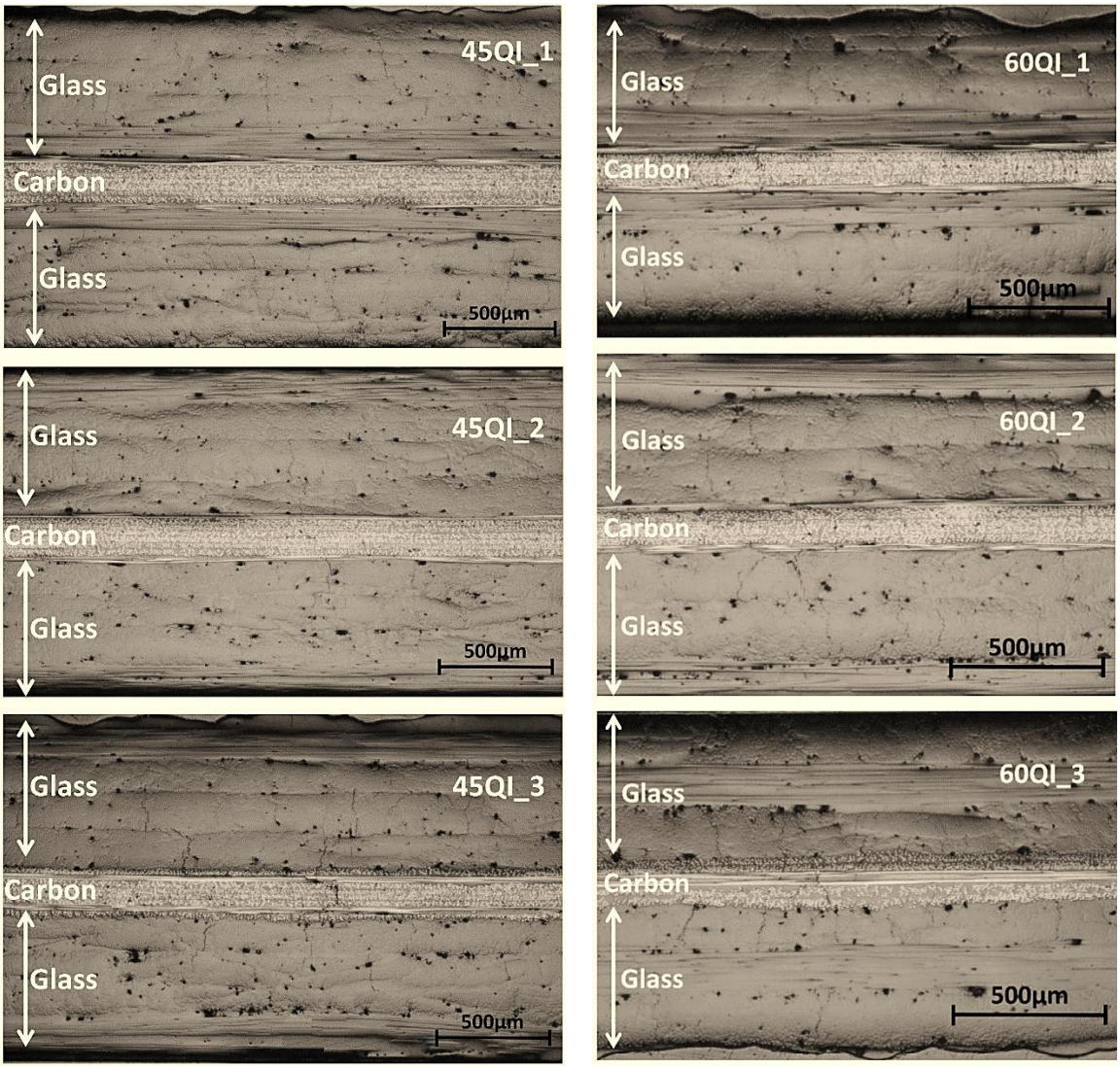

a) **b)**

Figure 42 Microscopy images of the interrupted samples, overall images covering the full thickness of all the layups. a) ±45QI layups b) ±60QI layups.

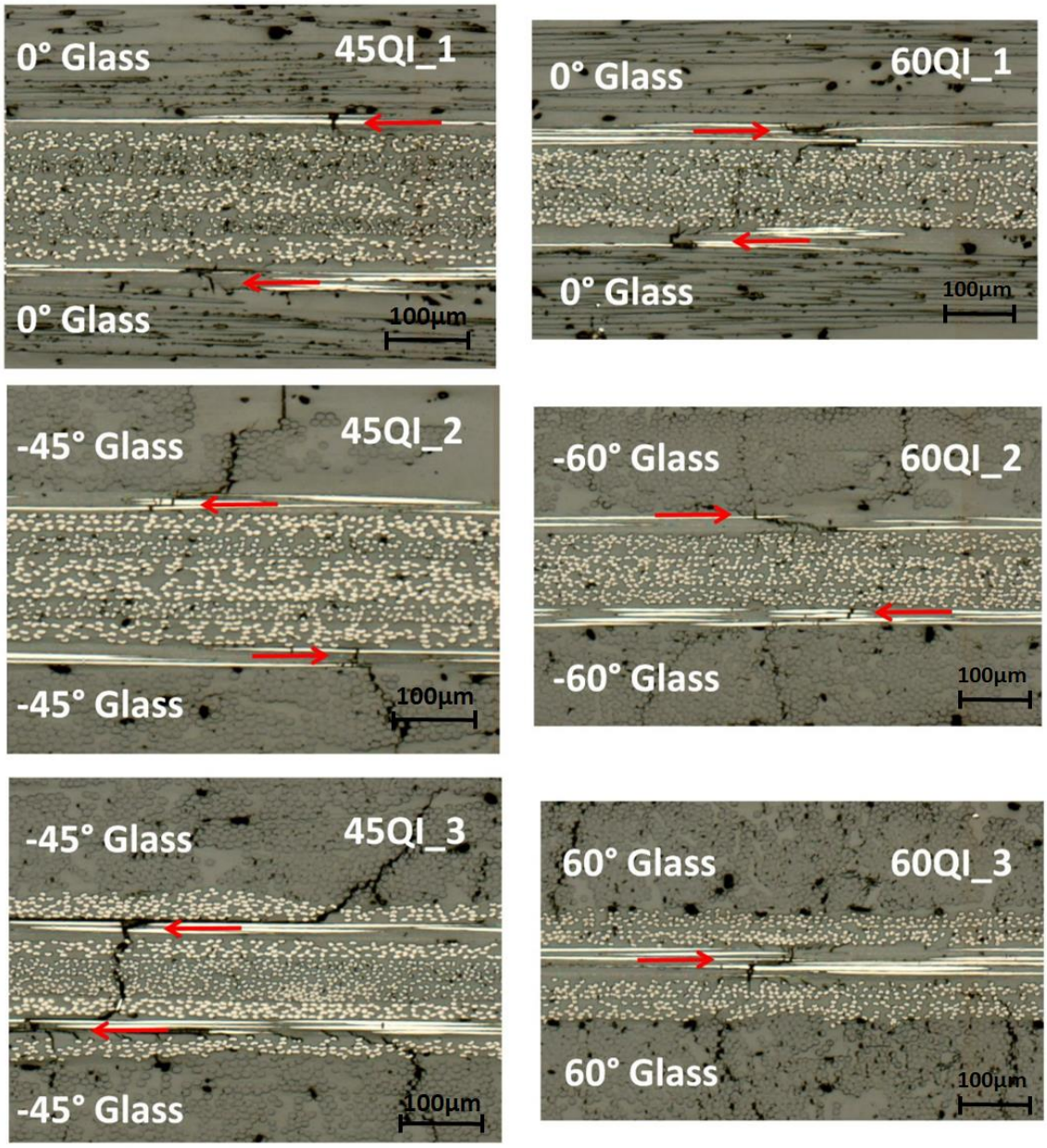

a) **b)**

Figure 43 Microscopy images of the interrupted samples, detail images covering the full thickness of carbon sub-laminated and the closest glass ply. a) ±45QI layups b) ±60QI layups.

4.6 Numerical Modelling

To understand the interaction between the two 0° carbon layers and its effect in the hybrid response, a numerical model is proposed in this section. The analysis is based on the next hypothesis:

A local fragmentation in the top 0° carbon ply induces a strain increment on the bottom 0° carbon ply. If this strain increment is enough to reach failure strain, a fracture will be

generated in the bottom 0° carbon ply. This will make that fragmentation in both 0° carbon plies happen at the same time, behaving like a single thicker layer rather than two single layers failing individually and reducing the hybrid effect. This strain increment depends on the position of the 0° carbon layers in the layup and the stiffness of the adjacent layers, see Figure 44.

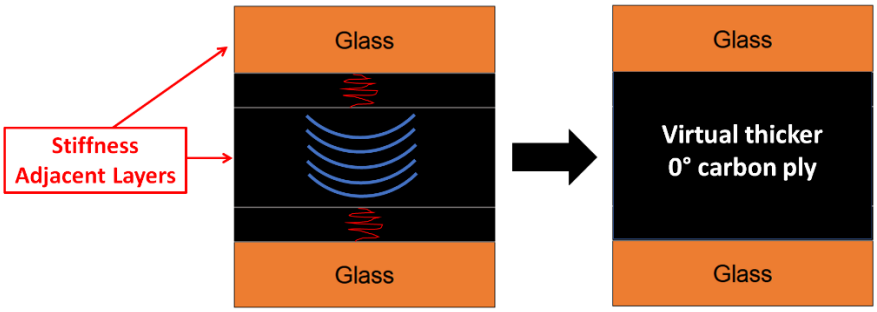

Figure 44 Interaction between 0° carbon plies and virtual thicker layer.

The numerical model proposed consists of a unit of 10 mm of a section along with the laminate and evaluates the strain distribution through the thickness, considering a single crack in one of the 0° carbon layers. The model studies the induced strain increment on the undamaged 0° carbon layer and the effect of the position and stiffness of the adjacent sub-laminates. The model is developed in Abaqus and it corresponds to a 2-D finite element model with 8-node quadratic plane strain elements with linear elastic material properties and non-elastic cohesive elements. The model has 13.080 elements and 44.336 nodes. A damping viscosity of $1x10^{-5}$ was assigned to the cohesive elements to improve convergence. In total 27 iterations were needed and the running time was 3 minutes. The crack in the top 0° carbon ply (damaged 0° carbon) is modelled as a discontinuity in the boundary condition U1=0 at the left side of the model (see Figure 45). Between the 0° carbon plies, cohesive elements are used to model potential local delamination and interfacial damage. The maximum displacement of 0.16mm is applied, which is equivalent to the fibre failure strain 1.6%. Figure 45 shows a schematic of the numerical model.

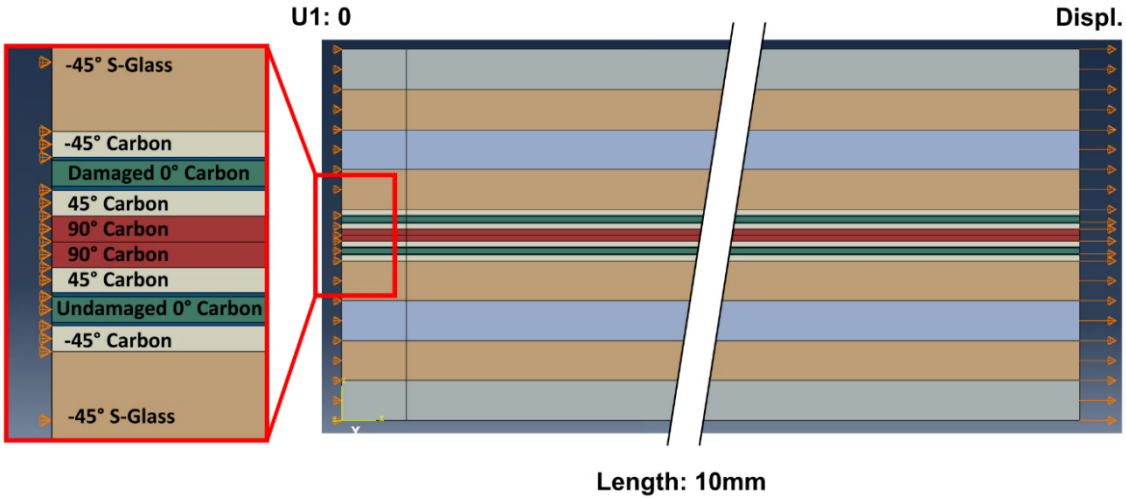

Figure 45. Applied numerical model using ABAQUS, layup ±45Ql_3.

The material properties correspond to the carbon and glass prepregs and they are summarised in Table 7. G23 is calculated using Eq. (12) and the other properties are taken from the manufacturer datasheet and Table 3.

$$G_{23} = \frac{E33}{2(1 + v_{23})} \quad \text{Eq. (12)}$$

Table 7 Material properties for the numerical model.

Properties	S-Glass/913Epoxy	TC35/K50Epoxy
E11 [MPa]	45600	114300
E22 [MPa]	15400	6060
E33 [MPa]	15400	6060
V12	0.3	0.32
V13	0.3	0.32
V23	0.45	0.45
G12 [MPa]	4340	2400
G13 [MPa]	4340	2400
G23 [MPa]	5310	2090

To calculate the properties of off-axis plies, Classical Laminate Theory is used to obtain the transformed reduced stiffness matrix $[\bar{Q}]$ and the compliance $[\bar{S}]$, see Eq. (13) and Eq. (14). Where $[T]$ is the transformation matrix and $[Q]$ is the stiffness matrix based on material properties of Table 7 and $[R]$ is Reuter's matrix (for more datils see reference [11]).

$$[\bar{Q}] = [T]^{-1}[Q][R][T] \quad \text{Eq. (13)}$$

$$[\bar{S}] = [\bar{Q}]^{-1} \quad \text{Eq. (14)}$$

Additionally, it was considered the stiffness reduction in the loading direction produced by matrix cracking, which was calculated in Table 6 for each layup. It was assumed that the stiffness reduction is only produced by matrix cracking in glass off-axis plies. This assumption is valid considering that the thickness of a carbon ply is about six times less than the thickness of a glass ply, additionally, thin carbon plies delay matrix cracking as a consequence of the tow-spreading manufacturing method (see section 2.4). Also, in order to simplify the calculation and the model, it was assumed that the stiffness reduction is the same for all glass off-axis plies, e.g. the stiffness reduction of the 90°glass ply is the same of a ±45°glass ply in the ±45QI configuration. However, in real conditions, the stiffness reduction of 90° plies is higher than 45° plies.

According to that, to calculate the stiffness reduction of the off-axis plies for each layup, Eq. (15) is used, which is based on micromechanics. Where E_{11} is the Young's modulus of the whole laminate in the loading direction, *t* is the thickness of each ply, E is Young's modulus of the plies in the loading direction, *i* corresponds to the off-axis plies (±45° and 90° for ±45QI and ±60° for ±60QI) and *x* is a reduction factor. Making *x* equal to 1, E11 correspond to the

theoretical Young's modulus of the laminate without stiffness reduction (without matrix cracking), which is 23.5 GPa and 26.3 GPa for ±45QI and ±60QI respectively. These values are similar to the values reported in Table 6 calculated from the experimental curves, which corroborates that the equation is consistent. Now considering the stiffness reduction, E_{11} is reduced proportionally to the values reported in Table 6 for each layup, e.g. for ±45QI_1 $E_{11(reduced)}$=23.5Mpa*(1-0.192)=19.0Mpa, using $E_{11(reduced)}$ for each layup, the reduction factor *x* is calculated for the off-axis plies in the layups. Finally, Young's modulus calculated using Eq. (13) and Eq. (14) for the off-axis plies is recalculated using the reduction factor. Table 8 summaries the results of the reduction factor *x* and Figure 46 show Young's modulus in the loading direction of the plies, highlighting the 0° carbon and glass plies.

$$E_{11} = \frac{t_{0°G}E_{0°G} + x(\sum t_{iG}E_{iG}) + t_{0°C}E_{0°C} + (\sum t_{iC}E_{iC})}{t_{0°G} + \sum(t_{iG}) + t_{0°C} + \sum(t_{iC})} \qquad \text{Eq. (15)}$$

Table 8 Reduction factor and the reduced E11 for off-axis plies.

Layup	±45QI_1	±45QI_2	±45QI_3	±60QI_1	±60QI_2	±60QI_3
Reduction Factor X	0.49	0.48	0.50	0.17	0.43	0.34

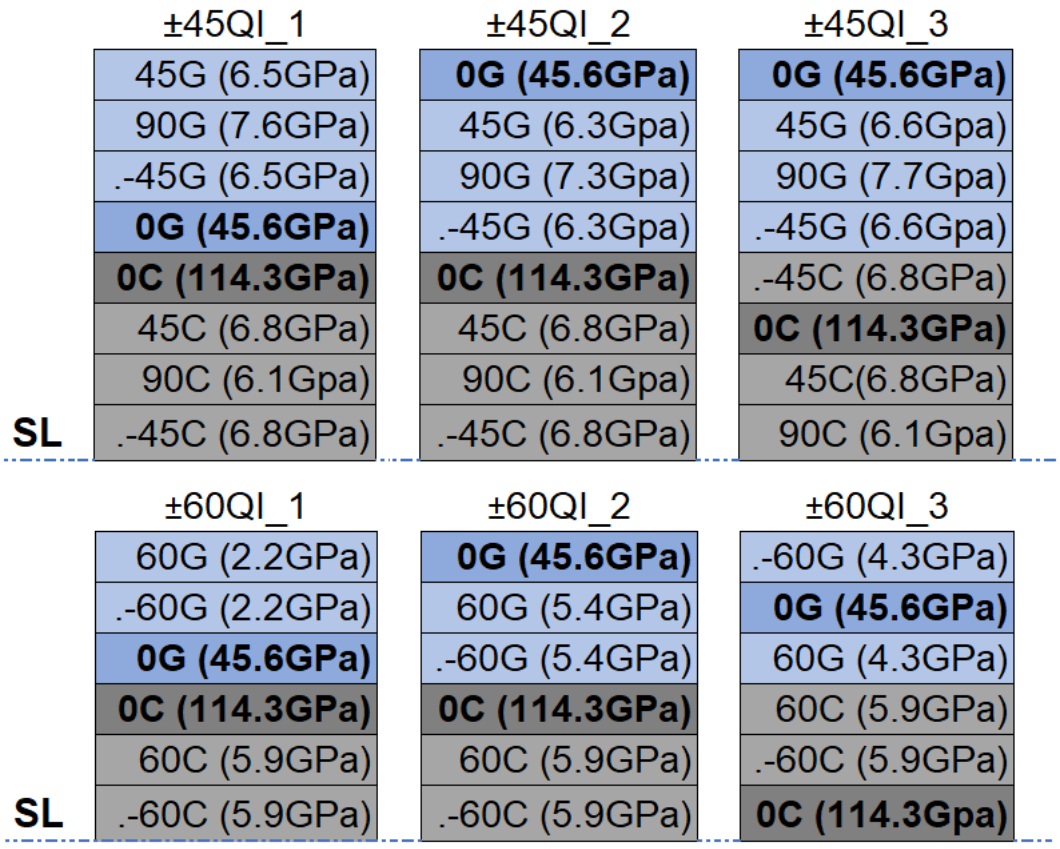

Figure 46 Young's modulus E1 in the loading direction of the plies for the layups (where C is carbon and G is glass).

Using the properties of Figure 46 the stiffness of the different laups was calculated using the numerical model in abaqus and compared with the experimental curve before the knee point. Figure 47 shows the stiffness of the layups using the reduction factors and the original stiffness without reduction, all of them calculated using the numerical model. According with the results, it is possible to conclude that the model is consistent in the linear elastic part and the stiffness calculations are in agreement preliminar results of Eq. (15) and the experimental results of Table 6.

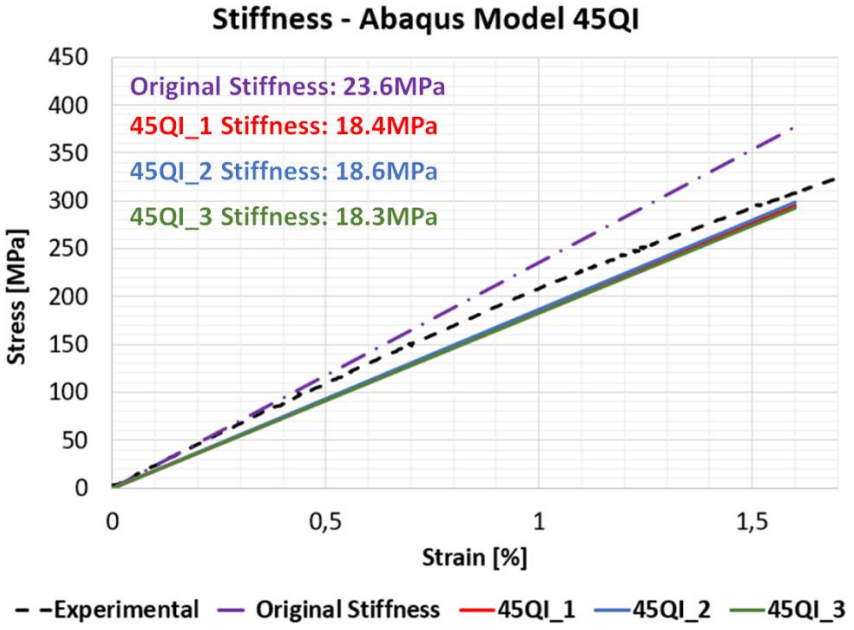

a)

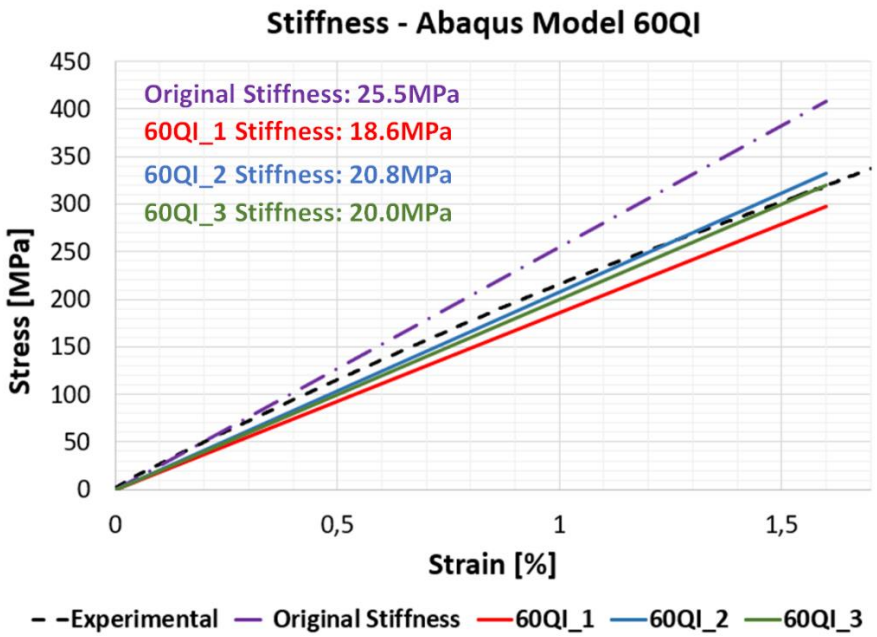

b)

Figure 47 Calculation of the stiffness of the layups using the numerical model in Abaqus. a) ±45QI layups b) ±60QI layups.

For cohesive elements, the quadratic nominal stress criterion (see Table 2) was selected to set damage initiation and the damage evolution was defined based on energy with linear softening (following recommendations on [113]). To determinate the maximum element size, the cohesive zone length is assumed equal to a variation of Hillerborg constant for orthotropic materials [103], Eq. (16):

$$l_{cz} = E_{II}^{'} \frac{G_{IIC}}{\tau^0} \quad \text{Eq. (16)}$$

Where $E_{II}^{'}$ is an equivalent elastic modulus for orthotropic materials, which is calculated using Eq. (17) and Eq. (18), G_{IIC} critical strain energy release rate in mode II of the cohesive zone and τ^0 is the shear strength of the cohesive zone (for more detail see [103]).

$$\frac{1}{E_{II}^{'}} = \sqrt{b_{11}/2} \sqrt{(b_{11}b_{33})^{1/2} + (b_{31} + b_{55}/2)} \quad \text{Eq. (17)}$$

$$b_{11} = 1/E_{11},\ b_{33} = 1/E_{33},\ b_{31} = -v_{31}/E_{33},\ b_{55} = 1/G_{31} \quad \text{Eq. (18)}$$

Using the properties of the carbon prepreg in Eq. (18), a G_{IIC}=1 (see section 4.2.2) and assuming that the shear strength of the cohesive zone is similar to the resin shear strength τ^0=67MPa, the cohesive zone length l_{cz} is 6.4mm. Following the recommendations of Turon et al. [109], a minimum of 3 cohesive elements is required to conduct an accurate delamination analysis and ensure that enough interface elements exist within the cohesive zone length at the point of crack propagation. According to that, a maximum of 2.1 mm element size is required to have an adequate simulation. Table 9 shows the properties of the cohesive elements used in the model, where the cohesive element stiffness before damage initiation K is calculated using Eq. (7).

Table 9 Properties of cohesive elements.

τ^0 [N/mm^2]	K [N/mm^3]	G_{IIC} [N/mm]	Thickness t [mm]	Element size [mm]
67	1x10^5	1	0.004	0.25

4.7 Numerical Model Results

Using the numerical model, the strain profile through the thickness of the different layups was determined at a strain of 1.6%. Figure 49 shows the results for layups ±45QI and ±60QI and the strain gradient in the loading direction (E11) obtained directly from Abaqus. Before fracture on the top 0° carbon ply, the strain is constant and equal to 1.6% through the thickness (see “Fibre failure strain 1.6%”, green dash-line in Figure 49). When a crack occurs, the cracked 0° carbon ply loses its load capacity and the strain profile becomes non-uniform, being the strain zero in the cracked top 0° carbon ply and maximum in the adjacent layers.

The percentage of strain increment produced in the undamaged bottom 0° carbon ply was calculated for each layup. The calculation was conducted measuring the maximum strain in the bottom 0° carbon ply and comparing this strain with the baseline 1.6% (see “strain increment red box” in Figure 49). Layups ±45QI_1 and ±60QI_1 show the smallest strain increment for each configuration, which means that the probability of failure of undamaged 0° carbon ply is lower compared to the other layups. Layup ±60QI_3 where the two 0° carbon plies are close to each other has the largest percentage of strain increment, so the probability of failure of the undamaged 0° carbon is quite high once a crack is produced in the top 0° carbon ply. For layups ±45QI_2 and ±60QI_2 where the 0° glass ply is moved to the surface, the strain increment in the bottom 0° carbon ply is higher in comparison with layups ±45QI_1 and ±60QI_1. This means that the stiffness of the carbon sub-laminate separating the two 0° carbon plies is important as is also the stiffness of the adjacent glass ply.

To understand better these results, the strain increment calculated with the model is compared with the experimental results. Figure 48 shows the correlation between the strain concentration in the undamaged 0° carbon ply and the knee strain taken from the experimental tests. In general, changing the stacking sequence results in the variation of the strain distribution, the specimens where the strain increment in the undamaged bottom 0° carbon ply is low a higher knee strain is observed, which means an increased hybrid effect. However, the correlation is not linear and layup ±45QI_2 shows a lower strain increment than ±60QI_1 but the knee strain is lower. This is likely because the model does not consider micro-level mechanisms such as fibre breaks and matrix cracking which in the case of ±60QI_1 are locally contained.

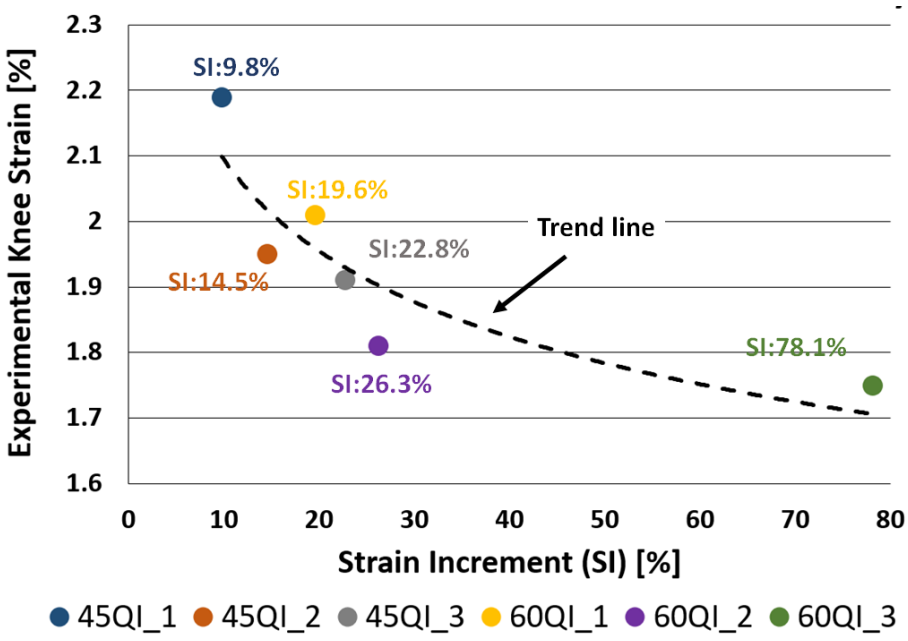

Figure 48 Correlation between the strain increment in the bottom 0° carbon ply and the experimental knee strain.

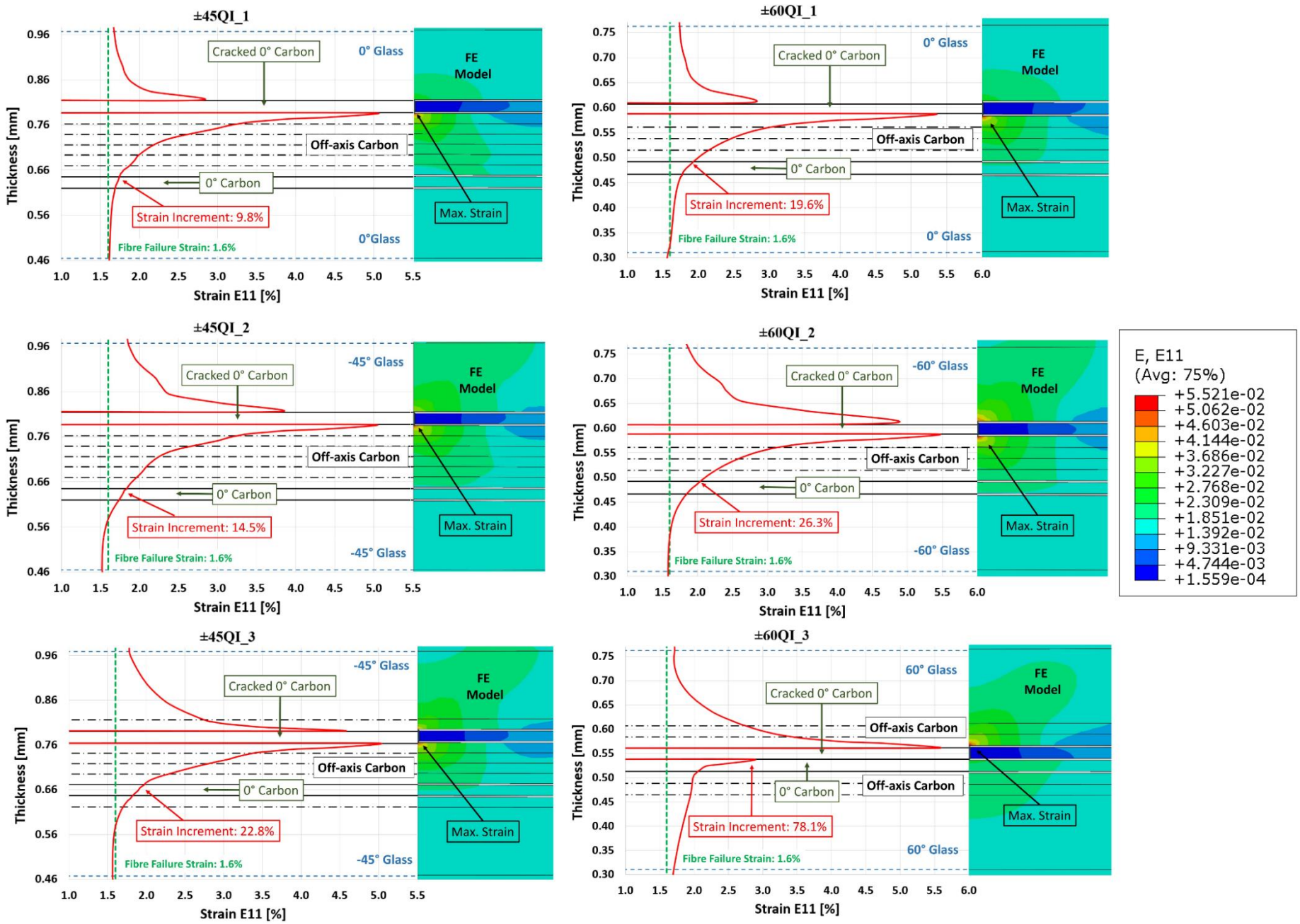

Figure 49 Strain distribution through the thickness of layups at 1.6% of strain, considering a single crack in the top 0° carbon ply.

4.8 Conclusions

The layups designed in this chapter show gradual failure with fragmentation in the 0° carbon plies and local delamination. This demonstrates that the use of damage mode maps for multidirectional composite provides a good approximation of the hybrid response.

In the multidirectional hybrid composite, not only the absolute and relative carbon thickness and material properties play an important role in the hybrid effect but also stacking sequence and the stiffness of the adjacent plies. In the layups where 0° carbon plies are closer or the stiffness of the adjacent layer is lower a higher interaction between 0° carbon plies is found, represented in a larger strain increment in the undamaged 0° carbon ply and therefore a lower hybrid effect.

Matrix cracking was observed in all the layups, which is responsible for the overall stiffness reduction of the layups. The effect of the matrix cracking was included reducing the stiffness of off-axis glass plies. However, to improve the accuracy of the model and the correlation between experimental and numerical results, micro-level mechanism such as fibre breaks and matrix cracking should be considered. Additionally, because the model does not consider these micro-level mechanisms, the strain values measured around the crack are higher than 5%. But in real conditions, these failure mechanisms dissipate energy around the fracture reducing the value of the local strain.

4.9 Recommendations and Future Works

Once it is identified the highest-performing direction in a structure, it is recommended to design the stacking sequence locating the 0° carbon plies as far apart as possible and promote that the adjacent layer corresponds to a 0° glass ply. This stacking sequence will reduce the 0° carbon plies interactions, represented in strain concentrations produced by the failure of a 0° carbon ply, and locally contained micro-failure mechanisms. In this way, the hybrid response will be optimised in the highest performing direction.

As future tasks, it is recommended to increase the experimental results proposing other stacking sequences reducing the gaps in Figure 48. To improve the microscope evidence, interrupting test just before and after the knee point allowing to have a better picture of plies interactions. Finally, consider micro-failure mechanisms like matrix cracking and fibre breaks in the model to increase accuracy.

CHAPTER 5 GRADUAL FAILURE IN COMPOSITES BENDING BEHAVIOUR

5.1 Introduction

This chapter introduces new composite architectures using carbon and glass fibre-reinforced epoxy prepregs to achieve gradual failure under flexural loading conditions. The concept is based on a technique introduced in section 2.7 and 2.8 to design hybrid composites with gradual failure in tension combined with beam theory to identify and control the failure sequence of the plies in the layups. The layups are designed to promote failure in tension and avoid catastrophic failure in compression. Two layups are designed based on standard ply thickness S-Glass and hybrid sub-laminates made out of intermediate and high modulus thin-ply carbon prepregs. The layups are tested under 4-point bending loading where a gradual failure alongside high values of flexural displacement is achieved. No catastrophic failure is observed throughout the whole loading process. The gradual layer-by-layer failure of the surface layers on the tensile side produces a brush-like appearance. Microscopy observations from interrupted tests verified fragmentation followed by local delamination on the tensile side of the beam as the main mechanism stopping catastrophic delamination. Additionally, stable shear cracks at an angle between ±45° and ±60° to the fibre direction were also identified as a unique failure mechanism in compression. Three finite element models are proposed, two of them taking into account nonlinearities produced by geometric deformations. The failure sequence and failure mechanisms are analysed using the models.

5.2 Material and Configuration Design

5.2.1 Concept

As it was mentioned previously in section 2.10, the failure of non-hybrid composite layups under bending conditions often occurs on the compressive face, because the compressive failure strain is generally lower than the tensile failure strain [86]–[89]. The dominant failure modes in UD composites under compression is micro-buckling, which lead to a catastrophic failure of the composites. To achieve gradual failure in bending, it is aimed to avoid compressive failure initiation so that the tensile side fails first. This is done by designing hybrid layups with higher compressive failure strain than tensile failure strain on one side of the laminate and achieving a stiffness reduction due to distributed damage in the 0° plies on the tensile side.

The layups proposed are hybrid carbon/glass composites, using standard thickness S-Glass on the compressive side and thin-ply carbon/carbon hybrid sub-laminates on the tensile side. The carbon/carbon hybrid sub-laminates are repeated through the thickness as a "building block" to obtain the desired total thickness. The building block corresponds to a basic unit made out of intermediate (IM) and high (HM) modulus thin-ply carbon prepregs: (IM Carbon$_i$/ HM Carbon$_k$ / IM Carbon$_i$) where i and k, are the number of plies selected for each material. Using damage mode maps, the building blocks were designed to guarantee initial fragmentation of the high modulus carbon layer without catastrophic failure of the intermediate modulus carbon layer.

5.2.2 Materials

Standard ply thickness S-glass/epoxy prepregs supplied by Hexcel with the epoxy resin system 913 are used for the compressive side. On the tensile part of the beam, it was decided to make hybrid sub-laminates out of T1000 and M55 thin-ply carbon/epoxy prepregs from North Thin Ply Technology (NTPT). The T1000 intermedium modulus (IM) carbon fibres have a tensile failure strain of 2.2% and the tensile failure strain of M55 high modulus (HM) carbon fibres is reported to be 0.8% [10]. The epoxy resin systems in both prepreg layer systems are Thin-Preg 120 EPHTg-402 (North TPT). The choice of fibres in tension was based on having enough difference between the tensile failure strain values of the constituents and at the same time, avoiding very low tensile failure strains at damage initiation. In this case, T1000 fibres provide a better failure strain (2.2%) response compared to TC35 (1.6%). Additionally, the results published in [78] showed that hybridising HM M55/epoxy with IM T1000/epoxy provided good results in terms of pseudo-ductile strain and gradual failure in pure tensile tests. The curing temperature implemented for all the resin systems in the used prepregs is 125°C. Although no chemical analysis on the compatibility of both resin systems was done, previous experience indicated a good bonding between both resin systems [78]. Table 10 shows the basic properties of the applied materials.

Table 10 Cured ply properties of the applied UD prepregs.

Prepreg Material	Elastic Modulus [GPa]	Tensile Failure Strain [%]	Compression Failure Strain [%]	Cured ply thickness [mm]
S-Glass/913	45.7 [111]	3.98 [111]	2.33 [111]	0.155 [111]
T1000/ Thin-Preg 120 EPHTg-402	143.3 [10]	2.2 [a]	0.95 [b]	0.032 [10]
M55/ Thin-Preg 120 EPHTg-402	280.0 [10]	0.8 [a]	0.56 [94]	0.030 [10]

[a] Fibre tensile failure strain based on manufacturer's data.

[b] Based on manufacturer's data for 60% fibre volume fraction.

5.2.3 Design of Hybrid Laminate Building Blocks

Proposing the building block architecture is the first step to design the full layups. Different combinations of M55 and T1000 layers were assessed using damage mode maps. Figure 50 shows the four possible failure processes of the M55/T1000 hybrids. The circles in the map represent the position of four different building block configurations and the coloured regions of the map indicate the favourable pseudo-ductile strain (ε_d) in the regions with gradual failure. Building blocks 1 and 2 are located in the fragmentation zone, building block 3 is located in the fragmentation and local delamination zone and building block 4 produces catastrophic delamination. The damage analysis was carried out using a mode II critical strain energy release rate of G_{IIC}= 0.5 N/mm. This critical value was selected based on observations conducted in [78] during tests on similar hybrid configurations made of

prepregs comprising the same epoxy matrix systems (Thin-Preg 120 EPHTg-402 North TPT). Table 11 shows the geometric parameters, Young's modulus and mode II energy release rate, G_{II}, at the M55 fibre failure strain of 0.8% (see Table 10). As it was mentioned in section 2.7, the energy release rate (G_{II}) must be lower than the mode II critical energy release rate (G_{IIC}=0.5) of the interface to avoid catastrophic delamination of the central M55 layer after its first fracture. This criterion is introduced in Eq. (2), which is satisfied by all building blocks proposed, except by building block 4 (see Table 11), [$T1000_4/M55_3/T1000_4$] where the calculated energy release rate G_{II} is 0.69 N/mm at the failure strain of the M55 fibre, 0.8%.

In this case for Eq. (2), E_1 and E_2 are the elastic modulus of the T1000 and M55 layers. t1 is the thickness of each block of T1000 on either side, t2 is half of the laminate thickness of M55 and ε_{2b} is the failure strain of M55. G_{II} is the energy release rate and G_{IIC} is the mode II critical energy release rate.

Table 11 Building block properties.

Building Block	Total Thickness [mm]	M55 Relative Thickness [-]	Predicted Modulus [GPa]	Calculated G_{II} at 0.8% Strain as the failure of M55 [N/mm] [a]
1. [T1000/M55/T1000]	0.095	0.323	186.6	0.26
2. [$T1000_2/M55/T1000_2$]	0.160	0.193	169.3	0.19
3. [$T1000_4/M55_2/T1000_4$]	0.320	0.193	169.3	0.39
4. [$T1000_4/M55_3/T1000_4$]	0.351	0.263	178.9	0.69

[a] Mode II energy release rate G_{II} calculated using Eq. (2)

Layups 1, 2 and 3 are located in the desirable area of the map where the failure is expected to be gradual. However, the total thickness of building block 3 is 0.32 mm which is relatively thick. Therefore, building blocks 1 and 2 were chosen for the experiments and the rest of the analysis in the next sections.

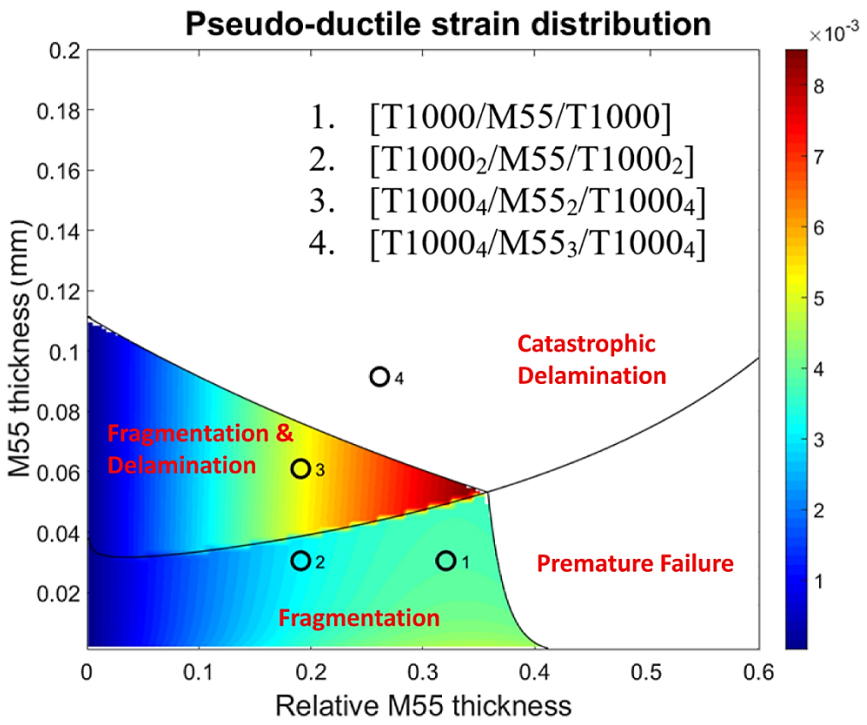

Figure 50 Damage mode map of M55/T1000 hybrid layups

Using the analytical method proposed by [76] (section 2.8), the strain-stress response of the building blocks 1 and 2 is calculated as shown in Figure 51. Building block 1 has slightly higher initial stiffness and damage initiation stress (knee point A on the blue curve) and building block 2 has a better response in terms of progressive damage (pseudo-ductile strain ϵ_d) and final failure strength (point B on the orange curve). Both configurations show acceptable behaviour in tension and they are expected to produce gradual failure in bending.

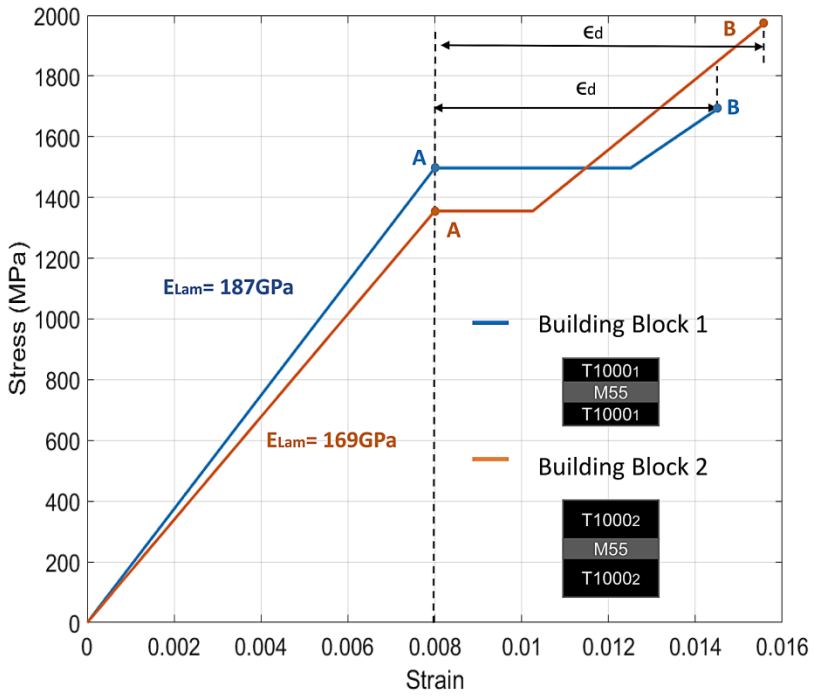

Figure 51 The tensile response of building block 1 [T1000/M55/T1000] and building block 2 [$T1000_2$/M55/$T1000_2$]

5.2.4 Full Layup Design Using Beam Theory

Different configurations were analysed using beam theory to calculate the strain distribution through the thickness. The aim is to design a beam configuration in which the glass layers under compression do not fail before the failure initiation on the tensile side of the beam. A MATLAB code, with the algorithm explained in Figure 52, was implemented to find the required failure bending moment of each layer through the thickness, based on the compressive and tensile failure strains reported in Table 10. The code provides an idea of the initial failure of the laminate, calculating the required failure moments of each layer and producing a failure sequence where the plies that fail first are those with lowest failure bending moment.

From this analysis, two layups proposed for the experimental tests are:

- **Layup 1:** [$S\text{-}Glass_7$/M55/T1000/$(T1000/M55/T1000)_{17}$/T1000] using building block 1
- **Layup 2:** [$S\text{-}Glass_7$/T1000/M55/ $T1000_2$/$(T1000_2/M55/T1000_2)_{10}$] using building block 2.

Both layups have the same total thickness to make them directly comparable, but with different ratios of T1000 to M55. For the layup 1 compared with layup 2, one ply of T1000 was relocated from the top side (close to the S-Glass) to the bottom face, in order to have the same number of T1000 layers covering the external M55 ply in tension and to promote a similar failure initiation in both layups. Seven layers of S-Glass were proposed for the compression side as this number of layers allows a safe margin between the compressive

failure of the S-glass and the tensile failure of the T1000/M55 hybrid. This should ensure that compression failure is avoided.

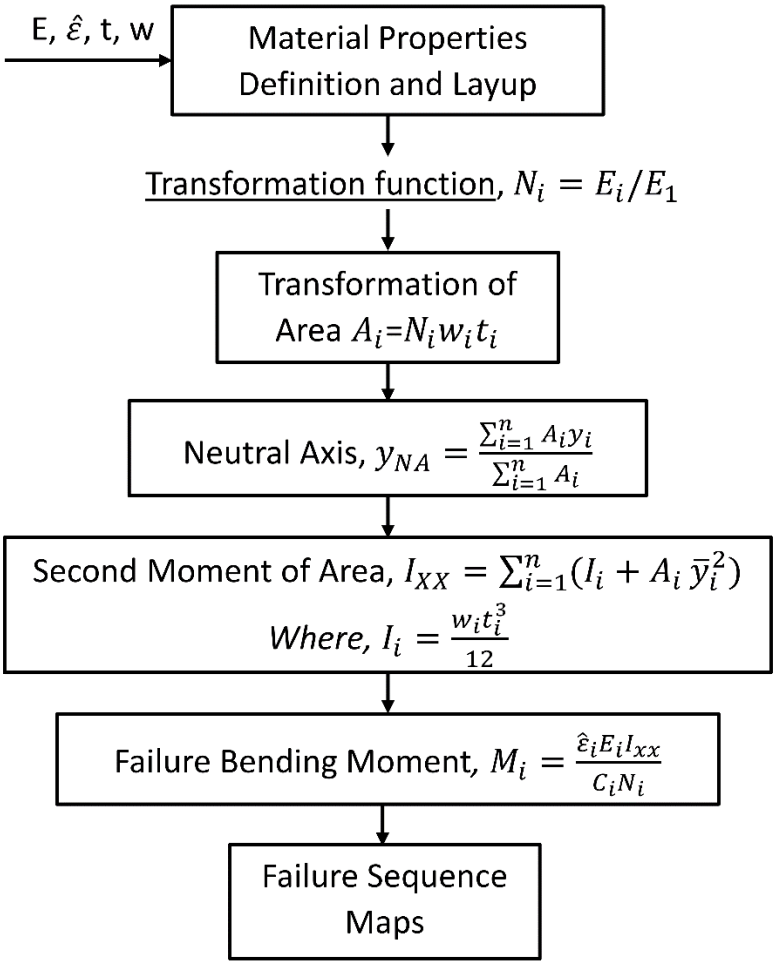

Figure 52 MATLAB code to generate the failure sequence diagram and strain and stress distribution diagrams.

In Figure 52, *E* is the young modulus, $\hat{\varepsilon}$ is the failure strain, *w* is the width and *t* is the thickness of the different layers. N_i is the transformation function to account for the different moduli, A_i is the weighted cross-section area of each layer including the transformation function, y_{NA} is the location of the neutral axis, y_i corresponds to the distance between the base of the layup (bottom face) and the centroid of layer i, I_{XX} is the layer second moment of area, $\bar{y}_i$ is the distance between layer i centroid and the neutral axis, M_i is the failure moment and C_i is the distance between the bottom surface of layer i to the neutral axis. For all the equations the sub-index i correspond to the layer number ranging from 1 to the total number of layers.

Figure 53 and Figure 54 show the position of each layer on the vertical axis and the required bending moment for the failure of each layer on the horizontal axis, with the left side layers being in compression and right side layers in tension. The blue stars, red dots and green squares correspond to the S-Glass, T1000 and M55 layers respectively. The blue dashed

lines indicate the location of the neutral axis. The code calculates the total bending moment required to break each layer in tension and compression. Layers with lower required failure bending moment will fail first. Since the main objective is to verify the initial failure order and guarantee that the failure initiation is promoted in tension, the code does not consider either the stiffness reduction of the layups because of ply failure nor the shift of the neutral axis.

The failure order of the most critical layers for the M55/T1000 sub-laminate and S-Glass is indicated in Figure 53 and Figure 54. For both layups, the layers most likely to fail first correspond to the M55 ply in tension (number 1 in the failure order), followed by the top M55 ply in compression close to the S-Glass (number 2 in the failure order). The other critical layers listed in Figure 53 and Figure 54 in the T1000/M55 sub-laminate are also M55 plies, which fail long before the T1000 plies, however, the failure order differs between the layups. Failure of S-Glass is predicted to be at 9th and 6th rank in these two layups confirming that the first failure should not be on the compressive side. Despite the top M55 layer under compression appearing likely to fail as the second layer in the failure order, it has been observed that M55 under compression can lead to fragmentation rather than catastrophic failure [92],[93]. Additionally, once the first layer fails in tension, the neutral axis will move upward, reducing the risk of compressive failure. Therefore, the design is still considered likely to avoid premature compressive failure.

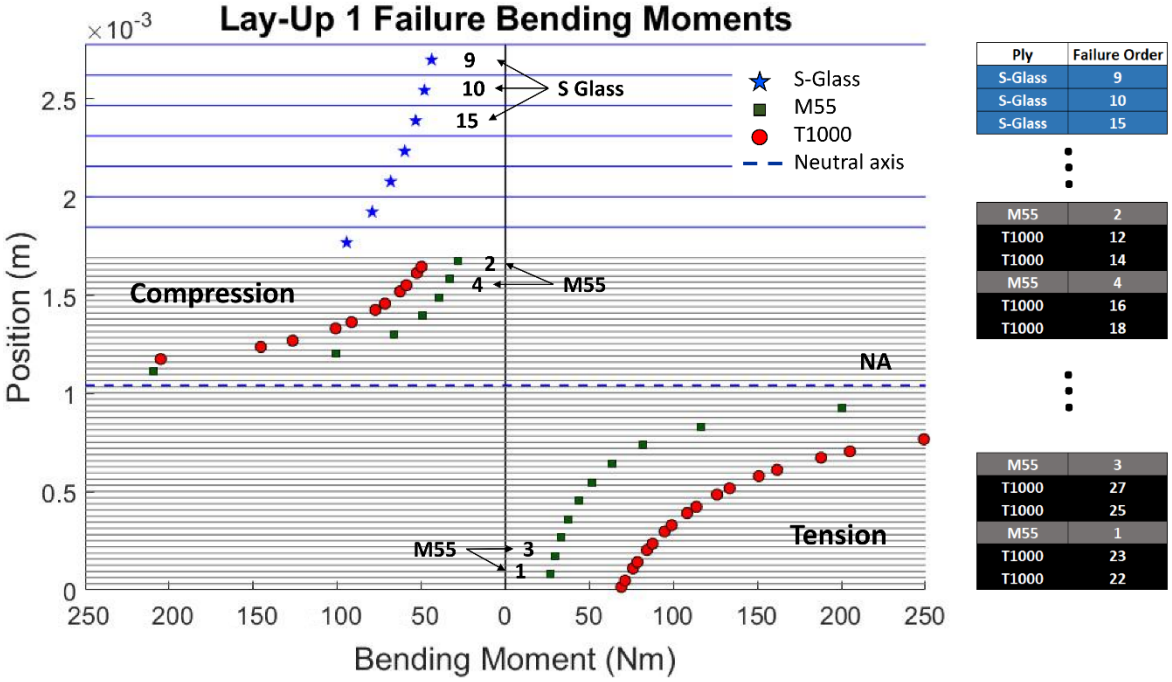

Figure 53 Bending moments for each layer showing the failure sequence of layup 1, [S-Glass7/M55/T1000/(T1000/M55/T1000)17/T1000].

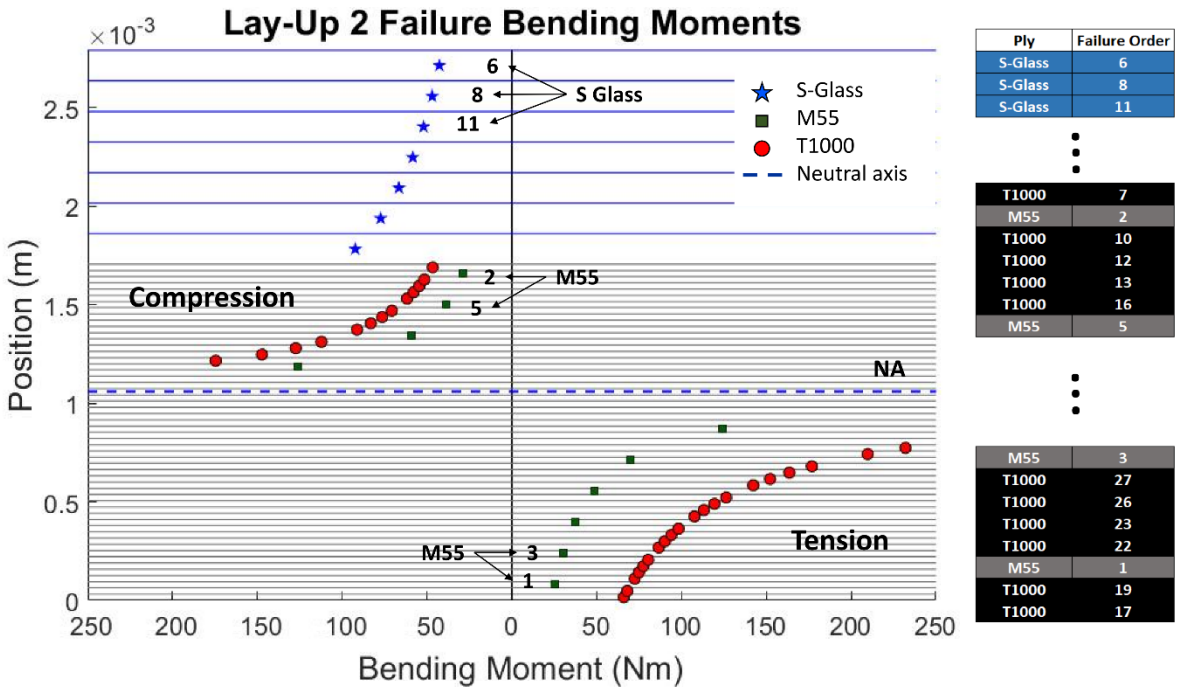

Figure 54 Bending moments for each layer showing the failure sequence of layup 2, [S-Glass7/T1000/M55/ T10002/(T10002/M55/T10002)10].

5.3 Experimental

5.3.1 Specimen Manufacturing

The interlayer hybrid specimens were made by stacking the specified glass and carbon prepregs on top of each other. Laminates were cured in an autoclave at the recommended cure temperature and pressure cycle for Hexcel 913 resin (60 min @ 125°C and 0.7 MPa), as this is similar to the NTPT thin carbon prepreg cure cycle (the curing cycle is the same used in section 4.3.1). The individual specimens were cut with a diamond cutting wheel. Six samples were obtained from each plate. Table 12 shows the dimensions of the manufactured samples.

Table 12 Dimensions of the manufactured samples

Spec. type	Length (mm)	Width (mm)	Thickness (mm)
Layup 1	190±0.19	19.93±0.10	2.92±0.05
Layup 2	190±0.34	20.38±0.05	2.96±0.08

5.3.2 Test Method

Four-point bending (4-PB) test setup was selected to achieve a constant bending moment in the middle of the beam. This assures that carbon layer failure takes place between the loading noses where the bending moment is maximum and constant whereas the shear stresses are relatively small. Rubber pads were used between the loading noses and the

samples to reduce the high and concentrated contact stresses. Figure 55 shows the schematic of the specimen geometry and the test setup including the calculated neutral axis position which is 1.049mm and 1.067mm from the bottom of layup 1 and 2 respectively. The distance between the bottom supports is 120 mm, the distance between the inner loading noses is 25 mm and the diameter of all supports and loading noses are 10mm. Four-point bending loading on the prismatic specimens was executed at a constant 3 mm/min crosshead speed on a computer-controlled Instron 8872 type 25 kN rated universal servo-hydraulic test machine with a regularly calibrated 10 kN rated load cell. Load and displacement were measured from the machine and the strains were measured using a strain gauge located on the bottom carbon ply of each sample as shown in Figure 55. Videos of the specimens were recorded for failure analysis and process characterisation.

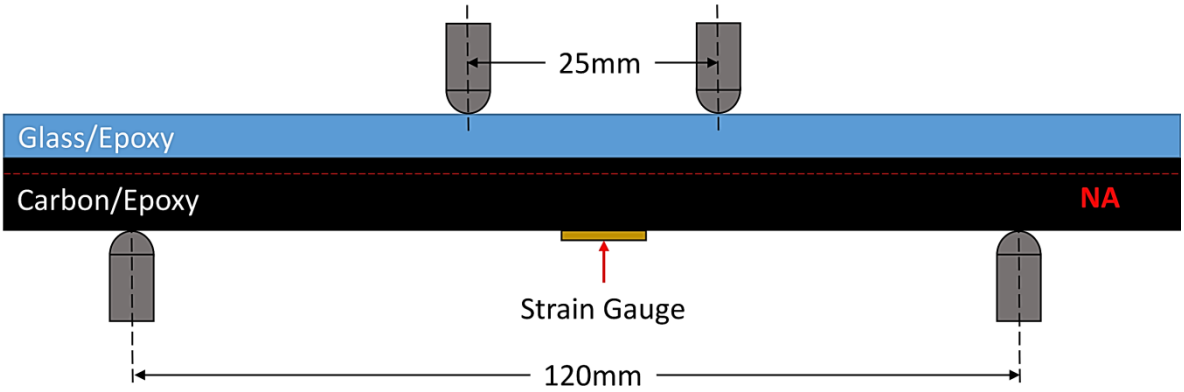

Figure 55 Schematic of the four-point bending (4-PB) test setup.

5.4 Results and Discussion

5.4.1 Test Results

The layups designed using the method proposed in section 5.3 show a successful gradual failure, displaying a brush-like appearance as shown in Figure 56b. 60mm maximum vertical displacement at the loading noses was achieved without failure through the full thickness. The tests were stopped when the samples were moved from the supporting rollers to the edge of the support block square as shown in Figure 56a. Some of the samples were interrupted earlier in order to observe the failure inside the layup under the microscope.

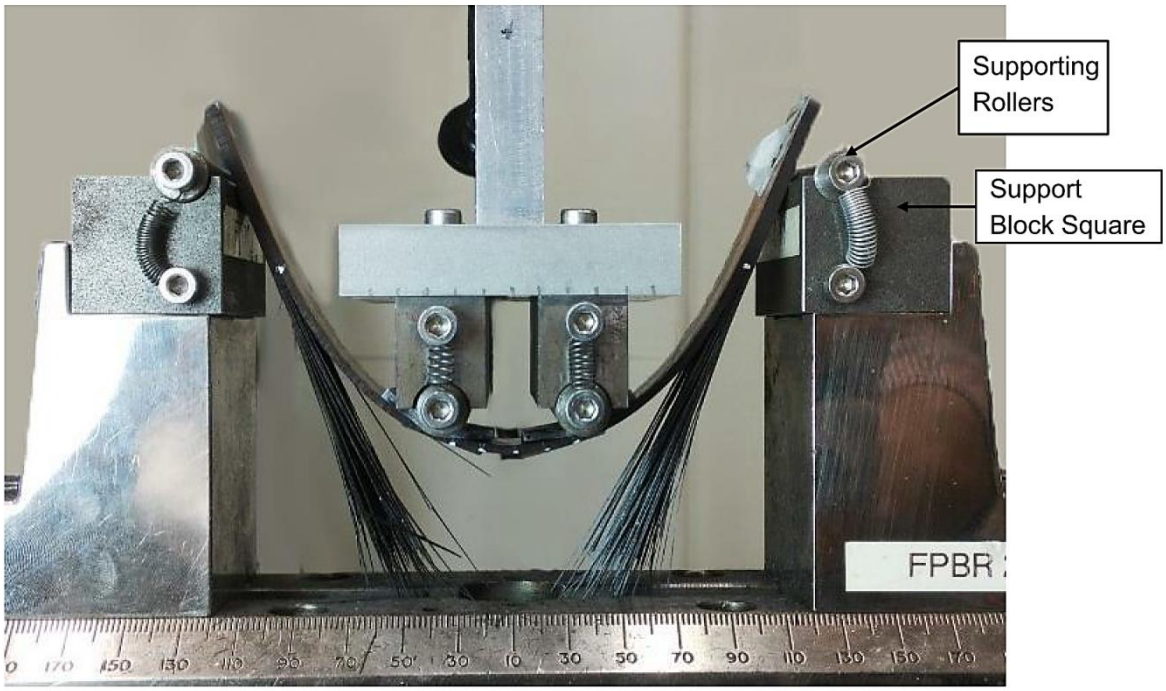

(a)

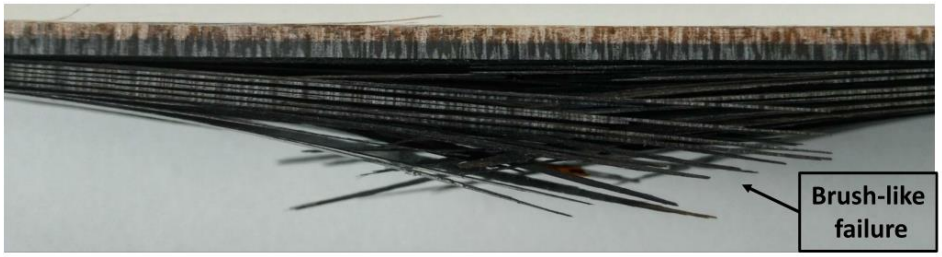

(b)

Figure 56 Four-point bending (4-PB) test, (a) high displacement results (b) brush-like failure appearance after the test.

Figure 57 shows the load-displacement graph for both layups. Both groups of samples show a high non-linear behaviour after 1.2kN and before the load drops. This behaviour is due to fragmentation of M55 plies and non-linear geometric deformation, being the geometric deformation the biggest component as it will be explained in section 5.6.2. Matching the time of the recorded videos and the load-displacement data provided by the machine and considering the large difference in the failure order between M55 and T1000 plies, it was observed that the load drops shown in the load-displacement graphs in Figure 57 are related to the failure of T1000 layers followed by instantaneous delamination of the T1000/M55 hybrid blocks from the undamaged part of the beam. This premise will be confirmed using finite elements in section 5.6.1. Layup 2 reached a slightly higher maximum load of 1.70 kN than that of layup 1, which is 1.60 kN. These results are in agreement with Figure 51 where Layup 2 (building block 2) shows slightly higher failure stress. The total energy of each specimen is calculated by integrating the area under the load-displacement curve up to a maximum applied displacement of 35mm. Both configurations give fairly close average absorbed energy of 150.8 kJ for layup 1 and 155.4 kJ for layup 2. The reason to compare

both layups only up to 35 mm applied transverse displacement is that around 36 mm, the beam touches the corner of the support block and loses contact with the support roller.

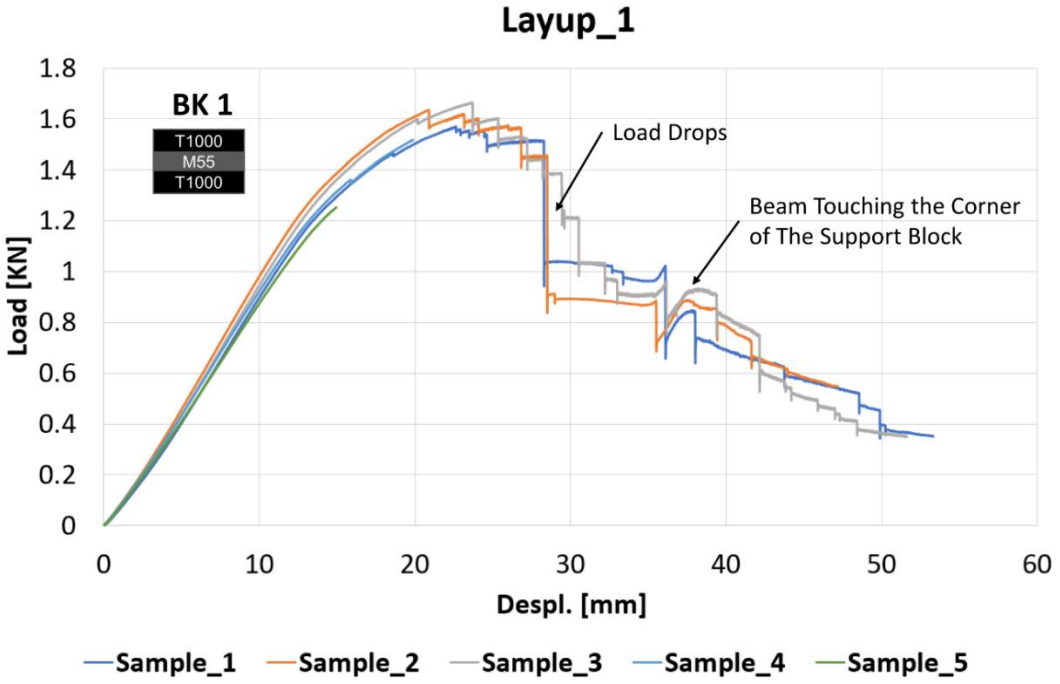

(a)

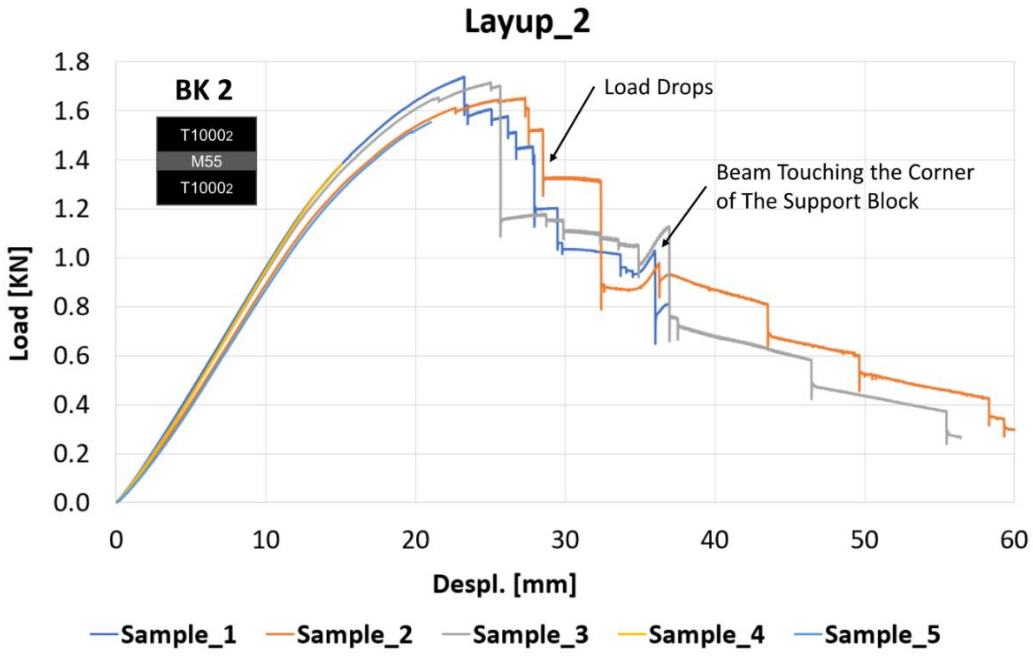

(b)

Figure 57 Load-displacement curves obtained directly from the loading machine including interrupted samples for (a) Layup 1 and (b) Layup 2, where BK1 and BK2 refer to building block 1 and building block 2.

5.4.2 Strain Gauge Results

To capture local tensile strain at the middle of the span of the beam, strain gauges were located at the bottom carbon ply. The maximum measured strains are associated with the failure of the bottom surface T1000 layers in tension, leading to strain gauges being debonded. The average strain at which the linear elastic behaviour changes is found by fitting two trendlines before and after the nonlinear point for each specimen and averaging, Figure 58 shows a schematic description. Figure 59 shows the load-strain curves where both layups display similar behaviour. At the early stage of loading, the behaviour is linear-elastic and at loads higher than 1.2kN, both layups show a non-linear response. As mentioned before, this non-linear behaviour is due to fragmentation of M55 plies and non-linear geometric deformation. For layup 1 the average strain at the non-linear initiation point corresponds to 0.90±0.06% at 1.20±0.02 kN and for layup 2, it corresponds to 0.94±0.01% at 1.21±0.02 kN.

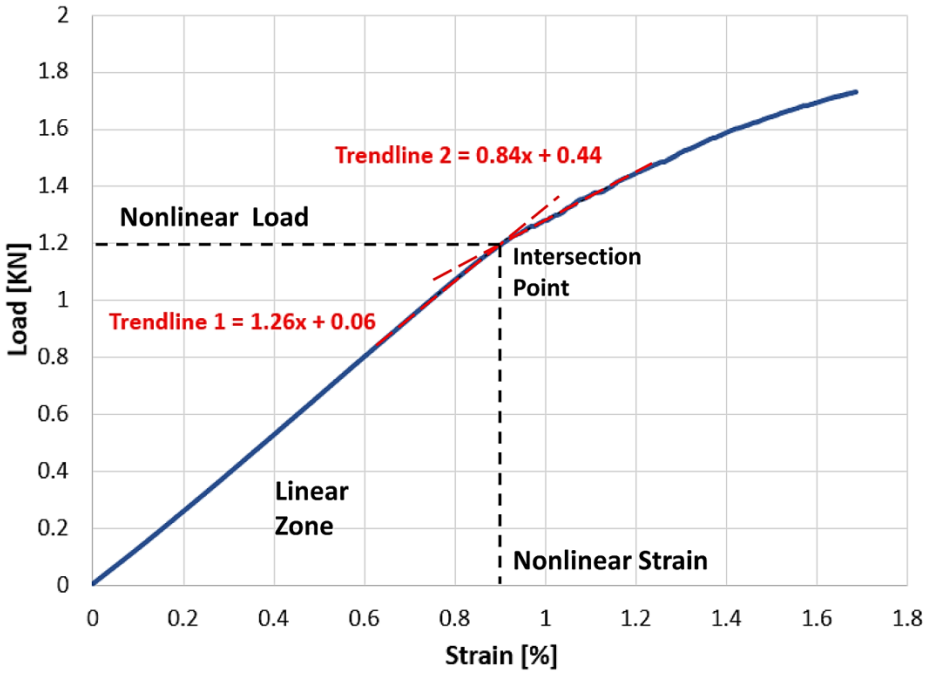

Figure 58 Definition of the nonlinear point through the intersection of trendlines and calculation of the nonlinear strain and load.

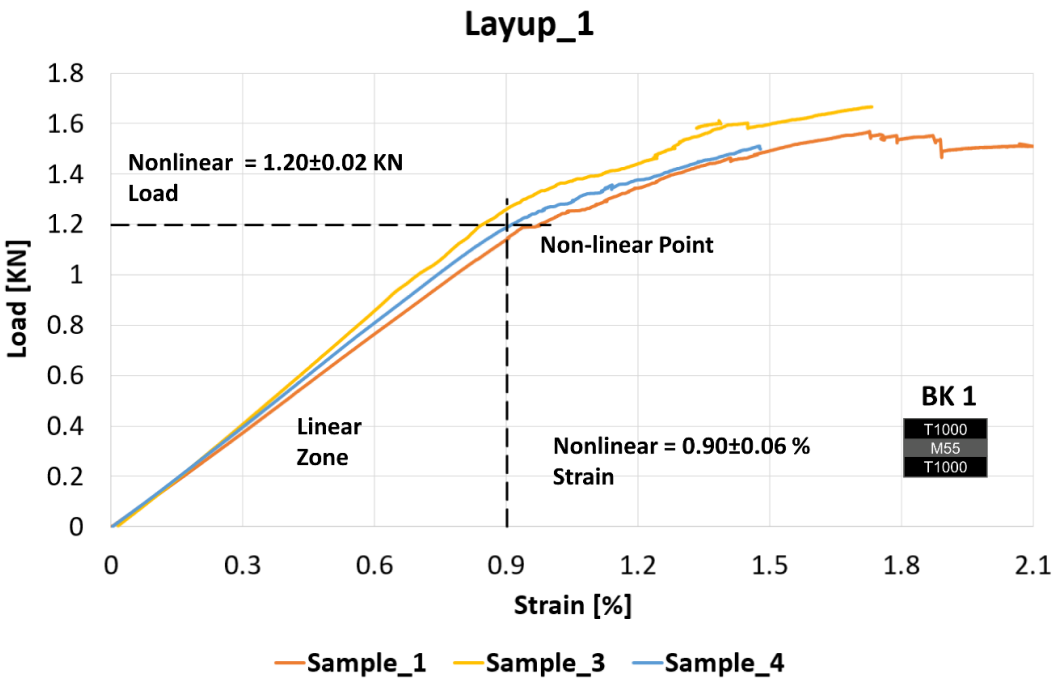

(a)

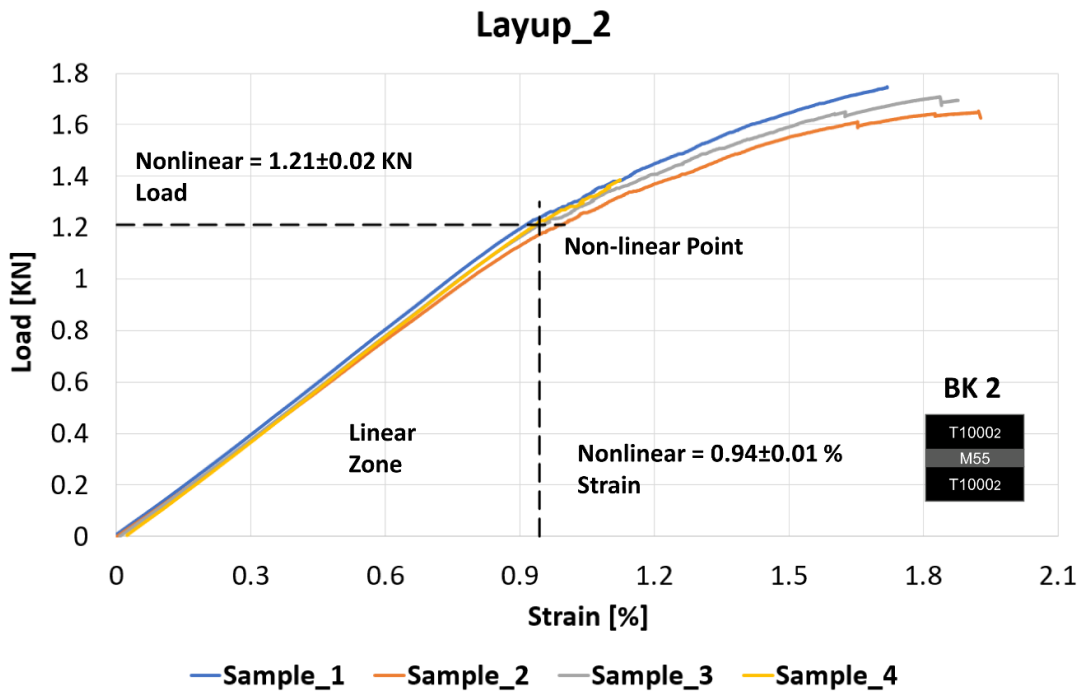

(b)

Figure 59 Load-strain curves obtained using the strain gauge at the middle of the beam on the bottom T1000 carbon ply for (a) Layup 1 and (b) Layup 2, where BK1 and BK2 refer to building block 1 and building block 2.

Figure 60 shows the strain distribution for both layups through the thickness using beam theory for an applied force of 1.2kN, which corresponds to the load at the non-linear initiation point. The maximum tensile strain at the bottom carbon T1000 ply is 0.91% and 0.95% for layup 1 and layup 2 respectively, which are very close to the experimental results using strain gauges (0.90% for layup 1 and 0.94% for layup 2). These strain values are below the tensile failure strain of T1000, 2.2%. According to Figure 60, at 1.2kN the strain in the bottom M55 layer is equal to 0.85% and 0.89% for layup 1 and layup 2 respectively, slightly greater than the quoted tensile failure strain of M55 fibres, 0.8% (see Table 10).

The maximum compressive strain for T1000 at 1.2kN corresponds to 0.54% and 0.58% for layup 1 and layup 2 respectively. These values are lower than the compressive failure strain of T1000 (0.95%). On the other hand, for M55 plies the compressive strain at 1.2kN for layup 1 is 0.57% and 0.55% for layup 2, which are similar to the compressive failure strain of M55 (0.56%). This suggests that the nonlinear initiation point is related to the starting of M55 fragmentation in both tension and compression at similar loads.

Finally, according to Figure 60 the maximum strain on the compressive side is 1.51% and 1.55% at the surface ply of S-glass for layup 1 and layup 2 respectively at 1.2kN, which is lower than the compressive failure strain of S-glass, 2.33% as reported in Table 10.

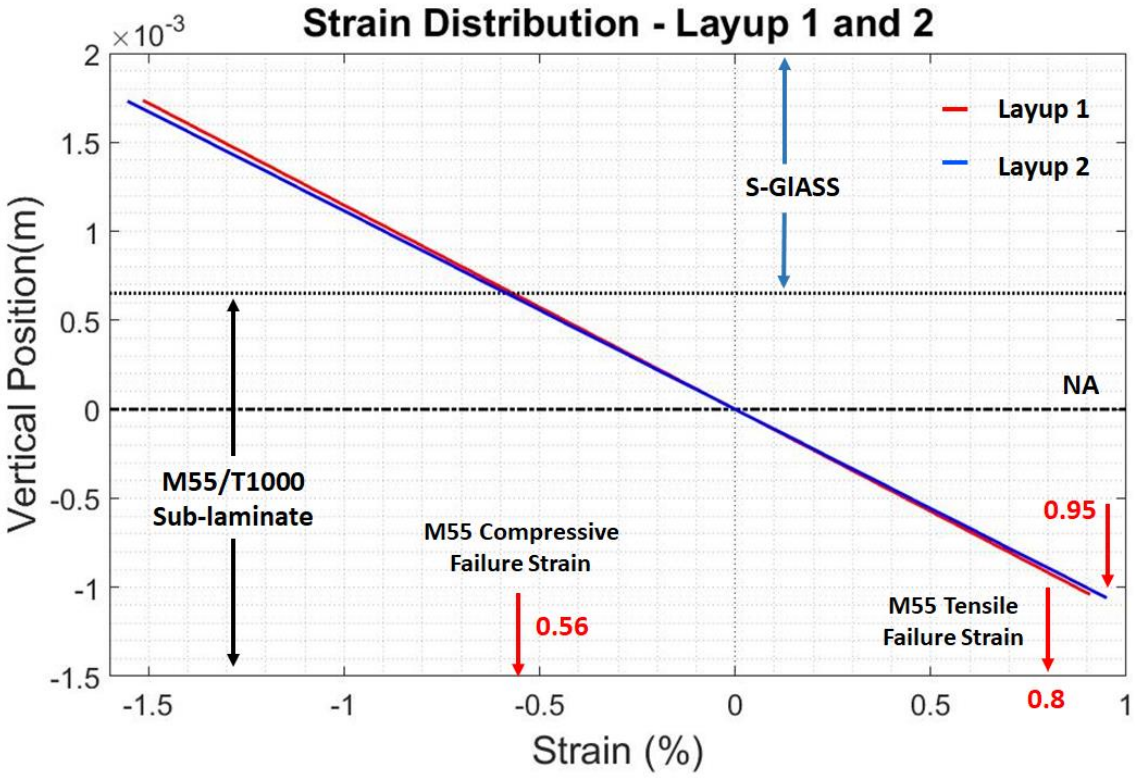

Figure 60 Strain diagrams of layups 1 and 2 at the non-linear point with a load of 1.2kN.

5.5 Microscopic Observations

The interrupted samples of each layup were observed using a Nikon Eclipse LV100 optical microscope to study the initiation of the brush-like failure mechanism. The samples were interrupted before their first load-drop (in the nonlinear section) and above 1.2 kN and beyond the first load-drop. Figure 61 shows the load-displacement curves of the samples interrupted for layup 1 and layup 2.

A section between the inner loading noses of the interrupted samples was cut using a diamond saw and embedded in Bakelite. The samples were ground 5mm along the width using 240 grit sandpaper and water as the lubricant. Then, the samples were polished using the procedure described in section 4.5.

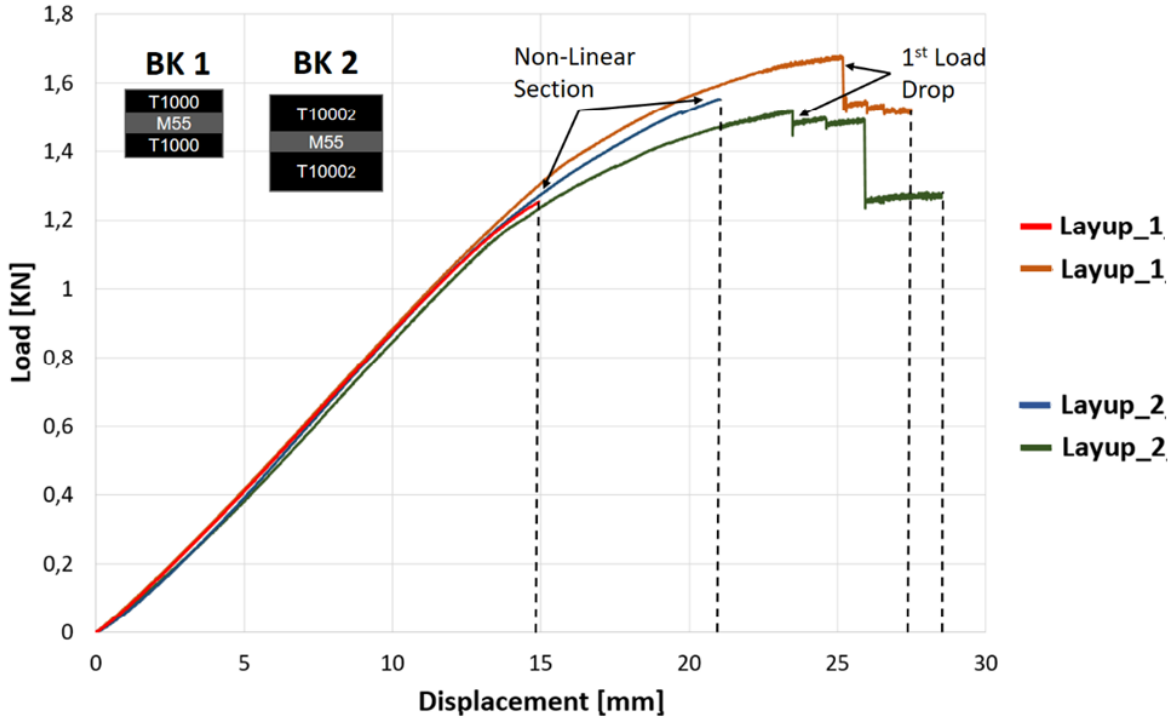

Figure 61 Load-Displacement curves of samples of layup 1 and layup 2 used in the microscopy analysis, were BK refers to building block 1 and building block 2.

The samples interrupted before the load were analysed using an optical microscope as shown in Figure 62 and Figure 63 for layup 1 and layup 2 respectively. The results are similar for both layups. Evidence of the M55 plies fragmentation in tension is highlighted with red horizontal arrows whereas T1000 layers are intact showing no damage, see Figure 62a and Figure 63a. These results are in agreement with the failure sequence introduced in section 2.3, see Figure 53 and Figure 54, where M55 plies are predicted to fail and fragment, long before T1000 plies in tension. As indicated in Figure 62c and Figure 63c, no evidence of failure in compression was observed for the sample interrupted before the load drop despite the failure order shown in Figure 53 and Figure 54 indicating that the top M55 ply would be expected to fail next after the M55 ply in tension. As mentioned before, this result is probably

because the earlier failure of M55 plies in tension modifies the position of the neutral axis, delaying the failure of the M55 plies in compression or because the compression failure strain of M55 available in the literature is still underestimated [94],[114].

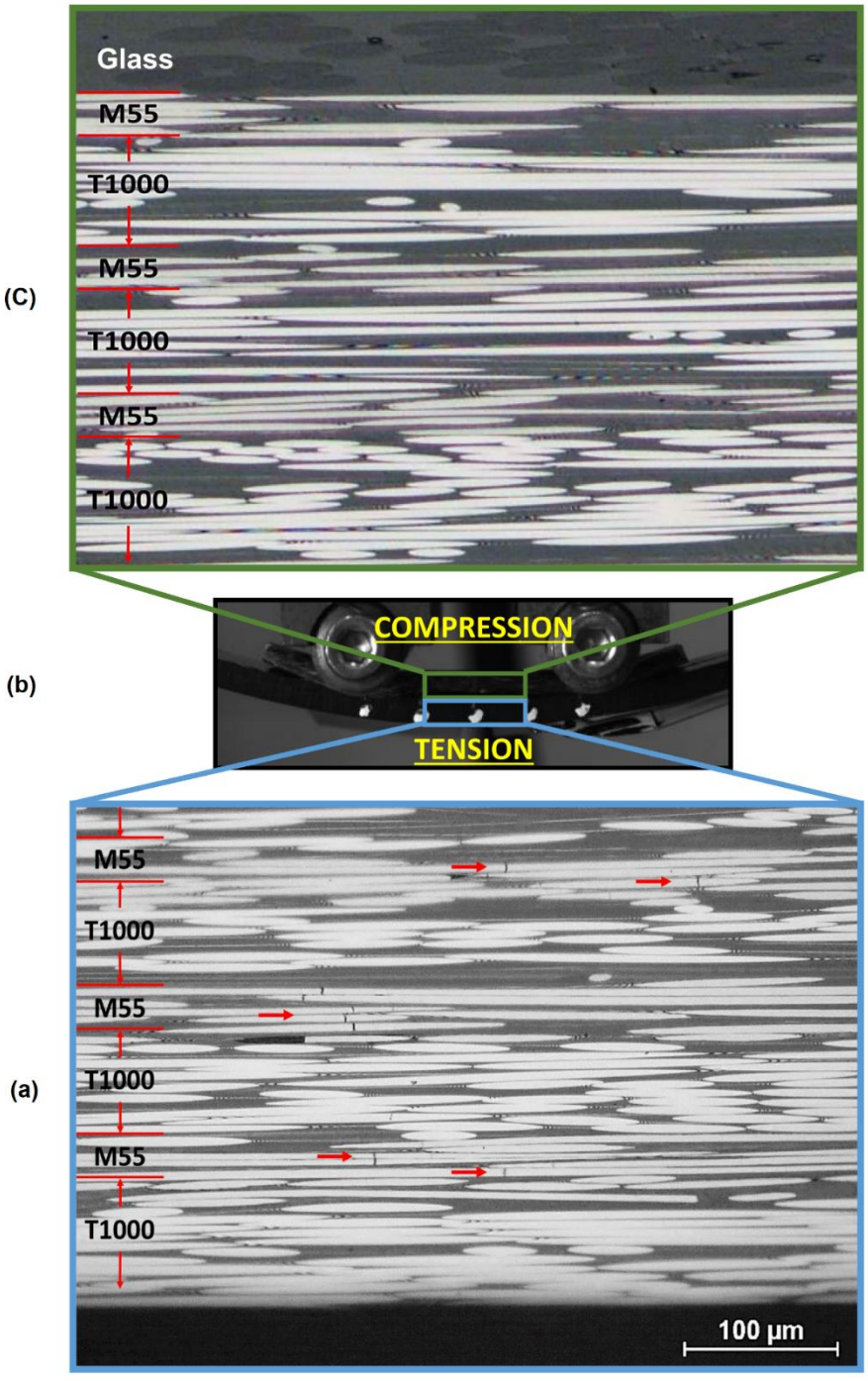

Figure 62 Tensile and compression side of Layup 1 before load drop, interrupted at 14.9mm applied displacement, (a) fragmentation of M55 plies in tension, (b) Layup 1 under load and (c) compression side of the sample.

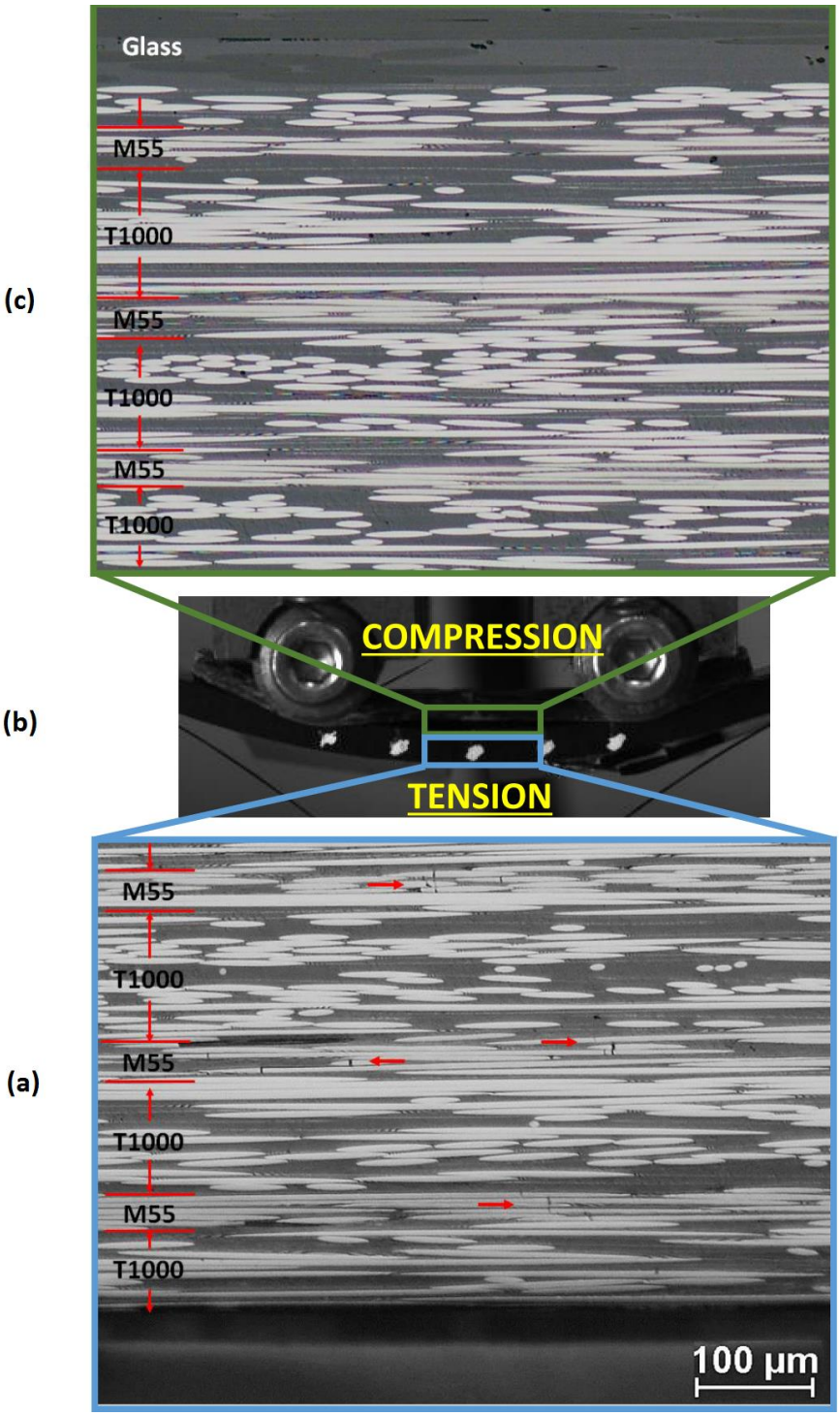

Figure 63 Tensile and compression side of Layup 2 before load drop, interrupted at 21.0mm applied displacement, (a) fragmentation of M55 plies in tension, (b) Layup 2 under load and (c) compression side of the sample.

The same process was carried out for the sample interrupted after the first load drop. Fragmentation of M55 plies, as well as local delamination, was observed in the tensile side of the beam as shown in Figure 64a and Figure 65a for layup 1 and layup 2 respectively. The fragmentations and local delaminations are highlighted by small horizontal red arrows in Figure 64a and Figure 65a. No evidence of fragmentation or damage was observed in the T1000 layers that are still attached nearer the middle of the beam. This means that the failed T1000 layers at the load drop, fracture only at one point along the length of the specimen and then delaminate, producing the brush-like failure appearance on the tensile side as shown in Figure 64b and Figure 65b. This will be described better in section 5.6.1.

On the compression side, cracks in the M55 plies were identified for the specimen loaded beyond the first load drop as shown by the red arrows in Figure 64c and Figure 65c for layup1 and layup 2 respectively. Similar to the results reported in [57],[93],[94], most of the identified cracks in compression are oriented at an angle between ±45° to ±60° relative to the fibre direction, which suggests that the fractures were caused by translaminar shear without kinking. Finally, it is worth to mention that no failure was found in either S-Glass or the T1000 plies in compression, which means the proposed stacking sequences, and the materials selected for the layups provide a good margin between compressive and tensile failure.

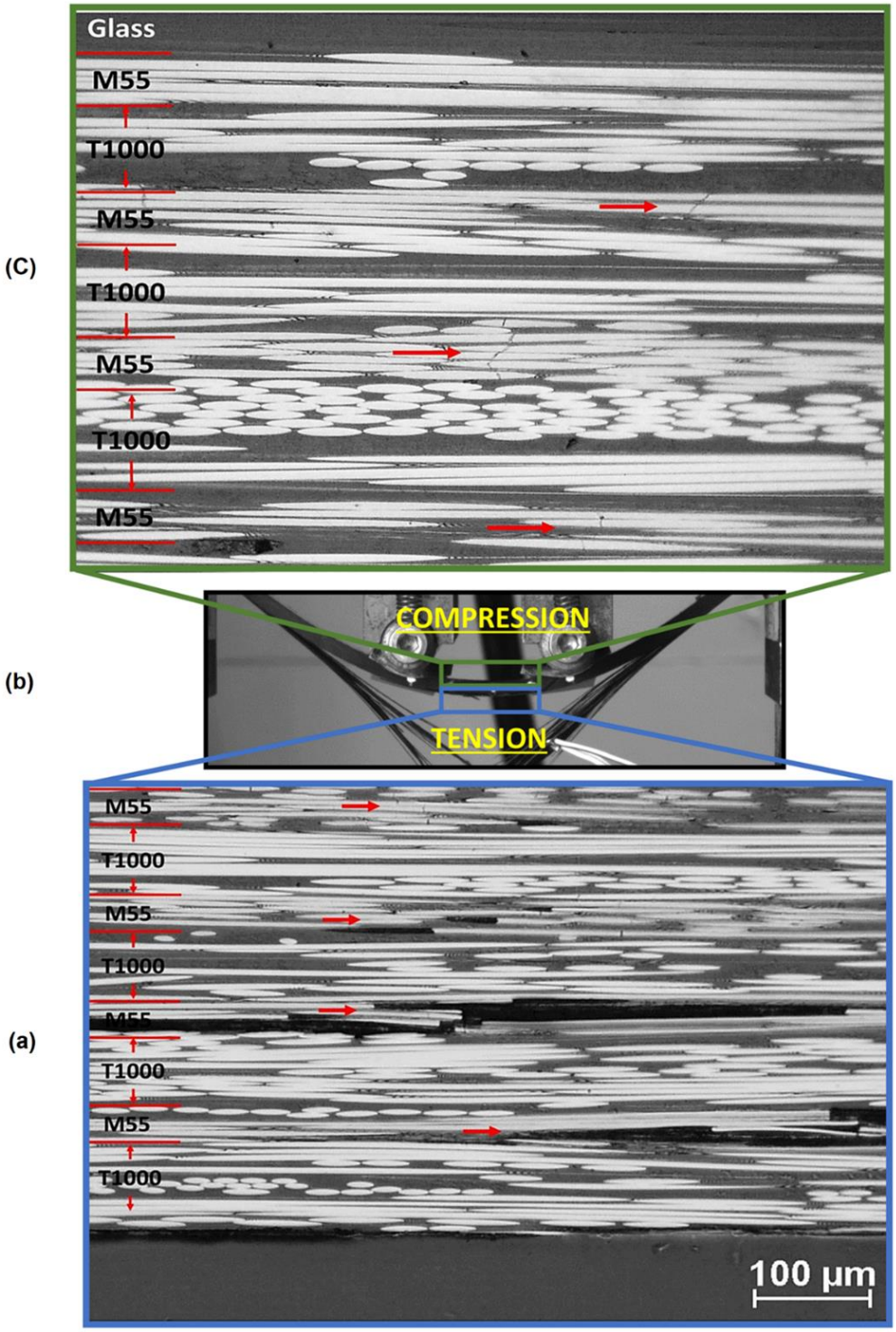

Figure 64 Tensile and compression side of Layup_1 interrupted after the first load drop at 27.5mm applied displacement, (a) fragmentation and local delamination of M55 plies in tension, (b) Layup 1 under the load showing the brush-like failure and (c) shear cracking of M55 plies in compression.

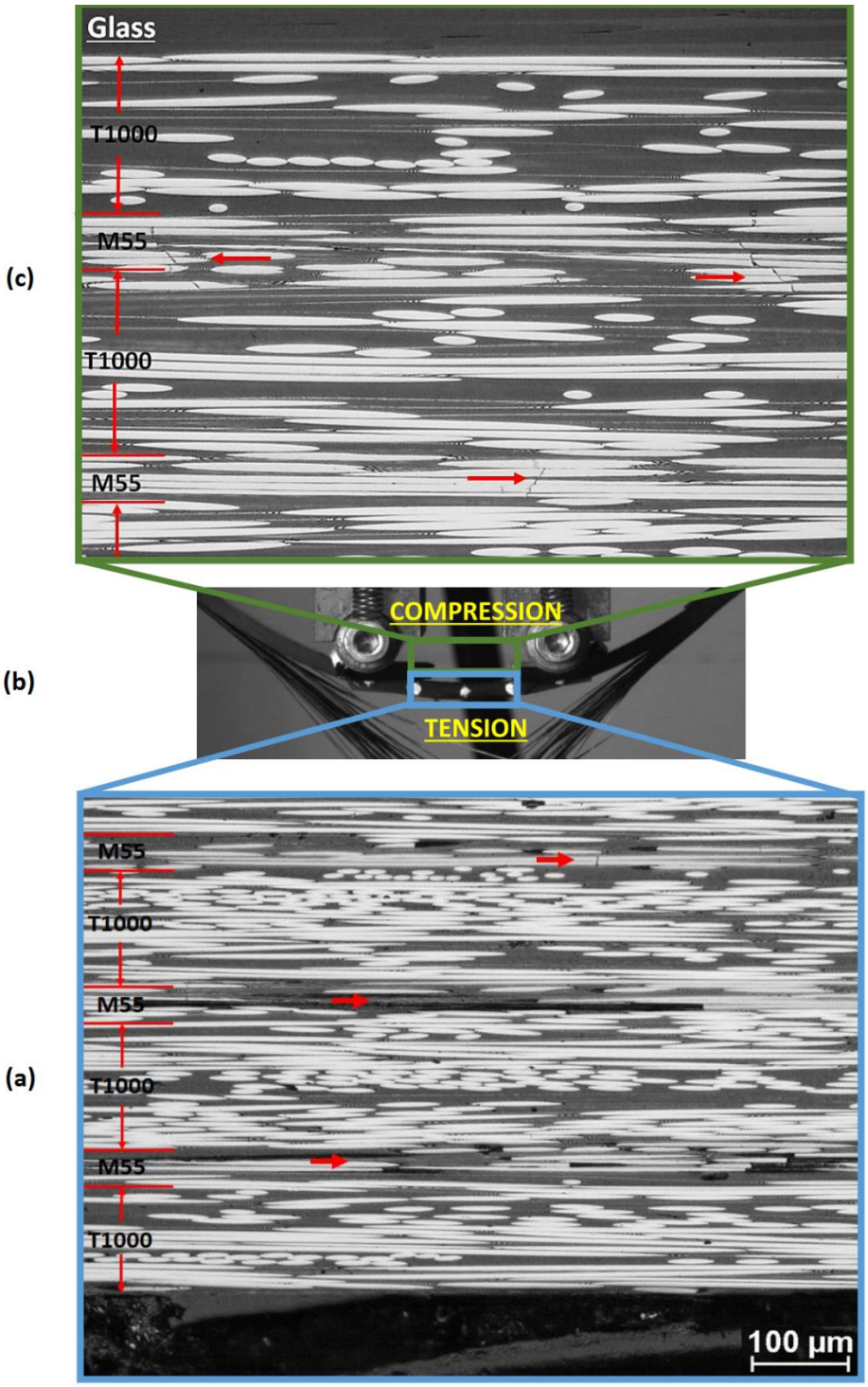

Figure 65 Tensile and compression side of Layup_2 interrupted after the first load drop at 28.9mm applied displacement, (a) fragmentation and local delamination of M55 plies in tension, (b) Layup 2 under the load showing the brush-like failure and (c) shear cracking of M55 plies in compression.

5.6 Numerical Modelling

This section aims to understand the failure sequence and the effect of the geometric nonlinearities in the behaviour of the layups proposed using numerical modelling. Section 5.6.2 and 5.6.3 show the results of joint research work with Juan Macias Lopez and part of his master thesis [114]. The models are designed based on layup 2, however, due both layups have similar behaviour and the failure mechanisms are the same, results and conclusion apply as well for layup 1.

5.6.1 Plane Strain Linear Elastic Model.

The model is developed in Abaqus and the stacking sequence corresponds to Layup 2. The model is a 2-D finite element model with 8-node quadratic plane strain elements with linear elastic material properties and non-elastic cohesive elements. For this model, it is not considered the nonlinear effects of large displacement in Abaqus, so the response of the model is linear. The noses are modelled as rigid bodies, with a maximum vertical displacement of 40mm for the loading noses, the simulation is displacement controlled. The contact between the noses and the sample is modelled using a surface-to-surface contact (standard) with tangential behaviour and a friction coefficient of 0.15 (this value was used based on recommendations of experts from the University of Bristol). The failure is modelled using intralaminar and interlaminar cohesive elements, considering fracture of plies and delamination. It is assumed that the failure of the plies take place just in the middle line of the sample, where a row of intralaminar cohesive elements are used (see Figure 66). Cohesive elements are implemented through the thickness from the bottom of the sample up to a length of 1mm which is close to the location of the neutral axis for an intact layup, see section 5.3.2. Due to differences in strength and stiffness of M55 and T1000 plies, the properties in the cohesive elements are different as well, being white the cohesive element of M55, red the cohesive elements for T1000 and green the interlaminar cohesive elements, see Figure 66. A total of 120.270 elements and 391.661 nodes are implemented and the mesh is refined in the section between the loading noses where failure is produced. The analysis was not completed and the model was stopped after 78 hours running. Machine consumption was higher during delamination processes than plies fracture.

Table 13 shows the properties of the materials used in the model, the tensile strength and the compressive strength is calculated based on the failure strains reported in Table 10 and the elastic modulus in the fibre direction (E11). On the other hand, Table 14 shows the properties of the intralaminar and interlaminar cohesive elements, the stiffness of the cohesive elements is calculated using Eq. (7). For the interlaminar cohesive zone, the cohesive zone length is calculated using Eq. (16) to Eq. (18) assuming the properties of T1000 plies since the results are more conservative. The cohesive zone length is 8.6mm and following the recommendations of Turon et al. [109] of a minimum of 3 cohesive elements in the cohesive zone, the maximum element size is 2.9mm. On the other hand, to calculate the intralaminar cohesive zone length, a variation of the Hillerborg constant for orthotropic materials in mode I is used [103], Eq. (19).

$$l_{cz} = E_I^{'} \frac{G_{IC}}{\sigma^0} \quad \text{Eq. (19)}$$

Where $E_I^{'}$ is an equivalent elastic modulus for orthotropic materials, which is calculated using Eq. (20) and Eq. (21), G_{IC} critical strain energy release rate in mode I of the cohesive zone and σ^0 is the tensile strength of the cohesive zone (for more details see [103]).

$$\frac{1}{E_I^{'}} = \sqrt{b_{11}b_{33}/2}\sqrt{(b_{33}/b_{11})^{1/2} + (2b_{31} + b_{55})/2b_{11})} \quad \text{Eq. (20)}$$

$$b_{11} = 1/E_{11},\ b_{33} = 1/E_{33},\ b_{31} = -v_{31}/E_{33},\ b_{55} = 1/G_{31} \quad \text{Eq. (21)}$$

Using the properties of M55 and T1000 indicated in Table 13 and critical energy release rates in mode I in Table 14 (this value is not reported in the literature and it was approximated to mode II) in Eq. (19) the intralaminar cohesive zone length l_{cz} is about 0.08mm for both M55 and T1000. Then, the maximum element size is 0.02mm.

Table 13 Material properties used in the numerical model.

Property	**S-Glass**	**T1000**	**M55**
E11 [N/mm^2]	45600	143300	280000
E22 [N/mm^2]	15400	6060	6060
V12	0.3	0.32	0.32
V23	0.45	0.45	0.45
G12 [N/mm^2]	4340	2400	2400
G23 [N/mm^2]	5310	2090	2090
Tensile Strength [N/mm^2]	1818	3152	2240
Compressive Strength [N/mm^2]	1065	1361	1568

Table 14 Properties of interlaminar and intralaminar cohesive elements.

Interlaminar		**Intralaminar**			
All layers		**T1000**		**M55**	
$\boldsymbol{\tau^0}$ [N/mm^2]	67	σ^O [N/mm^2]	3152	σ^O [N/mm^2]	2240
K	1x10^6	K	1x10^9	K	1x10^9
G_{IIc}	1	G_{Ic}	1	G_{Ic}	0.5
Thickness [mm]	0.0025	Thickness [mm]	0.0025	Thickness [mm]	0.0025
Element size [mm]	0.25	Element size [mm]	0.01	Element size [mm]	0.01

The model does not consider the failure in compression, however, the compressive stresses of the carbon plies in the compression zone were monitored to identify if the compression strength is reached.

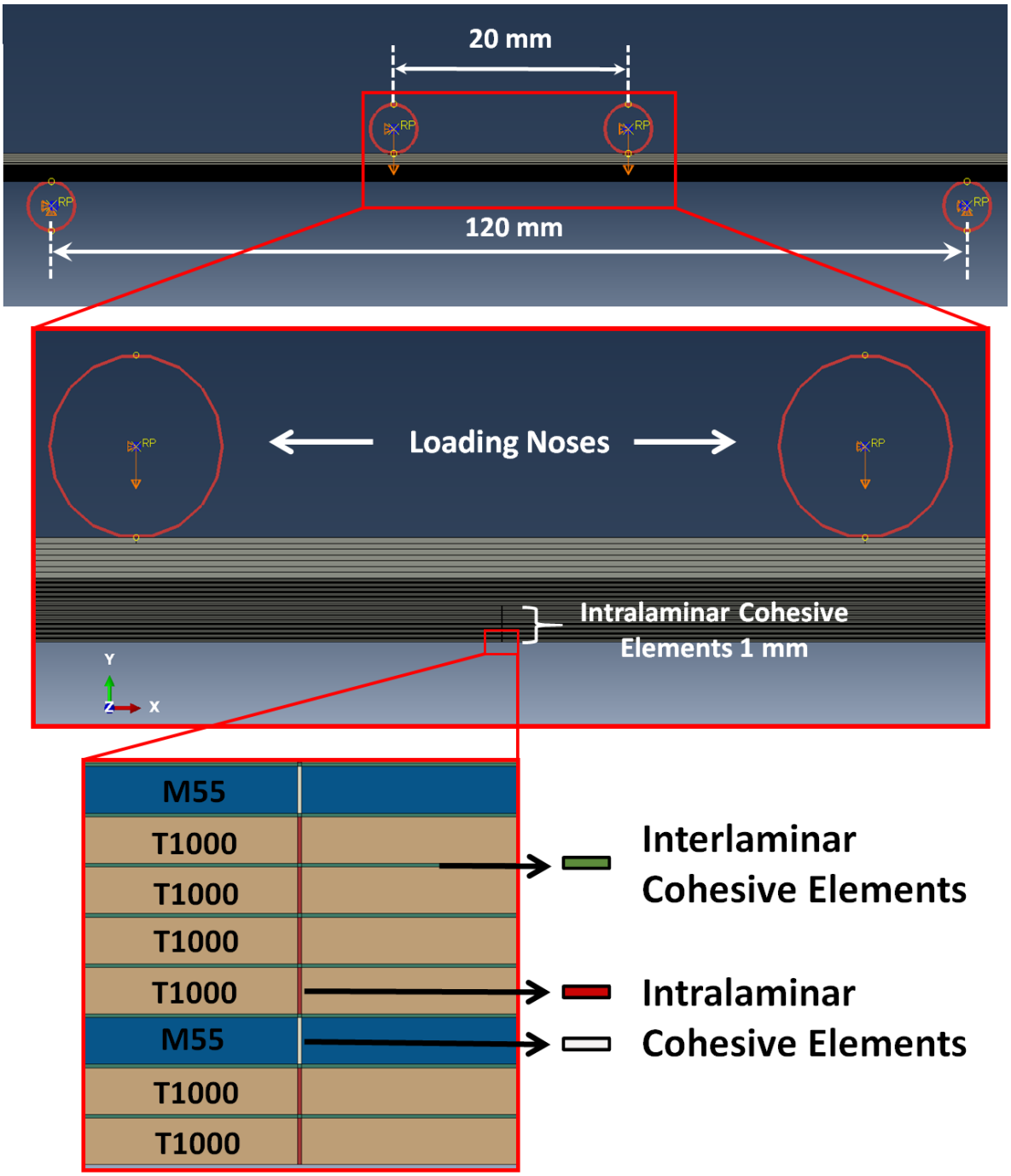

Figure 66 2D finite element model using interlaminar and intralaminar cohesive elements.

The results of the model are shown in Figure 67. The model predicts adequately the failure behaviour showing a brush-like failure appearance and gradual failure in tension, see Figure 67a. The reaction force and displacement were measured in the loading noses, obtaining the force vs displacement curve in Figure 67b. The results of the model are compared with the experimental curve of sample 1 of layup 2 (red experimental curve). The model shows good accuracy in the elastic part with a similar stiffness compared with the experimental curve and reaches a maximum force of 1.72KN, quite similar to the experimental curve which

reports 1.74KN. However, the first load drop occurs at a displacement lower in the numerical model, this difference is likely due to the properties used in the intralaminar cohesive elements are assumed.

Using the numerical model the failure sequence and failure mechanisms were monitored in the carbon plies, the steps where failure occurs are highlighted using blue and purple dots in the displacement vs force curve:

- Between points **1** and **2** in the curve, it was possible to identify the failure of M55 plies in tension and compression followed by localised delamination in tension. The failure sequence of this section of the curve is presented in more detail to the right side of Figure 67b. Analysing the first set of plies, the failure sequence is similar to the results obtained using the code in section 5.2.4, see Figure 54. However, due to stress concentrations produced by the failure of the bottom M55 ply, the T1000 ply just below fails much earlier (number 6^{th} in the failure order), while the code predicts the failure of the same ply at 19^{th} rank. Due to the code does not consider stress concentration and the move of the neutral axis, the failure order is only similar for the first set of plies. It is worth to mention, that the failure of M55 plies is present in different sections of the curve, during all the displacement process, but it does not affect the stiffness or produce load drops in the curve.
- Unlike microscope observation and similar to the results of the code, compression failure of M55 plies is expected in the nonlinear section of the curve. This could suggest that M55 compression strength is higher than the values reported in the literature, as it was mentioned before in section 5.5.
- In points **2,4,5,7,9,** blocks of T1000 plies just below an M55 ply fail. These blocks, including the M55 ply, start to delaminate producing the load drop. This agrees with the premise mentioned in section 5.4.1, where test the videos records, suggest the load drops matches with the failure of M55/T1000 blocks.
- In points **3,6,8,10,** delamination is completed and the plies of the delaminated block are pulled out from the section between the loading noses. After this, the laminate recovers its load capacity and the stiffness increase in the displacement-force curve. The recovery in the load capacity is due to the external work is no longer used to produce delamination, allowing the middle section of the sample to be loaded again.
- Between points **4** and **6**, three blocks of plies delaminated in a row, then the laminate is not able to recover the load capacity, and therefore, the load drop is larger in this section.

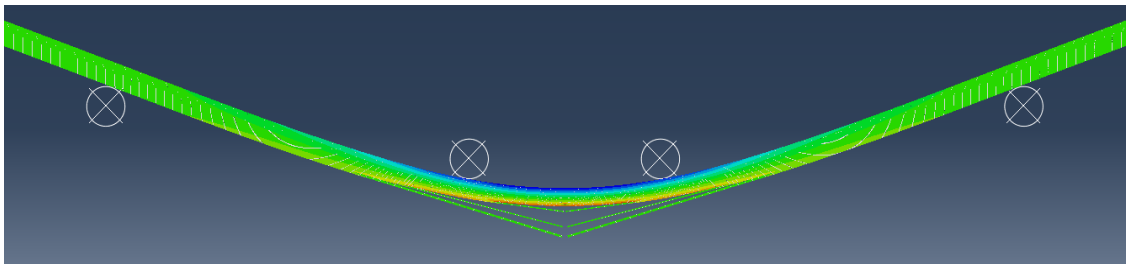

a)

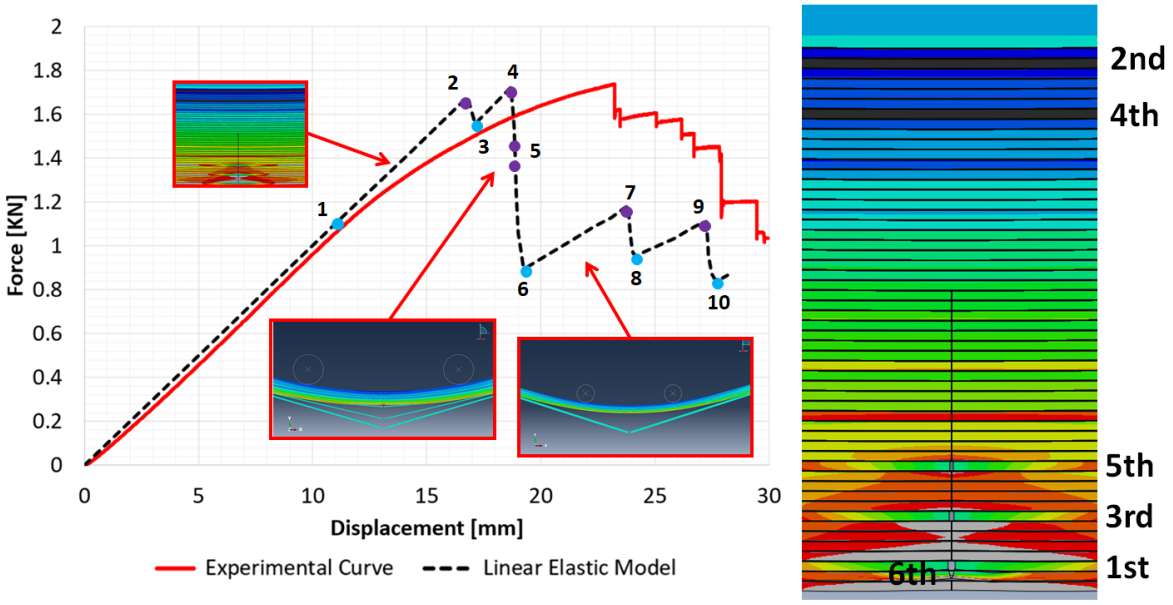

b)

Figure 67 Results of the using the 2D plane strain linear elastic model. a) brush-like failure appearance and gradual failure in tension. b) force-displacement curve and failure sequence (experimental curve corresponds to sample 1, layup 2).

5.6.2 Nonlinear Elastic Model Using Shell Elements.

Macias [114] introduced the nonlinear effects of large displacements in the model. He initially proposed a model to capture the non-linear response produced by contact interactions and large deformations only, without considering failure. He modelled the laminate using shell elements with a quadratic formulation and reduced integration. The geometry of the laminate is shown in Figure 68 and it corresponds to a rectangular surface with no thickness, because the thickness, as well as the stiffness, are given by the assignment of the layup section in Abaqus. The boundary conditions were imposed by frictionless-contact interaction with the loading noses (upper noses) and support noses (side supports), the noses were modelled as rigid shell bodies. Force reaction and displacement were measured in the loading noses.

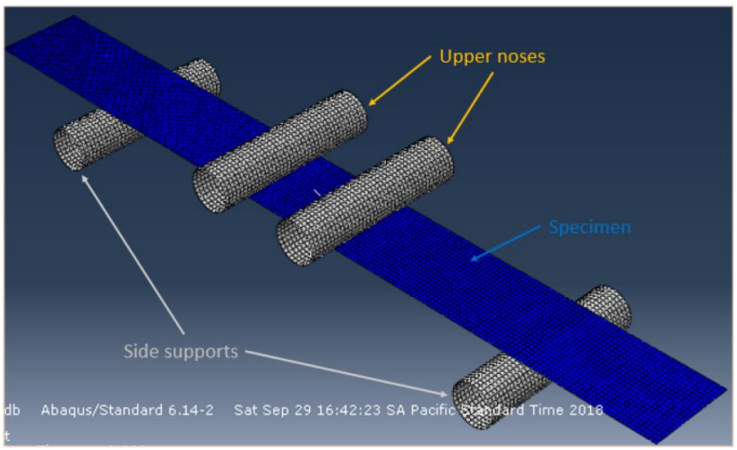

Figure 68 3D Nonlinear Elastic Model Using Shell Elements.

The results of the model are shown in Figure 69 and compared with the experimental results of layup 2. Figure 69a shows the model loaded, where high deformations are observed. Considering that the model does not include failure conditions and the good agreement between the experimental and the numerical results in Figure 69b, it was concluded that most of the nonlinear response is caused by large geometric deformations and the influence of M55 fragmentation is low. However, as it was demonstrated before in section 5.4.2, the initiation point of the nonlinear curve match with the starting of the M55 fragmentation in tension. This means that despite fragmentation is not the main component which produces the nonlinear response, it contributes to the initiation of nonlinear behaviour.

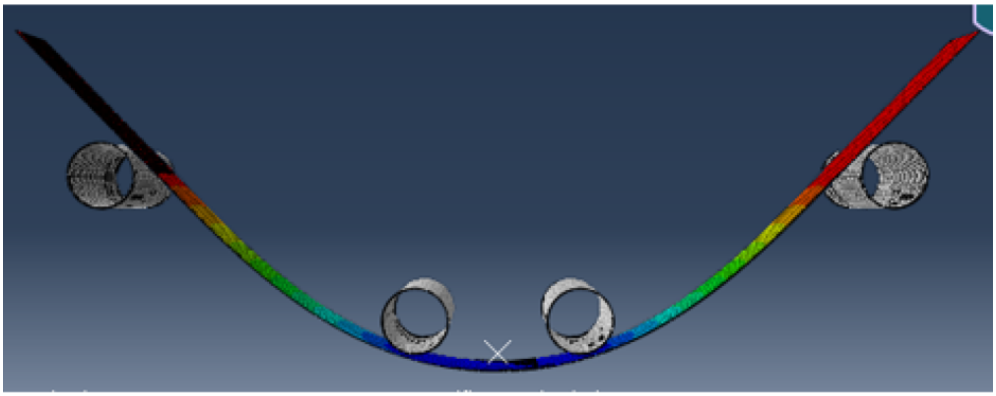

a)

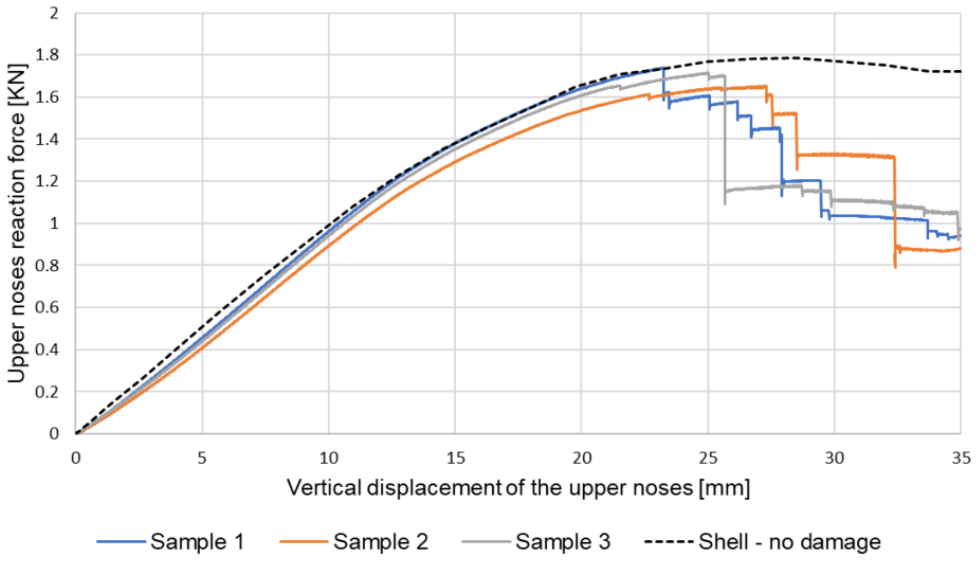

b)

Figure 69 Results of nonlinear elastic model a) model loaded and high deformation achieved b) model and experimental results using layup 2.

5.6.2 Plane Strain Nonlinear Elastic Model

Macias [114] took the concept introduced in section 5.6.1 and included the nonlinear effects of large displacements and fragmentation of carbon plies in the 2D model. To model fragmentation, Macias added several rows of intralaminar cohesive elements. The strength of intralaminar the cohesive element is variable following the Weibull distribution Eq. (22),

were σ_{CE} is the strength of a row of cohesive elements, σ^0 is the tensile strength reported in Table 14 for M55 and T1000, n is a random variable between 0 and 1 and m is the Weibull modulus which is 40 for both materials.

$$\sigma_{CE} = \sigma^0 \left[In\left(\frac{1}{1-n}\right)\right]^{1/m} \qquad \text{Eq. (22)}$$

For the model, Macias used 200 cohesive sections (cohesive pars) were placed for each carbon layer. The section of the specimen where all the cohesive elements are located is only between the loading noses. The blocks of T1000 plies are modelled as a unique ply of 0.128mm of thickness as it is shown in Figure 70.

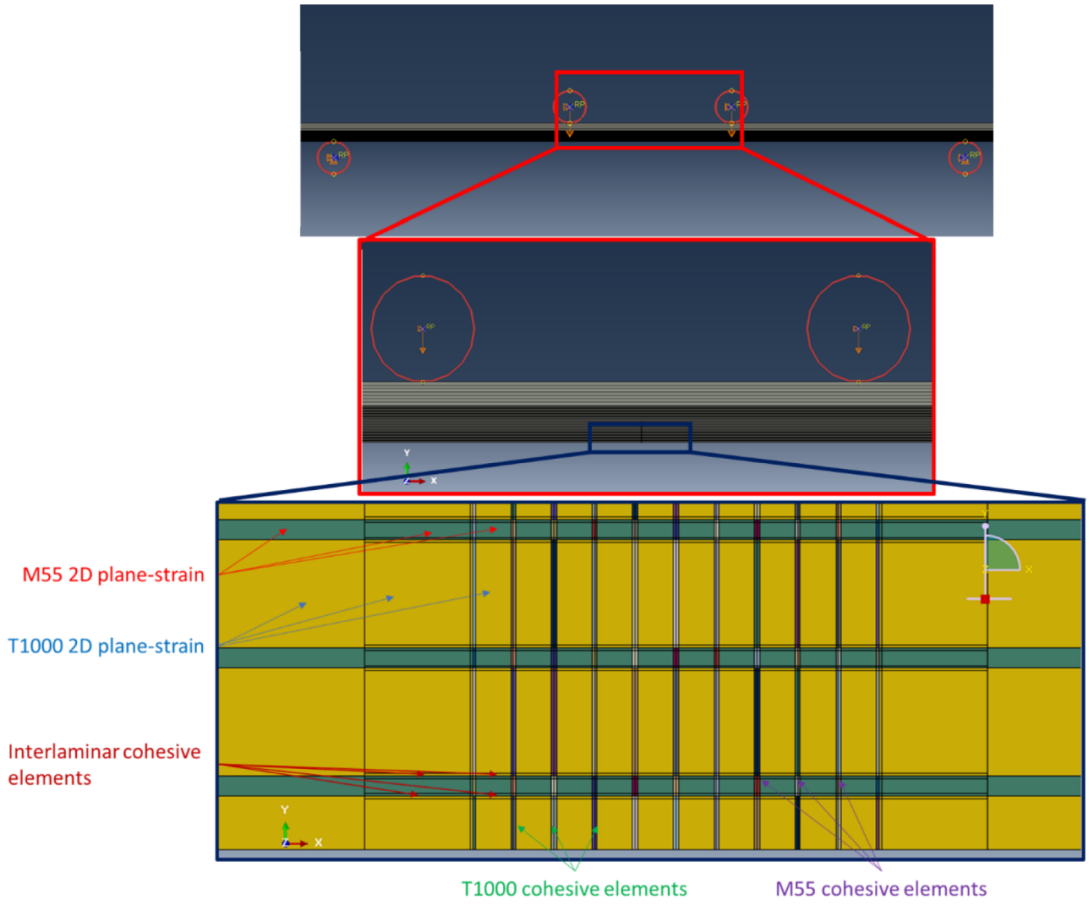

Figure 70 Cohesive element distribution in the 2D plane strain nonlinear elastic model.

Figure 71 shows the results obtained using the plane strain nonlinear elastic model proposed by Macias. Figure 71a shows the brush-like appearance produced in the tensile side by fragmentation and delamination of carbon plies. Modelling fragmentation through the use of several rows of intralaminar cohesive elements becomes the failure appearance more consistent with the experimental results shown in Figure 56b. The force vs displacement curve obtained by the model is compared with the experimental results of samples of layup 2 in Figure 71b. The model reproduces the experimental curves with good accuracy until 21mm where the first load-drop takes place. Despite M55 fragmentation is

considered, the nonlinear curve before load-drop is similar to the curve obtained using the shell element model of section 5.6.1, which confirm that the effect of local fragmentation of M55 plies in the stiffness reduction of the laminate is low. According to Macias [114], fragmentation of the three bottom M55 layers is observed before the failure of the bottom T1000 block, which is similar to the results showed before in Figure 67b (plies 1st, 3rd, 5th and 6th in the failure rank). Similar to the model of section 5.6.1 the first load drop is produced at an earlier displacement than the experimental one, as it was mentioned before, this is because properties are assumed in the model.

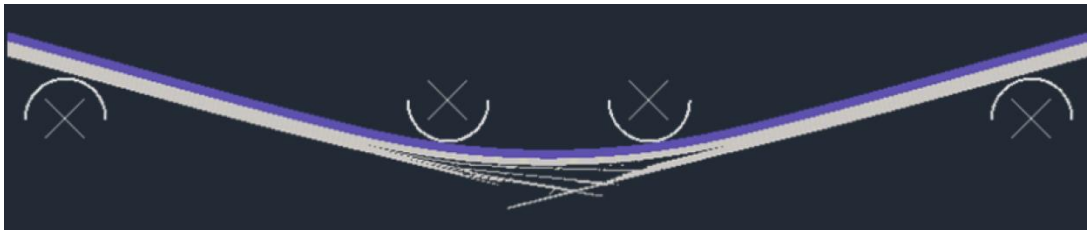

a)

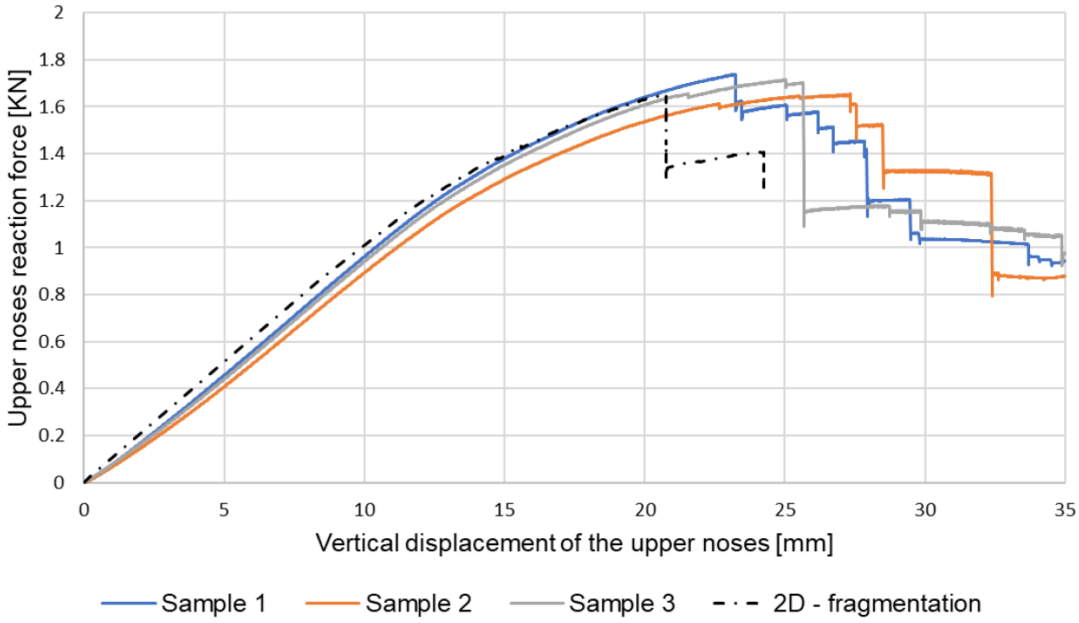

b)

Figure 71 Plane strain nonlinear elastic model results in a) brush-like failure appearance and gradual failure in tension. b) force-displacement curve

5.8 Conclusions

The methodology proposed in this chapter successfully achieved gradual failure of hybrid asymmetric composite laminates under flexural loading, producing highly-nonlinear load-displacement curves and progressive brush-like failure with large deformations. Implementing damage mode maps, it was possible to design a suitable building block for the carbon/carbon sub-laminate promoting a fragmentation damage mode in tension. Knowing the failure sequence of the plies, it was possible to identify the optimum architecture of the layups, obtaining a safe margin between compressive and tension failure and avoiding compressive failure initiation. Both proposed layups showed gradual failure behaviour as well as similar results in terms of load-displacement, load-strain curves, failure mechanisms and energy absorption.

The micrographs confirmed the predicted failure mechanisms and provide and evidence of the failure sequence. It was observed that in the non-linear part of the load-displacement curve and before any load drop, the bottom M55 layers on the tensile side started to fragment. At larger applied displacements after the load drop, not only fragmentation in the M55 plies in tension is observed, but also locally dispersed delamination at the M55/T1000 interface. At the same applied displacement, fragmentation was observed in the top M55 plies under compression. No damage was observed in the T1000 and S-Glass layers on the compressive side, showing that the suggested layups were successful in suppressing unstable compressive failure mechanisms.

A good correlation was found between the code and the numerical analysis showing similar failure sequence for the first set of plies. According to the numerical models, the bottom surface T1000 plies fail in tension, producing a complete de-bonding of the M55/T1000 building block in the form of a brush-like failure from the intact part of the beam. This creates a rather small load drop in the load-displacement curve and continues as further displacement is applied, leading to the second-bottom building block failing and separating from the beam. The gradual separation of the building blocks on the tensile side results in a gradual neutral axis shift to the top of the beam, further reducing the risk of having a compressive failure.

The numerical model demonstrates that the nonlinear behaviour is produced mainly by large geometric deformations but the fragmentation of M55 plies contributes to the initiation of this nonlinear response. Finally, unlike the code and the numerical models, the failure of M55 plies in compression reported by the microscope observation takes places in higher displacement which suggest that the failure strain of M55 plies in compression is higher than the value reported in Table 10.

5.9 Recommendations and Future Works

Both the code and the models depend on the properties used in the analysis. To increase the accuracy of the method used in the layup design and the predictive models, an experimental campaign is required to properly measure the properties of the materials and the intralaminar and interlaminar toughness. Using accurate models, it is possible to optimise the layups reducing the number of thin carbon plies and increasing the flexural strength. This could produce a range of layups designed for specific applications.

REFERENCES

[1] M. Jansen. The evolution of thermoplastic composites: The road to highest lightweight potential in mass production. Reinforced Plastics Volume 64, Number 1 January/February 2020.

[2] Market research report, Global forecast to 2024. Available: www.marketsandmarkets.com

[3] E. Witten, V. Mathes, M.Sauer, M. Kühnel. Composites market report published by AVK-Industrievereinigung Kunststoffe eV in 2018. Available: www.avk-tv.de

[4] Airbus Group. A350 XWB: Sensational - Shape - Modern. 2006. [Online]. Available: http://www.a350xwb.com.

[5] L. Mishnaevsky, K. Branner, H.N. Petersen, J. Beauson, M. McGugan, B.F. Sørensen. Materials for wind turbine blades: An overview. Materials (Basel)., vol. 10, no. 11, pp. 1–24, 2017.

[6] G. Czél, MR. Wisnom. Demonstration of pseudo-ductility in high performance glass-epoxy composites by hybridisation with thin-ply carbon prepreg. Compos Part A Appl Sci Manuf 2013; 52:23–30.

[7] Y. Swolfs, L. Gorbatikh, I. Verpoest. Fibre hybridisation in polymer composites: A review. Composites: Part A 67 (2014) 181–200.

[8] Y. Swolfs, I. Verpoest, L. Gorbatikh. Recent advances in fibre-hybrid composites: materials selection, opportunities and applications. International Materials Reviews, 64:4, 181-215, 2019.

[9] M. Jalalvand, G. Czél, M.R. Wisnom. Parametric study of failure mechanisms and optimal configurations of pseudo-ductile thin-ply UD hybrid composites. Compos Part A Appl Sci Manuf 2015; 74:123–31.

[10] G. Czél, M. Jalalvand, M. R. Wisnom, “Design and characterisation of advanced pseudo-ductile unidirectional thin-ply carbon/epoxy-glass/epoxy hybrid composites,” Compos. Struct., vol. 143, pp. 362–370, 2016.

[11] E.J. Barbero. Introduction to composite materials design. Taylor & Francis, CRC Press, Boca Raton, FL, third edition 2017

[12] D.W. Dwight, Glass Fiber Reinforcements, in: A. Kelly, C.B.T.-C.C.M. Zweben (Eds.), Compr. Compos. Mater., Pergamon, Oxford, 2000: pp. 231–261.

[13] B.A. Newcomb, Processing, structure, and properties of carbon fibers, Compos. Part A Appl. Sci. Manuf. 91 (2016) 262–282.

[14] K. Naito, Y. Tanaka, J.M. Yang, et al. Tensile properties of ultrahigh strength PAN-based, ultrahigh modulus pitch-based and high ductility pitch-based carbon fibers. Carbon N Y. 2008;46(2):189–195.

[15] B.A. Newcomb. Processing, structure, and properties of carbon fibers. Compos Part A Appl Sci Manuf. 2016;91:262–282.

[16] H. Miyagawa, T. Mase, C. Sato, et al. Comparison of experimental and theoretical transverse elastic modulus of carbon fibers. Carbon N Y. 2006;44 (10):2002–2008.

[17] K.D. Jones, A.T. Dibenedetto. Fiber fracture in hybrid composite systems. Compos Sci Technol. 1994;51 (1):53–62.

[18] M.L. Korwin-Edson, D.A. Hofmann, P.B. McGinnis. Strength of high performance glass reinforcement fiber. Int J Appl Glass Sci. 2012;3(2):107–121.
[19] Y. Swolfs, I. Verpoest, L. Gorbatikh. A review of input data and modelling assumptions in longitudinal strength models for unidirectional fibre-reinforced composites. Compos Struct. 2016;150:153–172.
[20] N. Svensson, R. Shishoo, M. Gilchrist, "Manufacturing of Thermoplastic Composites from Commingled Yarns-A Review," J. Thermoplast. Compos. Mater., vol. 11, no. 1, pp. 22-56, 1998.
[21] A.R. Offringa. Thermoplastic composites – rapid processing applications. Compos Part A Appl Sci Manuf. 1996;27(4):329–336.
[22] G. Fernlund and A. Poursartip, Autoclave processing for composites. Woodhead Publishing Limited, 2012.
[23] A. McIlhagger, E. Archer, R. McIlhagger. Manufacturing processes for composite materials and components for aerospace applications. Woodhead Publishing Limited, 2020.
[24] B. W. Rosen, "Tensile failure of fibrous composites," AIAA J., vol. 2, no. 11, pp. 1985–1991, 1964.
[25] M.R. Nedele, M.R. Wisnom. Stress-concentration factors around a broken fiber in a unidirectional carbon-fiber-reinforced epoxy. Composites 1994;25(7): 549–57.
[26] Y. Swolfs, L. Gorbatikh, V. Romanov, S. Orlova, S.V. Lomov, I. Verpoest. Stress concentrations in an impregnated fibre bundle with random fibre packing. Compos Sci Technol 2013;74:113–20.
[27] Y. Swolfs, R.M. McMeeking, I. Verpoest, L. Gorbatikh. Matrix cracks around fibre breaks and their effect on stress redistribution and failure development in unidirectional composites. Composites Science and Technology 108 (2015) 16–22
[28] T. Okabe, M. Nishikawa, N. Takeda. Numerical modeling of progressive damage in fiber reinforced plastic cross-ply laminates. Composites Science and Technology 68 (2008) 2282–2289.
[29] P. Wright, X. Fu, I. Sinclair, S.M. Spearing. Ultra high resolution computed tomography of damage in notched carbon fiber epoxy composites. Journal of Composite Materials 2008 42: 1993
[30] L. R. Dharani, J. Wei, F. S. Ji and J. H. Zhao. Saturation of Transverse Cracking with Delamination in Polymer Cross-Ply Composite Laminates. International Journal of Damage Mechanics 2003 12:89
[31] L. Szu-Hui, L. Shuguang. Energy release rates for transverse cracking and delaminations induced by transverse cracks in laminated composites. Composites: Part A 36 (2005) 1467–1476.
[32] A. Melnikov, Y. Swolfs, S.V. Lomov, L. Gorbatikh. Do transverse cracks affect the in-situ strength and fibre breaks accumulation in longitudinal plies of cross-ply laminates?. ECCM18 - 18th European Conference on Composite Materials. Athens, Greece, 24-28 th June 2018.
[33] M. Ueda, W. Saito, R. Imahori, D. Kanazawa, and T. K. Jeong, "Longitudinal direct compression test of a single carbon fiber in a scanning electron microscope," Compos. Part A Appl. Sci. Manuf., vol. 67, pp. 96–101, 2014.

[34] G. C. Shih and L. J. Ebert, “Flexural failure mechanisms and global stress plane for unidirectional composites subjected to four-point bending tests,” Composites, vol. 17, no. 4, pp. 309–320, 1986.
[35] C.T. Sun, J.L. Tsai. Comparison of microbuckling model and linl band model in predicting compressive strengths of composites. Proceeding of ICCM13, Beijing, China, June 2001.
[36] S.W. Tsai. Thin ply composites. JEC Compos Mag 2005;42:31–3.
[37] North Thin Ply Technology. 2016. www.thinplytechnology.com.
[38] NorthThin PlyTechnology (ProductReview). Reinforced Plastics. 2016;60:28–29.
[39] R. Amacher, W. Smith, J. Botsis, C. Dransfeld, J. Cugnoni . New design opportunities using thin-ply composites. JEC Compos Mag 2015;52:33–5.
[40] J. Galos. Thin-ply composite laminates: a review. Composite Structures 236 (2020) 111920.
[41] K. Kawabe, T. Matsuo, Z. Maekawa. New technology for opening various reinforcing fiber tows. J Soc Mater Sci, Japan 1998; 47:727–34.
[42] S.W. Tsai, K. Kawabe. Thin ply laminates. Japanese Patent: JP2014177125A. 2007.
[43] S. Sihn, R.Y. Kim, K. Kawabe, S.W. Tsai. Experimental studies of thin-ply laminated composites. Composites Science and Technology 67 (2007) 996–1008.
[44] L.N. Phillips, Improving racing-car bodies, Composites 1 (1969) 50–51.
[45] C. Zweben, Tensile strength of hybrid composites, J. Mater. Sci. 12 (1977) 1325–1337.
[46] J. Summerscales, D. Short, Carbon fibre and glass fibre hybrid reinforced plastics, Composites 9 (3) (1978) 157–166.
[47] P.W. Manders, M.G. Bader, The strength of hybrid glass/carbon fibre composites – Part 1, J. Mater. Sci. 16 (1981) 2233–2245.
[48] M.G. Phillips, Composition parameters for hybrid composite materials, Composites 12 (2) (1981) 113–116.
[49] G. Kretsis, A review of the tensile, compressive, flexural and shear properties of hybrid fibre reinforced plastics, Composites 18 (1) (1987).
[50] Y. Swolfs et.al. Tensile behaviour of intralayer hybrid composites of carbon fibre and self-reinforced polypropylene. Composites: Part A 59 (2014) 78–84
[51] Y. Swolfs et.al. Introducing ductility in hybrid carbon fibre/self-reinforced composites through control of the damage mechanisms. Composite Structures 131 (2015) 259–265.
[52] T. Hayashi, On the improvement of mechanical properties of composites by hybrid composition, in: Proc 8th Int Reinf. Plast. Conf., 1972: pp. 149–152.
[53] A.R. Bunsell, B. Harris, Hybrid carbon and glass fibre composites, Composites 5 (1974) 157e164.
[54] L.N. Phillips. The hybrid effect - does it exist?. Composites. January 1976
[55] Aveston J, Sillwood JM. Synergistic fibre strengthening in hybrid composites. J Mater Sci 1976; 11:1877–83.
[56] H. Fukuda, An advanced theory of the strength of hybrid composites, J. Mater. Sci. 19 (3) (1984) 974–982.

[57] Czél G, Jalalvand M, Wisnom MR. Hybrid specimens eliminating stress concentrations in tensile and compressive testing of unidirectional composites. Composites: Part A 91 (2016) 436–447.
[58] M.R. Wisnom, G. Czel, Y. Swolfs, M. Jalalvand, L. Gorbatikh, I. Verpoest, Hybrid effects in thin ply carbon/glass unidirectional laminates: accurate experimental determination and prediction, Compos Part A 88 (2016) 131-139.
[59] J. Xing, G.C. Hsiao, T.W. Chou, A dynamic explanation of the hybrid effect, J. Compos. Mater. 15 (SEP 1981) 443–461.
[60] Y. Swolfs, R.M. McMeeking, L. Gorbatikh, I. Verpoest. The effect of fibre dispersion on initial failure strain and cluster development in unidirectional carbon/glass hybrid composites, Compos. A: Appl. Sci. Manuf. 69 (2015) 279–287.
[61] R. Kulkarni, O. Ochoa. Transverse and longitudinal CTE measurements of carbon fibers and their impact on interfacial residual stresses in composites, J. Compos. Mater. 40 (2006) 733–754.
[62] C. Dong. Development of an engineering model for predicting the transverse Coefficients of thermal expansion of unidirectional fiber reinforced composites, J. Eng. Mater. Technol. Trans. ASME. 131 (2009) 0310011–0310017.
[63] D.L. Motoc, J. Ivens, N. Dadirlat. Coefficient of thermal expansion evolution for cryogenic preconditioned hybrid carbon fiber/glass fiber-reinforced polymeric composite materials, J. Therm. Anal. Calorim. 112 (2013) 1245–1251.
[64] J. Hedgepeth, Stress concentrations in filamentary structures, NASA, TN. D-882 (1961) 1–36.
[65] PWJ. van den Heuvel, YJW. van der Bruggen, T. Peijs. The influence of carbon fibre surface treatment on fibre-fibre interactions in multi-fibre microcomposites. Adv Compos Lett 1994;3(6):197–201.
[66] D.G. Harlow, S.L. Phoenix. Probability distributions for the strength of composite materials I: two-level bounds. Int J Fract 1981;17(4):347–72.
[67] R.L. Smith. Limit theorems and approximations for the reliability of load-sharing systems. Adv Appl Probab 1983;15(2):304–30.
[68] J.M. Neumeister. A constitutive law for continuous fiber reinforced brittle matrix composites with fiber fragmentation and stress recovery. J Mech Phys Solids 1993;41(8):1383–404.
[69] X.F. Zhou, H.D. Wagner. Stress concentrations caused by fiber failure in two-dimensional composites. Compos Sci Technol 1999;59(7):1063–71.
[70] Y. Swolfs et. al. Global load-sharing model for unidirectional hybrid fibre-reinforced composites, J. Mech. Phys. Solids 84 (2015) 380–394.
[71] H. Fukuda, T.W. Chou, Stress concentrations in a hybrid composite sheet, J. Appl. Mech. Trans. ASME. 50 (1983) 845–848.
[72] Y. Swolfs, L. Gorbatikh, I. Verpoest, Stress concentrations in hybrid unidirectional fibre-reinforced composites with random fibre packings, Compos. Sci. Technol. 85 (2013) 10–16
[73] L. Mishnaevsky, G. Dai, Hybrid carbon/glass fiber composites: Micromechanical analysis of structure-damage resistance relationships, Comput. Mater. Sci. 81 (2014) 630–640.

[74] Y. Swolfs, I. Verpoest, L. Gorbatikh. Maximising the hybrid effect in unidirectional hybrid composites. Mater Des. 2016;93:39–45.
[75] M. Jalalvand, M. Fotouhi, M.R. Wisnom. Orientation-dispersed pseudo-ductile hybrid composite laminates - A new lay-up concept to avoid free-edge delamination**.** Composites Science and Technology 153 (2017) 232-240.
[76] M. Jalalvand, G. Czél, M. R. Wisnom, "Damage analysis of pseudo-ductile thin-ply UD hybrid composites – A new analytical method," Compos. Part A Appl. Sci. Manuf., vol. 69, pp. 83–93, Feb. 2015.
[77] M. Jalalvand, G. Czél, M. R. Wisnom, "Numerical modelling of the damage modes in UD thin carbon/glass hybrid laminates," Compos. Sci. Technol., vol. 94, pp. 39–47, 2014.
[78] M. Jalalvand, G. Czél, M. R. Wisnom, T. Czigány. Design and characterisation of high performance, pseudo-ductileall-carbon/epoxy unidirectional hybrid composites. Composites Part B 111 (2017) 348-356.
[79] J.D. Fuller, M.R. Wisnom. Pseudo-ductility and damage suppression in thin ply CFRP angle-ply laminates. Composites: Part A 69 (2015) 64–71.
[80] M. Fotouhi, M. Jalalvand, M.R. Wisnom. High performance quasi-isotropic thin-ply carbon/glass hybrid composites with pseudo-ductile behaviour in all fibre orientations. Composites Science and Technology 152 (2017) 101-110.
[81] G. Czél et.al. Pseudo-ductility and reduced notch sensitivity in multi-directional all-carbon/epoxy thin-ply hybrid composites. Composites: Part A 104 (2018) 151–164.
[82] J.W. Giancaspro, C.G. Papakonstantinou, P.N. Balaguru. Flexural response of inorganic hybrid composites with E-Glass and Carbon fibers. J Eng Mater Technol 2010;132. 021005e1-8.
[83] IDG. Subagia, Y. Kim, L.D. Tijing, C.S. Kim, H.K. Shon. Effect of stacking sequence on the flexural properties of hybrid composites reinforced with carbon and basalt fibers. Compos B Eng 2014; 58:251–8.
[84] M. Kalantari, C. Dong, I.J. Davies. Multi-objective analysis for optimal and robust design of unidirectional glass/carbon fibre reinforced hybrid epoxy composites under flexural loading. Compos Part B Eng 2016; 84:130-9.
[85] M. Kalantari, C. Dong, I.J. Davies. Effect of matrix voids, fibre misalignment and thickness variation on multi-objective robust optimization of carbon/glass fibre-reinforced hybrid composites under flexural loading. Composites Part B 123 (2017) 136-147
[86] Sudarisman, I.J. Davies. Flexural failure of unidirectional hybrid fibre-reinforced polymer (FRP) composites containing different grades of glass fibre. Adv Mater Res 2008; 41–42:357–62.
[87] Sudarisman, B. de San Miguel, I.J. Davies. The effect of partial substitution of E-glass fibre for carbon fibre on the mechanical properties of CFRP composites. Proc Int Conf Mater Metall Technol (ICOMMET 2009) 2009:125–8.
[88] C. Dong, I. J. Davies, "Optimal design for the flexural behaviour of glass and carbon fibre reinforced polymer hybrid composites," Mater. Des., vol. 37, pp. 450–457, 2012.
[89] C. Dong, I.J. Davies. Effect of stacking sequence on the flexural properties of carbon and glass fibre-reinforced hybrid composites Advanced Composites and Hybrid Materials 1, 530–540 (2018).

[90] M.R. Wisnom. The effect of specimen size on the bending strength of unidirectional carbon fibre-epoxy. Composite Structures 18 (1991) 47 -63
[91] M.R. Wisnom. On the high compressive strains achieved in bending tests on unidirectional carbon-fibre / epoxy. Composites Science and Technology 43 (1992) 229-235
[92] G. Czél, M. Jalalvand, M.R. Wisnom. Hybrid specimens eliminating stress concentrations in tensile and compressive testing of unidirectional composites. Composites: Part A 91 (2016) 436–447
[93] G. Czél, P. Suwarta, M. Jalalvand, M.R. Wisnom. Investigation of the compression performance and failure mechanism of pseudo-ductile thin-ply hybrid composites. 21st International Conference on Composite Materials Xi'an, 20-25th August 2017.
[94] X. Wu, J.D. Fuller, M.R. Wisnom Combining the non-linearity of angle-plies and fibre fragmentation in carbon fibre laminates under compressive loading. 21st International Conference on Composite Materials Xi'an, 20-25th August 2017.
[95] F. Mesquita, Y Swolfs, S.V. Lomov, L. Gorbatikh Ply fragmentation in unidirectional hybrid composites linked to stochastic fibre behaviour: A dual-scale mode. Composites Science and Technology 181 (2019) 107702.
[96] M. Jalalvand, M.R. Wisnom, H. Hosseini-Toudeshky, B. Mohammadi. Experimental and numerical study of oblique transverse cracking in cross-ply laminates under tension. [] Composites: Part A 67 (2014) 140–148
[97] Dong CS, Duong J, Davies IJ. Flexural properties of S2 glass and TR30S carbon fiber-reinforced epoxy hybrid composites. Polym Compos. 2012;33(5):773–781.
[98] S. Blassiau, A. Thionnet, A.R. Bunsell. Micromechanisms of load transfer in a unidirectional carbon fibre–reinforced epoxy composite due to fibre failures. Part 1:
[99] Micromechanisms and 3D analysis of load transfer: The elastic case. Composite Structures 74 (2006) 303–318
[100] Dai G, Mishnaevsky Jr L. Fatigue of hybrid glass/carbon composites: 3D computational studies. Compos Sci Technol. 2014;94:71–79.
[101] Mishnaevsky L Jr, Dai G. Hybrid carbon/glass fiber composites: micromechanical analysis of structure damage resistance relationships. Comput Mater Sci. 2014;81:630–640.
[102] B. Sabuncuoglu, S. Orlova, L. Gorbatikh, S.V. Lomov, I. Verpoest. Micro-scale finite element analysis of stress concentrations in steel fiber composites under transverse. Journal of Composite Materials published online 1 April 2014
[103] P.W. Harper, S.R. Hallett. Cohesive zone length in numerical simulations of composite delamination. Engineering Fracture Mechanics 75 (2008) 4774–4792.
[104] C. Dong, I.J. Davies. Optimal design for the flexural behaviour of glass and carbon fibre reinforced polymer hybrid composites. Materials and Design 37 (2012) 450–457
[105] C. Dong, I.J Davies. Flexural strength of bidirectional hybrid epoxy composites reinforced by E glass and T700S carbon fibres. Compos Part B Eng. 2015;72 (0):65–71.
[106] E. Kalfon-Cohen et.al. Synergetic effects of thin plies and aligned carbon nanotube interlaminar reinforcement in composite laminates. Composites Science and Technology volume 166, 29 September 2018, Pages 160-168.
[107] Abaqus 6.12, analysis user's manual, volume IV: elements, charpter 32.5 cohesive elements.

[108] E.J. Barbero. Finite element analysis of composite materials using ansys. Taylor & Francis, CRC Press, Boca Raton, FL, second edition 2014.
[109] A. Turon, C.G. Dávila, P.P Camanho, J. Costa. An engineering solution for using coarse meshes in the simulation of delamination with cohesive zone models. NASA/TM-2005-213547.
[110] P. Suwarta, M. Fotouhi, G. Czél, M. Longana, and M. R. Wisnom, "Fatigue behaviour of pseudo-ductile unidirectional thin-ply carbon/epoxy-glass/epoxy hybrid composites," Compos. Struct., vol. 224, no. January, p. 110996, 2019.
[111] G. Czél, M. Jalalvand, M.R. Wisnom. Demonstration of pseudo-ductility in unidirectional hybrid composites made of discontinuous carbon/epoxy and continuous glass/epoxy plies. Composites: Part A 72 (2015) 75–84.
[112] G. Czél, M. Bugár-Mészáros. M.R. Wisnom. The effect of test temperature on the pseudoductility of thin-ply hybrid composites. ECCM18 - 18th European Conference on Composite Materials. Athens, Greece, 24-28th June 2018.
[113] P.P. Camanho, C.G Davila. Mixed-Mode decohesion finite elements for the simulation of delamination in composite materials. NASA/TM-2002-211737.
[114] J.M Macias. Numerical and analytical models for the design of hybrid composite laminates with gradual failure behaviour under bending loads. Master thesis, Universidad Nacional de Colombia, Medellin-Colombia 2020.